THE UNIVERSITY OF CHICAGO

INVESTIGATING THE HIERARCHY OF SUBDIVISIONS IN PRIMARY MOTOR CORTEX, AND BETWEEN PRIMARY MOTOR AND SOMATOSENSORY CORTICES DURING NATURALISTIC BEHAVIORS

A DISSERTATION SUBMITTED TO

THE FACULTY OF THE DIVISION OF THE BIOLOGICAL SCIENCES

AND THE PRITZKER SCHOOL OF MEDICINE

IN CANDIDACY FOR THE DEGREE OF

DOCTOR OF PHILOSOPHY

COMMITTEE ON COMPUTATIONAL NEUROSCIENCE

BY

ALEXANDER RAJAN

CHICAGO, ILLINOIS

JUNE 2016

Table of Contents

Table of Figures

I. Introduction

Hierarchy in the Motor Cortex

A popular framework to help comprehend the complicated connections and interactions between cortical areas is to place them in a so-called cortical hierarchy [1]. To do so is helpful not only to describe interactions between cortical areas and their neural processing, but also to make predictions. For example, one would expect a cortical area that is higher in the hierarchy to have more complex, or abstract, receptive or projection fields. Indeed, this functional difference in cortical areas is a defining characteristic of cortical hierarchies. Another defining characteristic are different patterns of laminar connections: ascending projections terminate on middle cortical layers, and descending projections terminate onto high and low cortical layers, avoiding the middle layers [2]. Thus, cortical hierarchies, in this dissertation, are defined by the functional properties of responses, and the neuroanatomical underpinnings of laminar connectivity.

In motor cortex hierarchies, the "higher" cortical areas project motor commands down to "lower" cortical areas, and receive ascending feedback. This contrasts with sensory hierarchies, in which lower areas (eg, V1) project sensory information forwards to higher areas (eg, V2). Thus, in the motor cortex, premotor cortex projects high-level motor commands to the lower primary motor cortex, which in turn sends feedback signals to premotor cortex. Further, the timing of activation of cortical areas is different between sensory and motor systems. In motor systems, as commands for voluntary movement are generated, higher areas modulate firing earlier than lower areas. In somatosensory systems, hierarchically lower areas modulate firing earlier, sending their stimulus responses up to higher areas.

In this dissertation, I hope to place two subdivisions in the classic motor cortex hierarchy relative to each other. To do so, I begin with the assumption that there are consistent hierarchical rules in the motor cortices. Thus, here I build a comparison between ventral premotor (PMv) and motor (M1) cortices,

and extend that comparison to differentiate between rostral (rM1) and caudal (cM1) primary motor cortex. Additionally, I will provide evidence that supplements previous suggestions that M1 is hierarchically higher than primary somatosensory cortex (S1) in the somatomotor cortical hierarchy.

There are several lines of research that define the relative hierarchical positions of premotor and motor cortex. Premotor cortex has more abstract representations of the body and movement parameters in both humans and macaques [3,4]. For example, premotor cortex has been shown to have a higher proportion of neurons that encode movement in extrinsic coordinates compared to intrinsic, muscle-like coordinates in motor cortex [5,6]. Kakei, Hoffman, & Strick trained monkeys to perform wrist movements in different coordinate frames: extrinsic, joint, or muscle [5]. About 80% of directionally-tuned PMv neurons were extrinsic-like, whereas in M1 the proportion of extrinsic-, joint-, and muscle-like neurons were more equal. Premotor cortex is also involved in the transformation from visual-centric coordinate frames to body coordinates [7] and has been found to contain "mirror neurons" [8,9]. Additionally, premotor cortex has higher stimulation thresholds to elicit movement than primary motor cortex [10,11]. Further, although both PM and M1 have descending projections, M1 has more numerous and more effective corticospinal projections than premotor cortex [11–13]. Thus, primary motor cortex is more tightly related to muscle activity than premotor cortex, suggesting it is lower in the hierarchy.

Premotor cortex neurons begin firing modulation prior to primary motor cortical neurons [14]. This suggests that information is processed serially between the two areas, rather than in parallel, and that premotor cortex is earlier (higher) in the hierarchy.

Another line of evidence that illuminates the hierarchy between premotor and motor cortex are the bidirectional anatomical connections [1,2]. Laminar projections have traditionally been used to delineate cortical hierarchies based on patterns of connections [1,15,16]. Ascending connections project to middle layers, whereas descending connections project to higher and lower layers (Figure 1).

However, in motor hierarchies, the order (forward vs feedback) is reversed compared to sensory hierarchies; that is to say that ascending connections are feedback, and descending connections are forward. Thus, ventral premotor and primary motor cortices are densely interconnected, and the projections show differences in their laminar targets [17]. There are ascending projections from motor cortex to premotor cortex, and descending projections from premotor cortex to motor cortex, placing ventral premotor cortex higher, hierarchically, to primary motor cortex.

Interestingly, projections from PMv to M1 are topographically divergent, whereas projections from M1 to PMv are topographically convergent [18]. Tracer injections into the hand representation of each led to different patterns of connectivity. While the PMv projections were diffuse across proximal and distal forelimb representations in M1, the M1 projections were predominantly limited to within the hand representation of PMv. This study suggests that forward connections from higher cortical motor areas will be more divergent, whereas feedback connections will be less divergent.

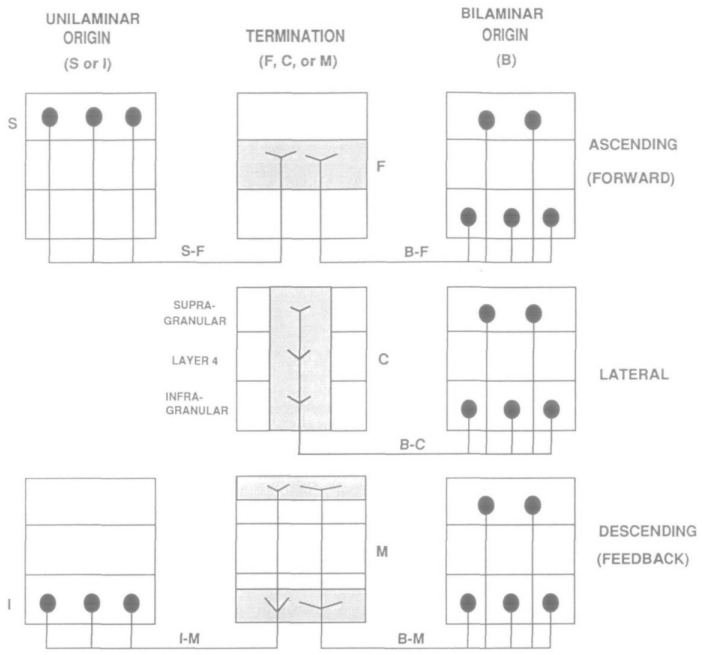

Figure 1 – Patterns of Laminar Projections.
The patterns of laminar projections shown above have been used to place cortical areas relative to each other in cortical hierarchies. Ascending projections, from low areas to high areas, target the middle layers of the higher, receiving area. Additionally, descending projections, from high areas to low, avoid middle areas, and instead target superficial and deep layers. Van Essen, 1991 [1] .

Unfortunately, there are very few studies that have attempted to address the hierarchical organization between the rostral (rM1) and caudal (cM1) subdivisions within the primary motor cortex (M1). Most studies of M1 focus only on the superficially located

rM1 in the precentral gyrus, as the deeper caudal M1, located on the anterior bank of the central sulcus, is more difficult to access for recording. Further, there have been no studies assessing the laminar connectivity between rM1 and cM1. Indeed, only two studies have looked at the connectivity between the subdivisions, and they both focused on flattened projections of cortex [16,19], which make laminar delineations difficult.

However, cM1 does have a significantly higher proportion of descending connections, particularly corticomotoneuronal cells [13,20,21]. Further, stimulation thresholds in cM1 tend to be lower than in rM1 [22]. These findings together suggest that cM1 is more closely linked to motoneurons and muscles, and therefore likely lower in the cortical hierarchy than rM1.

Based on these prior studies comparing the hierarchical organization of premotor and motor cortices, I expect similar patterns between rostral and caudal subdivisions of motor cortex. For example, rM1 firing will precede cM1, and rM1-cM1 spike-field coherence will precede cM1-rM1 coherence. Further, I predict that coherent connections from rostral to caudal M1 will be more divergent: one rM1 spiking neuron will be coherent with more cM1 LFPs, than coherent connections from cM1 to rM1.

Similarly, I hypothesize that M1 is higher than S1 in the cortical hierarchy. This is foremost based on laminar connections between the two areas: S1 projects strongly onto layer 3 of motor cortex, in an ascending pattern, and M1 projections to S1 tend to avoid middle layer 4 [15,23,24].

Other research findings agree with this hierarchical structure. For example, as between PMv and M1, the motor representation in M1 is more complex than in S1 [25,26]. Whereas somatosensory mappings are highly organized and structured, motor maps are highly fractionated, distributed, and spread across more diffusely across motor cortex. Further, task-modulated neural activity in M1 usually precedes S1, although S1 neurons often fire before movement onset [27,28]. These studies support the

argument that, as M1 may be placed in somatosensory hierarchies [1,2], S1 may be placed in a motor cortical hierarchy.

Accordingly, several predictions may be made regarding activity between M1 and S1. First, I expect M1 firing to precede that in S1 in simultaneously recorded data. Further, M1-S1 will lead S1-M1 coherence.

If these hypotheses, and those regarding rostral and caudal M1, are supported, they will provide further evidence of their relative locations in the motor cortical hierarchy. The primary method to be used to analyze the interactions between cortical areas is spike-field coherence.

Spike-Field Coherence

Coherence is a measure of correlation of two signals in the frequency domain. More specifically, it is the amount of spectral content each signal shares at a given frequency, and when computed in successive time windows, across time. Before providing a more detailed explanation, it is useful to describe each component signal: spikes and local field potentials (LFPs).

Spikes

Action potentials, also known as spikes, are the output signals of individual neurons. Biologically, they are used to propagate binary signals (the existence or absence of spikes), down the axon to induce the release of neurotransmitters across the synapse. However, neurophysiologists are able to detect these output signals with microelectrodes, and thus record the "neural code," or signal, that individual neurons are transmitting. These sequences of action potentials, or "spike trains," can be correlated with stimulus inputs to or motor outputs from the nervous system. The background studies provided above, regarding, for example somatotopy, focused on spike trains.

Common analyses of spike trains include firing rates (spikes/second) and trial-by-trial variability of firing rates. Firing rates often modulate across time, either with a stimulus or a motor behavior. Indeed, neurons frequently exhibit preferred direction of stimuli [eg: 36] or movement [30,31]. However, for this dissertation I am focusing on correlations in the frequency domain.

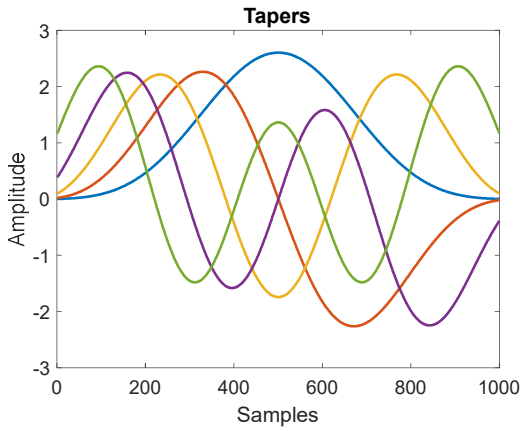

Figure 2 – Tapers Used in Multi-Taper Spectral Analyses.
The data within each time window is multiplied by each orthogonal taper prior to computing the Fast Fourier Transform.

To move spike trains from the time domain into the frequency domain, a multi-taper fast Fourier transform was used [32]. First, the signals are multiplied by orthogonal tapers (Figure 2), concentrating energy within different frequency bands. Subsequently, the fast Fourier transform is performed. These calculations are done within limited time-windows (500 ms, see Methods section for more details) to reduce the effects of non-stationarity and stepped in small increments to build a time-series.

Local Field Potentials

While spikes are an intuitive representation of the output of single neurons, there are other commonly analyzed neurophysiological signals. Local field potentials are another signal that is frequently correlated with stimuli, motor outputs, and neural signals. Indeed, LFPs represent the summation of both distant synaptic inputs and local processing [33] within hundreds of micrometers of the electrode tip [34,35].

Although LFP signals may include action potentials, they provide complementary information about the forelimb [36]. As with spike trains, different frequency bands may contain different information

or serve different roles [37]. For example, during movement, power modulates differently in various frequency bands [38–40].

Of particular interest in this dissertation are the low frequencies (2-6 Hz) of neural signals. In the motor system, a low frequency potential known as the motor event-related potential [41–43] occurs around movement onset. Additionally, these signals include task-related information, such as movement direction and grip type in reach and grasp tasks [43–47]. Indeed, kinematics from reach and grasp tasks can be decoded from low frequency LFPs in M1 [38,47], including movement direction and grasp type.

LFPs in this frequency band may represent synaptic inputs to the area [48,49] whose source is spiking from other neurons presynaptic to the neuropil being recorded. These low frequency signals likely reflect the summed inputs from intrinsic activity and areas projecting to M1, including feedforward signals from premotor areas, and sensory feedback signals [47,50].

Coherence

Coherence is a measure of correlation between two signals within a given frequency band. Although it is not predictive, it looks at how synchronized the local fields and the spikes are. However, as spikes are inherently an output signal, and LFPs reflect summed synaptic input (distal and local), my interpretation here is that it is an analytically symmetrical, but biologically asymmetrical signal.

Therefore, spikes are an output signal of individual neurons, and LFPs represent all local synaptic activity, including local processing and inputs from distal sources. Accordingly, distal spikes from another cortical area represent only a small portion of the LFP signals. However, if systems are oscillating at similar frequencies, even weak signals can maintain coherence [51,52]. Thus, coherence values, which can range in magnitude from 0 to 1, even if small, may have an effect on the receiving neural population. Periods between inhibition cycles provide temporal windows for neural interactions [53]. Further, at low frequencies the temporal window is wider, allowing for more input summation, across longer distances.

Figure 3 provides a schematic that demonstrates how spikes may be timed to arrive to combine with LFPs at maximally effective times.

Coherence between populations of neurons provides a mechanism for efficient interactions. By coordinating the input from one area to another, the timing of arriving spikes is optimal, and therefore maximally effective [54]. Two neural populations will have greater influence on each other when temporal interaction windows are coordinated, or coherent [53]. Thus, coherence may optimize the impact of spikes from one area on another [55], and coherent firing of neurons may effectively drive other neurons to fire [56]. Coherence between neural populations is likely to facilitate their interactions [53]. This suggests a mechanism through which dynamic patterns of coherence weight the anatomical connections with a gain pattern, resulting in interaction patterns that allow for dynamic changes [53]. Thus, coherence may allow populations of neurons in distant, interconnected cortical regions to be temporally and functionally linked [37].

Similar to LFP signals themselves, different frequency bands in the coherence signal are believed to have different functions [37]. Different frequencies provide different dynamical structure, and may therefore serve different roles in cortical processing [57]. Low frequency LFPs are particularly suited to entrain action potentials, as they provide a larger integration window for the low amplitude signals to have a combined effect [58,59]. Low frequency coherence has also been found in humans [60].

Coherence is highest between populations of neurons performing similar functions [61,62]. For example, coherence is stronger between populations of neurons with overlapping receptive fields than between populations of neurons with distinct receptive fields.

Theta band (4-12 Hz) coherence is task modulated [63], and has been found to project across long distances [63]. Thus, low frequency coherence is believed to be involved in synchronizing long range interactions [64]. Further, low frequency coherence may be involved in "top down" processing in visual tasks [63,65].

A recent study suggests that oscillations provide a substrate that allows for computation and long-range communication in spatially distributed brain networks [62]. By examining neural activity in motor and dorsal premotor cortex (PMd), Canolty et al found that "spiking activity in single neurons and neuronal ensembles depends on dynamic patterns of oscillatory phase coupling between multiple brain areas." Further, this dynamic modulation of neural activity is strongest between functionally similar neurons, and correlates with behavior. This suggests that these neuronal oscillations synchronize anatomically distant neural populations that, together, are actively engaged in functional roles.

In a similar study of spike-field coherence, Pesaran et al. (2008) examined the coherence between spiking of single neurons in parietal reach region (PRR) and local field potentials in PMd during a reach task. They found significant coherence that was strongly modulated during the reaching. Interestingly, they found that the spike-

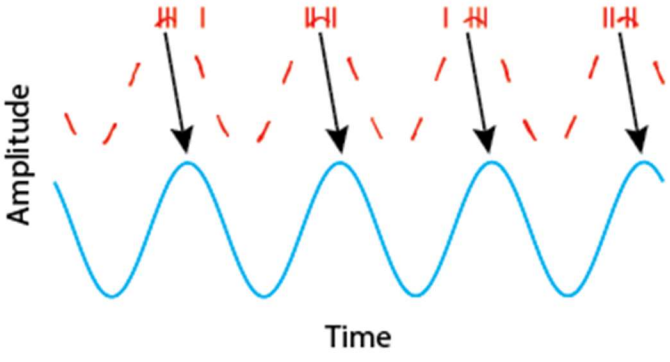

Figure 3 – Schematic Demonstration of Spike-Field Coherence.
This cartoon shows how spikes that are coherent with field potentials may arrive during key intervals to provide a maximally efficient effect on the local neural

field coherence was highly similar to partial spike-field coherence, in which field potentials local to the spiking neurons are taken into account, and therefore was not largely a result of coherence between spikes and local fields within the same area.

Here, I propose using spike-field coherence to measure the interactions between individual neurons in one cortical area and populations of neurons in another to validate the hierarchical structure between cortical areas. First I will show that these anatomically intertwined areas are synchronized in a low frequency band, and that this coherence is not symmetrical. I expect that rM1-cM1 spike-field coherence will precede cM1-rM1 spike-field coherence, and likewise that M1-S1 spike-field coherence will precede S1-M1 coherence. Additionally, I will provide support that coherence is a functional mechanism that is meaningful above and beyond either spikes or local fields.

II. Methods

All procedures were approved by the University of Chicago Institutional Animal Care and Use Committee (IACUC), the Animal Care and Use Review Office (ACURO), and complied with the guidelines set by the Association for Assessment and Accreditation of Laboratory Animal Care (AAALAC) International.

Subjects

Three rhesus macaques were each trained for their respective tasks. Two were male (Monkey Bu-Grasp & Monkey Yo-Tongue) and one female (Monkey At-Reach). Monkey Bu and Monkey Yu were research naïve. Monkey At was previously implanted in the hemisphere ipsilateral to the arm used in the task, opposite to the hemisphere of interest.

Arrays

Two types of multielectrode arrays were used: Utah Microelectrode Arrays with Cereport connectors (Blackrock Microsystems, Salt Lake City, UT) and Floating Microelectrode Arrays (FMAs, MicroProbes, Gaithersburg, MD) with Omnetics connectors (Omnetics Connector Corporation, Minneapolis, MN). All arrays were sterilized according to manufacturer specifications prior to implantation. All Utah array electrodes were 1.5 mm in length, with the exception of the 1.0 mm array in S1 of Monkey Yo. FMAs had either 18 or 36 electrodes; electrodes ranged from 3 to 11 mm in length. The length of each electrode on a given FMA were designed to target cM1. See the FMA Design section below for details regarding the designing of the FMAs.

Grasp Monkey Bu had two Utah arrays and four 18-electrode FMAs (Figure 4). One Utah array was centered on the hand representation of rM1, and one in the hand representation of S1. The S1 Utah array primarily targeted Brodmann area 2, but may have also contained electrodes in areas 1 and 5. The

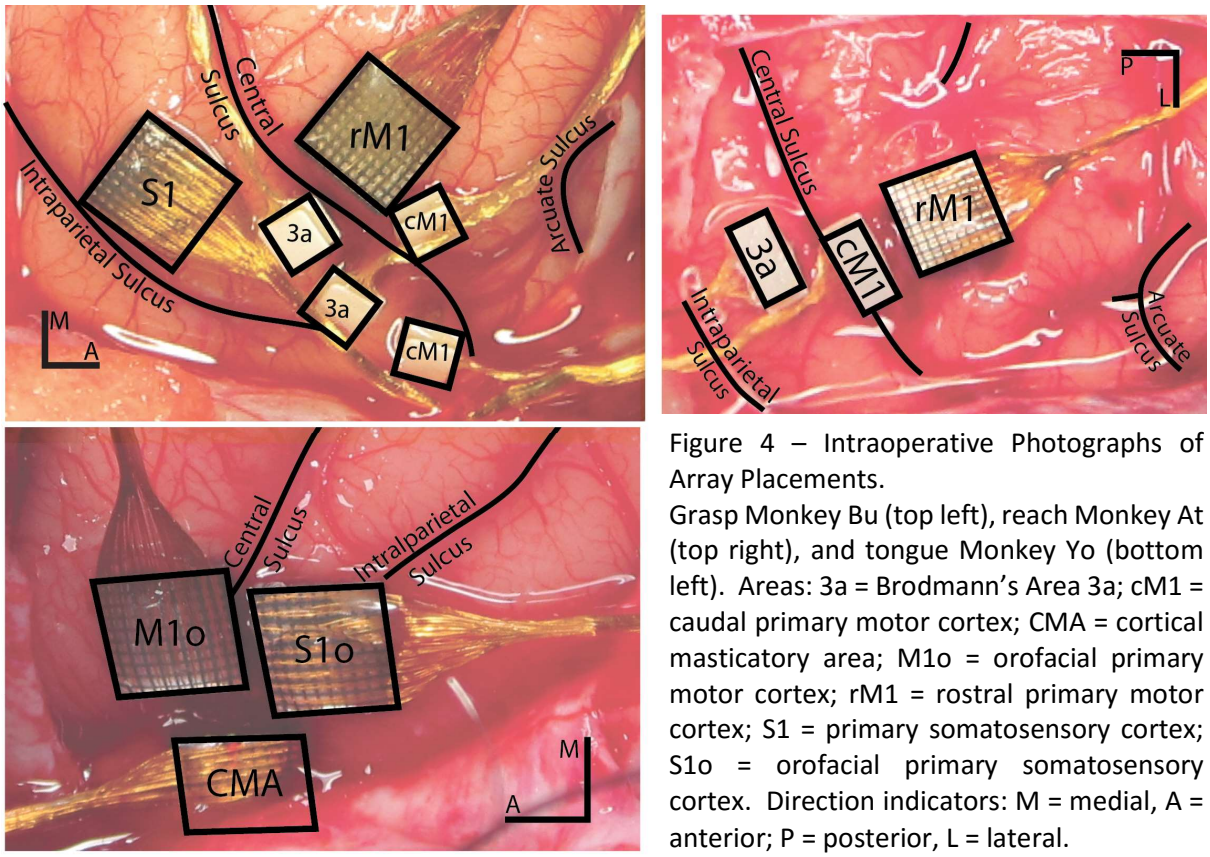

Figure 4 – Intraoperative Photographs of Array Placements.
Grasp Monkey Bu (top left), reach Monkey At (top right), and tongue Monkey Yo (bottom left). Areas: 3a = Brodmann's Area 3a; cM1 = caudal primary motor cortex; CMA = cortical masticatory area; M1o = orofacial primary motor cortex; rM1 = rostral primary motor cortex; S1 = primary somatosensory cortex; S1o = orofacial primary somatosensory cortex. Direction indicators: M = medial, A = anterior; P = posterior, L = lateral.

FMAs targeted the hand representation of cM1 and area 3a. The area 3a recordings were poor and are not included in the following results or analyses.

Reach Monkey At had one Utah array and two 36-electrode FMAs implanted (Figure 4). The Utah array targeted the elbow and shoulder representations of rM1, one FMA targeted these representations in cM1, and the other in Area 3a. As with Monkey Bu, the Area 3a recordings were poor and are not included here.

Tongue Monkey Yo received three Utah arrays: one in M1o, one in S1o, and one in cortical masticatory area (CMA) (Figure 4). Although all other Utah arrays had electrodes with 1.5 mm in length, the S1o array's electrodes were 1.0 mm in length. The CMA data are not included in the following results or analyses.

FMA Design

Each FMA was customized for its given anatomical target and the respective somatotopic target. To do so, first magnetic resonance imaging (MRI) scans were conducted at the Brain Imaging Research Center at the University of Chicago. The detail scans were conducted at 0.7 mm along the parasagittal plane. The imaging results were entered into Analysis of Functional NeuroImages software (AFNI, NIMH, Bethesda, MD). Images in the coronal, sagittal, horizontal axes were then extracted and imported into Adobe Illustrator (Adobe Systems Incorporated, San Jose, CA). The cortical surface and the gray-white matter border surrounding the arcuate, central, and intraparietal sulci were drawn on each section. Transparent images of these outlines were then imported into SketchUp (Trimble Navigation Limited, Sunnyvale, CA). In SketchUp, a wireframe-like model was constructed from the line drawings of the cortical features. Mockups of Utah arrays and FMAs were made to scale within the SketchUp software, and placed on the models' surfaces. Individual electrodes for each FMA were extruded so that the array spanned, in as many dimensions as possible, the hand or arm representation of cM1 (and area 3a). Finally, the location and orientation of the array substrate was noted in relation both to stereotactic ear-bar coordinates and cortical surface features to assist in surgical implantation.

Surgical Implantation

Having been administered atropine preoperatively (0.04 mg/kg, IM), NHPs were anesthetized with a mix of ketamine hydrochloride (2-3mg/kg, IM) and dexmedetomidine (75 µg/kg, IV), placed in a stereotaxic coordinator (Kopf Instruments, Tujunga, CA), and intubated. Anesthesia was maintained with isoflurane (1-3%). IV fluids and remifentanil (0.1-0.5µg/kg/min) were delivered throughout the procedure.

Utah array and FMA target locations were based on MRI scans, stereotactic coordinates, and surface anatomy of the sulci and gyri. For Monkey Bu and Monkey Yo, projection fields in motor cortex were initially estimated with a brief intraoperative session of microstimulation. In all monkeys, receptive

fields in somatosensory cortex were verified postoperatively by palpating the respective body parts and monitoring the multiunit activity of each electrode visually and auditorially.

FMAs were implanted before the Utah arrays to ensure that deformation of the cortical tissue during the long insertion procedure did not dislodge the Utah arrays.

Neural Recording Procedures

All neural recordings were performed with Cerebus neural data acquisition systems (Blackrock Microsystems). Electrode signals were amplified 5000x, band-pass filtered between 0.3 Hz and 7.5 kHz, and recorded digitally (14-bit) at 30 kHz per channel. Unit spiking waveforms of 1.6 ms duration (48 sample time points per waveform) that crossed a voltage threshold (set just above the noise band) were saved and single unit signals were sorted using Offline Sorter (Plexon, Dallas, TX). LFPs were sampled at 2 kHz. Data files were imported into MATLAB software (Mathworks, Natick, MA) using the Neural Processing MATLAB Kit (Blackrock Microsystems). All subsequent processing and analyses were done in MATLAB with custom code and code modified from the Chronux open-source software package (chronux.org).

Tasks

Each of the three animals performed a different task: Monkey Bu grasped objects with minimal arm movement; Monkey At reached in a two-dimensional plane; Monkey Yo exerted tongue force within a specified range.

Grasp

The goal of this task was to have a monkey grasp a variety of different objects using only its wrist and hand, rather than a full reach-to-grasp movement involving the entire upper limb (Figure 5).

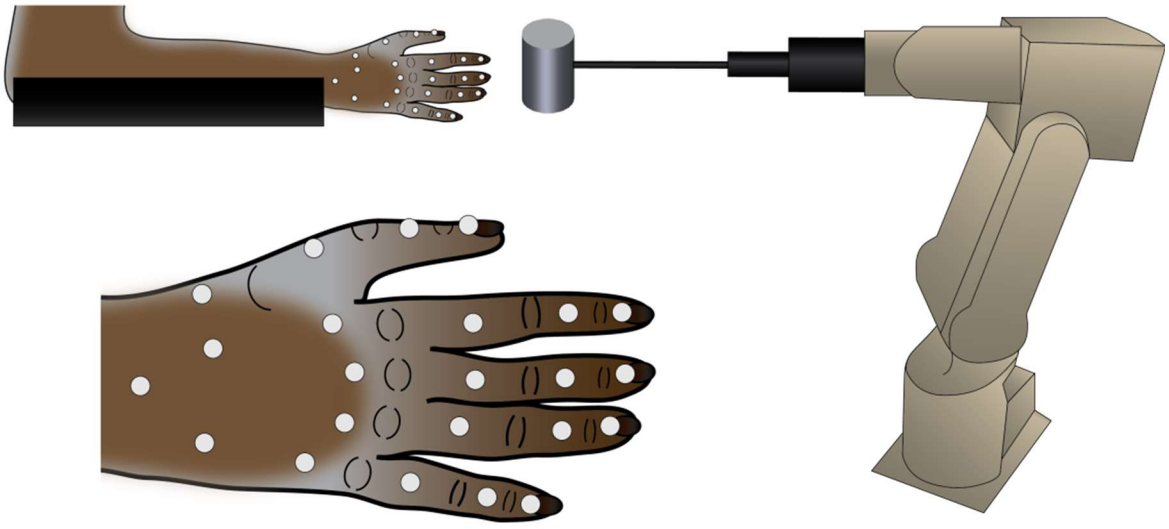

Figure 5 – Experimental Setup for the Grasp Task.
Monkey Bu's arm is depicted in the arm rest with reflective markers affixed to the hand. The enlarged view below shows the detailed location of the hand markers, spanning each joint on the fingers, and most hand joints. The 6-axis is depicted at right (not to scale with the hand), as it approaches the hand with the object. See Figure 6 for a photograph of the objects.

Accordingly, Monkey Bu was trained to sit in a primate chair while resting his arms on arm rests. Light sensors embedded in the arm rests detected if the arms moved. If so, the trial aborted and repeated.

As a six-axis robot (RV-1A-SI1, Mitsubishi Corporation, New York, NY) presented one of 35 objects to his hand, he would grasp it. The robot would retract, and the monkey exerted isometric counter force to break the magnetic connection between the robot and the object. If the monkey did not move his arm (as detected by the light sensors) and the object was not detached prematurely, the monkey received a juice reward and the next trial began. Objects were presented in a pseudorandom order on a trial by trail basis for at least 10 repetitions of each of the 35 objects.

Objects

Each object was made in the University of Chicago Student Machine Shop. Each object has a base, a stem, and the shape (Figure 6). The base of each object is a 1" cube of black plastic polyoxymethylene with a bar of magnetic metal at the end opposite the stem. The stem is a threaded rod attached to the

Figure 6 – Photograph of the Objects Used in the Grasp Task.
Each object is composed of a magnetic base, threaded rod, and plastic shape. Note that some shapes can be presented in either a horizontal or vertical position, and so were considered as different objects.

base with a set screw against a flattened segment of the rod. Each shape has a tapped hole into which the stem is screwed. In order for the objects to be presented to the primate's hand at the same distance, the stems were shortened so that every object has the same overall length, from the beginning of the base to the tip of the shape.

The robot was affixed with a magnetic device that allowed the objects to be rapidly reattached in exactly the same position and orientation between trials. The base of an object fit snugly into the support, and was secured with two rare earth metal magnets. A light sensor in the support detected the presence or absence of an object, and communicated with the experimental software.

Vicon

In order to record the kinematics of the movements we used a 10-camera motion tracking system (VICON, Oxford, UK) and affixed reflective markers to the monkey's arm, wrist, and hand. The system tracked the three-dimensional position of the markers at 250 Hz, and received a synchronizing pulse to

line up the kinematic data with the neural data. 30 markers were placed on the upper arm, forearm, hand, and phalanges in order to bridge the elbow, wrist, and each digit joint, allowing all joint angles of the upper limb (excluding shoulder) to be calculated. A Sony HandiCam (Sony Corporation of America, New York, NY) also recorded the task and were encoded with the Vicon data files to provide a visual review of the task.

OpenSim and Kinematics

In order to calculate the joint angles and velocities from the above Cartesian marker positions, OpenSim software (Simtk.org, Stanford CA; [66]) was used that incorporated a customized biomechanical model based on a musculoskeletal model of the human upper extremity [67]. The model used here had every bone scaled appropriate to macaque proportions, based on multiple still frames of Monkey Bu. Additionally, the range of motion of each joint was adjusted to match the range of motion of Monkey Bu. The markers were accurately positioned on the skeletal model in the software, to match the marker positioning on the animal. Based on the movement of these markers from VICON software, and the musculoskeletal constraints from the OpenSim model, the inverse kinematics could be calculated from the position of the markers at each time-frame. Angular positions and velocities were calculated for elbow flexion and extension, forearm pronation and supination, wrist flexion and extension, and wrist adduction and abduction (deviation). Within the hand, the carpal-metacarpal joints of digits four and five (D4, D5) were given minimal flexion. For each digit, D1-5, the metacarpal-phalangeal joints had both flexion/extension and deviation. Digits 2-5 had both proximal and distal interphalangeal joint extension and flexion, but D1 only had distal interphalangeal joint extension and flexion. Note that the thumb only has two phalangeal bones, and so no distal interphalangeal joint exists. The OpenSim software exported this joint position data into a MATLAB-readable format.

Within MATLAB, the 250 Hz kinematic data were bidirectionally filtered with a fourth-order Butterworth low-pass filter with a 6 Hz cutoff to reduce noise artifacts.

Reach

The goal of this task was to have a monkey make two-dimensional arm movements, navigating a cursor through a series of targets before receiving a reward. The monkey was positioned in a two-link robotic exoskeleton (KINARM, BKIN Technologies, Inc, Kingston, Ontario, Canada) in front of a projector, and trained to move a cursor on the screen through targets by moving the end point of the exoskeleton. The movements were constrained to a two-dimensional, horizontal plane, and the monkey was only able to move her shoulder and elbow. There were 9 possible targets arranged in a 3x3 square. Targets were selected at random, and the monkey was trained to move a cursor through each target in succession, as

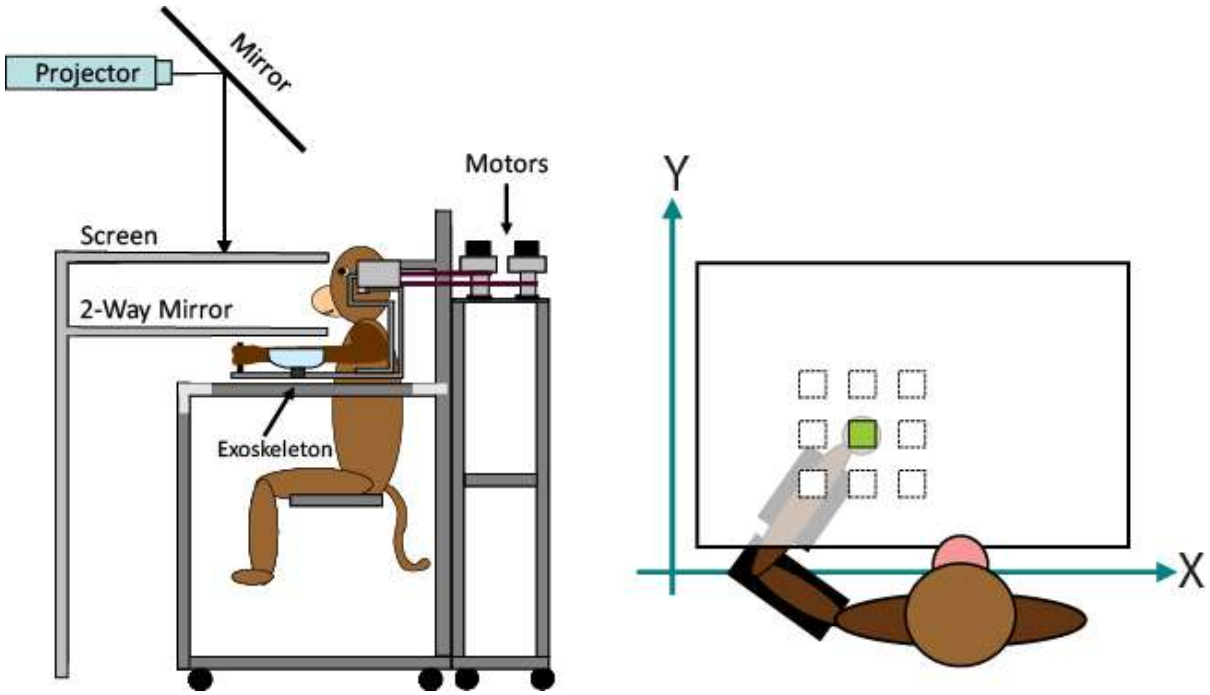

Figure 7 – Cartoon Depiction of the Reach Task.
Left: side view of the experimental setup for the reach task. The left arm is resting in an exoskeleton, and the and is holding a cursor. While the arm is in the exoskeleton, it is constrained to horizontal movement in two dimensions. Right: top view of the monkey and display area. Different targets lit up one at a time, and the monkey moved the cursor through the targets as they appeared. See Suminski et al, 2010 for further details [68].

they appeared. After a successfully navigating 3-5 targets, the monkey received a juice reward. See Suminski et al, 2010 for further details [68].

Tongue

The goal of the tongue protrusion task was for the monkey to use his tongue to exert a specified amount of force on a force transducer (Model 462-D3-2-10P1R, Revere Transducers, Tustin, CA). The monkey sat in a primate chair in front of a computer monitor with the force transducer in front of its mouth. It was trained to protrude the tongue and exert the required amount of force to move a cursor along a one-dimensional axis into the target (Figure 8). A successful trial resulted in a juice reward. Between trials, the tongue could either rest on the transducer or be retracted. See Arce et al, 2014 for further details [69].

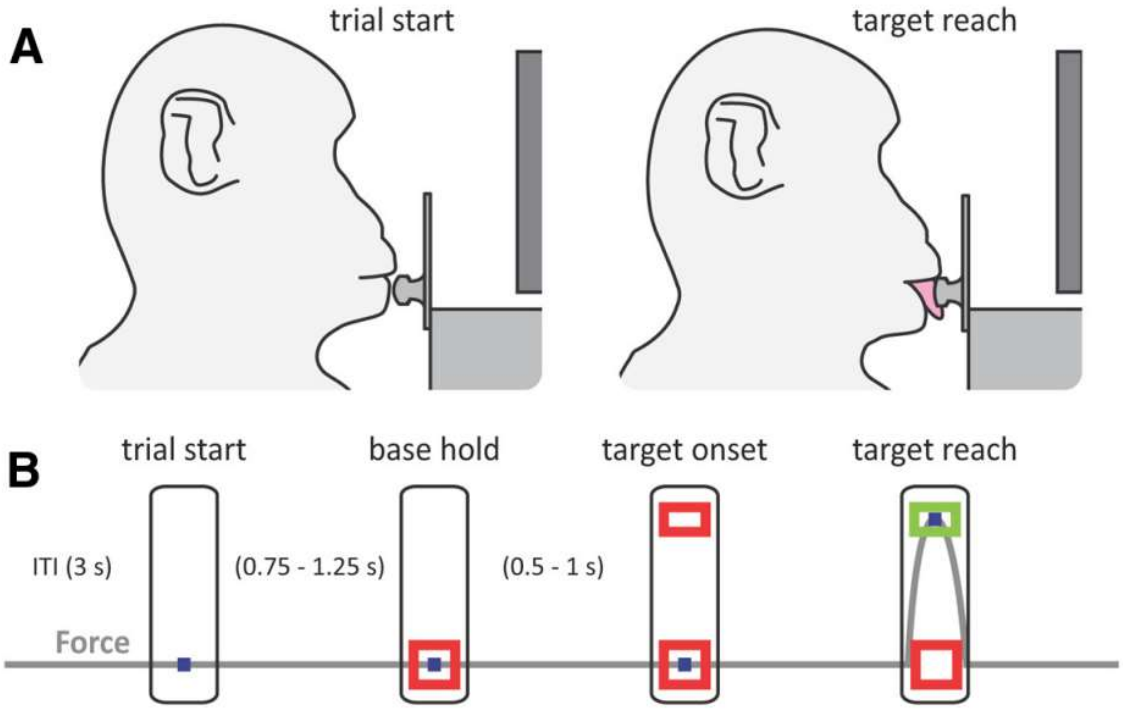

Figure 8 – Diagram Representing the Sequence Events in the Tongue Force Task for Each Trial. A monitor in front of the monkey shows the force cursor (blue), base window (red), and target window (green when reached) of force, similar to shown below in B. See Arce et al 2014 for further details [69].

Kinematics

Although detailed kinematics or kinetics were recorded and processed for all tasks, the primary function of these data were to tabulate key time-points to facilitate the analysis of the neural data. For the grasp task, data were aligned to movement onset. Reach data were aligned to the time the cursor hit the target. Tongue data were aligned to force onset.

The time of grasp movement onset was calculated based on wrist flexion, and first, second, and third metacarpal-phalangeal joint velocities. Movement onset for each joint is the first time-point to exceed 20% of maximum velocity prior to time of contact, where time of contact was marked by watching the video recording and scoring the event in the VICON software. Grasp movement onset was the earliest joint movement onset.

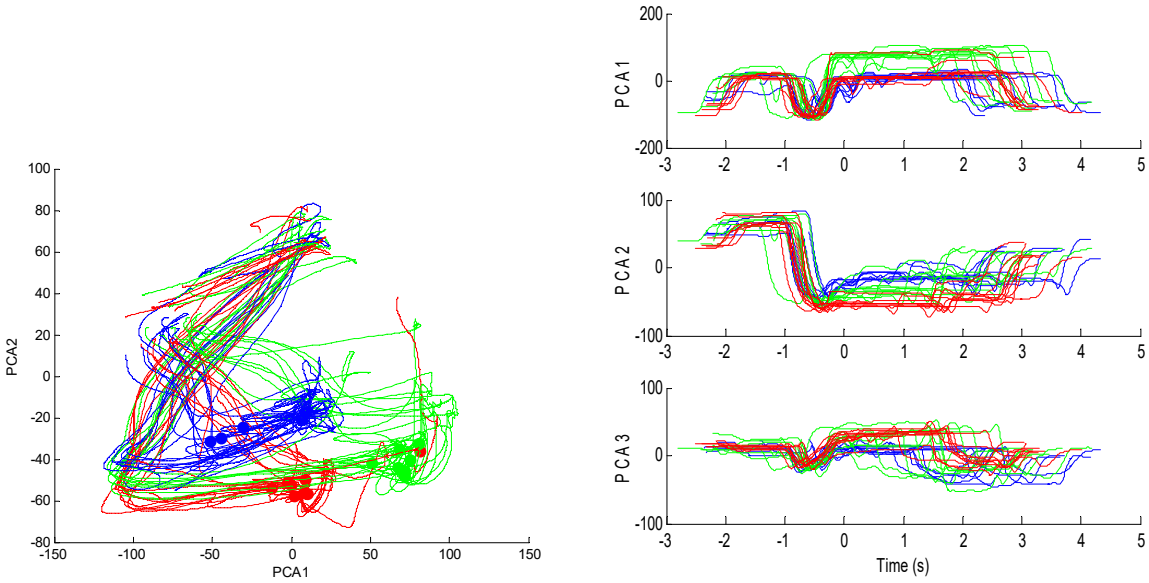

Figure 9 – Example Grasp Kinematics.
Kinematic examples for 10 trials each for 3 different objects. Each object is a different color. Kinematics are displayed in principal component space. The left plot shows the time-varying kinematics in the first two principal components, and the right plot shows each of the first three principal components as a function of time. Note that there is more variability in trajectories and end points in principal component space between objects than within objects.

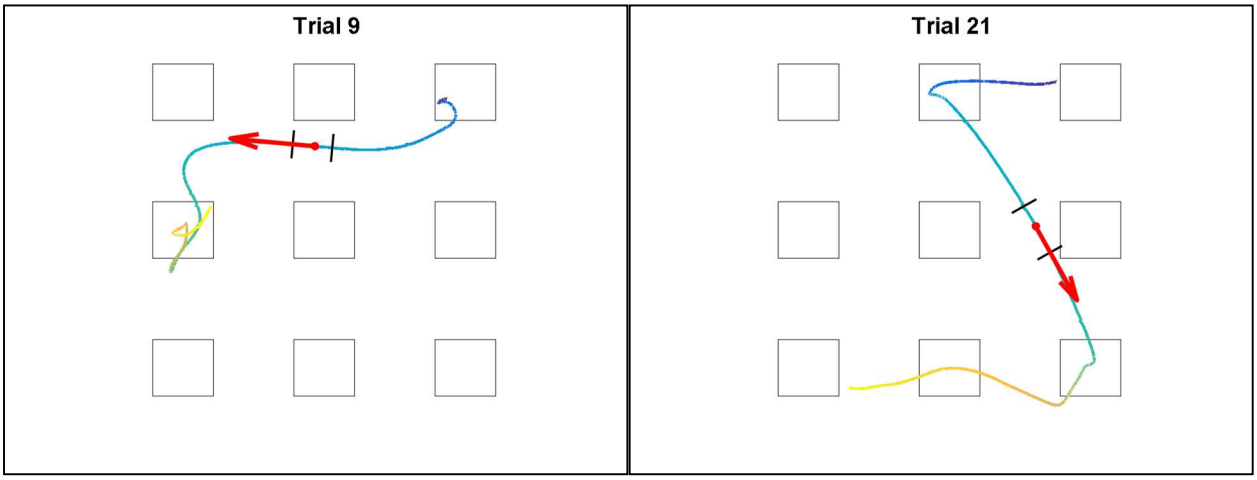

Figure 10 – Examples of Reach Cursor Trajectories and Movement Direction at Maximum Velocity. Time is indicated as the color of the trajectory, from one second prior to target hit (blue) to one second after target hit (yellow). Direction at the time of maximum velocity is indicated by the red arrow. The black lines show the time period over which direction was calculated, 20 ms surrounding maximum velocity. Note that trajectories may span multiple target hits.

Due to the ongoing nature of the reach task, pinpointing the time of movement onset for each target was a non-trivial challenge. Instead, data were aligned when the cursor reached the target and a new target was displayed.

Tongue force onset was marked when tongue force last exceeded 1 gram, prior to reaching two-thirds of peak force (Arce 2013).

Example kinematics for each task are shown in Figure 9, Figure 10, and Figure 11. To reduce any effects of variability due to differing kinematics or direction, some analyses were calculated within each object (grasp) or movement direction

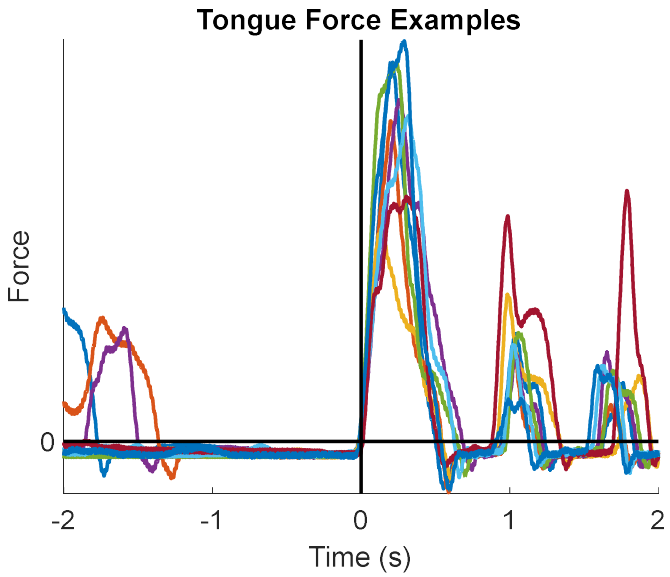

Figure 11 – Examples of Tongue Force. Eight randomly selected trials within one recording session of 401 trials. Time zero indicates force onset. Note the similar profiles of the force generated within each trial.

(reach). Movement direction for the reach data was calculated as the average direction within 20 ms of the time of maximum cursor velocity prior to target acquisition was found, and sorted into 12 discrete direction bins. Note that the force profiles for the tongue task were highly stereotyped, and therefore grouping trials was unnecessary.

Single-Unit Analyses

All single-unit analyses were performed in MATLAB using custom code. The frequency spectra of the LFP signals used modified code from the Chronux toolbox.

Neuronal Modulation

Only neurons that modulated during the task were used for all subsequent analyses. The criterion for task modulation was that each neuron's trial averaged firing rate was outside of the 98% confidence interval of baseline firing for at least 50 milliseconds. The baseline period was one second, beginning at two seconds before movement onset, target acquisition, or force onset, as appropriate. Firing rates were calculated in 10 millisecond bins.

Firing Rate Comparisons

Maximum and mean firing rates were calculated for each neuron and the distributions compared across cortical areas. A one-way ANOVA test between cortical areas compared the mean firing rates of all neurons within each area.

Local Field Potentials

To demonstrate that frequency spectra of the local field potentials in each cortical area modulate strongly during each task, the population spectrogram was calculated. The demeaned spectral power was computed within distinct frequency band as a function of time. The frequency bands used were Theta (2-

6 Hz), Alpha (7-15 Hz), low Beta (16-30 Hz) and high Beta (31-45 Hz). This analysis emphasized the task modulation within each frequency.

More specifically, the spectral contents of the local field potential signals were calculated in 500 ms windows, stepped by 10 ms through the 4 seconds surrounding movement onset or target acquisition, across 5 tapers using a multi-tapered fast Fourier transform algorithm. The power spectra were then averaged across each cortical area, and demeaned within each frequency band.

Coherence Analyses

Spectral analyses such as coherence were calculated in MATLAB using custom code and modified versions of the Chronux toolbox.

Spike-Field Coherograms

In order to determine which frequency ranges were reliably task modulated, spike spectrograms, field spectrograms, and spike-field coherograms were calculated using multi-tapered fast Fourier transforms. Sliding windows of 500 ms were used, with 10 ms steps and 5 tapers. The frequencies inspected ranged from 2 to 45 Hz. The lower bound is determined by the duration of the sliding windows, and the upper bound by the presence of a significant 60 Hz line noise signal.

Auto- and cross-spectra can then be calculated from the fast Fourier transformed data as the product of the spike spectra and the conjugate of the LFP spectra in each time-frequency bin:

$$S_{sf} = J_s^* J_f$$

Coherence, then, is the magnitude of the cross-spectra divided by the square root of the product of each auto-spectra, as below:

$$Coh_{sf} = \left| \frac{S_{sf}}{\sqrt{S_{ff} S_{ss}}} \right|$$

The above calculations were performed on every neuron-channel pair between the cortical areas. For example, coherence was calculated between every task-modulating neuron in cM1 and every LFP channel in rM1, and every task-modulating neuron in rM1 and every valid LFP channel in cM1 for the grasp and reach data.

Trial Shuffling

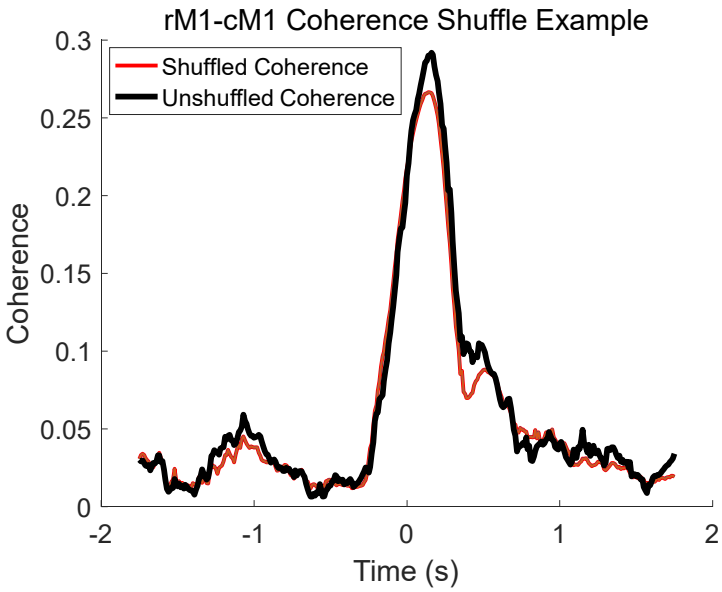

Figure 12 - Trial Shuffling Example.
An example of the unshuffled (black) and trial-shuffled (red) spike field coherence for an individual rM1-cM1 spike-field coherence pair. The red trace shows the average and the variance of the 100 trial-shuffled pairs, and the black trace shows the unshuffled spike-field coherence.

Trial shuffling was used to ensure that coherence values were not a result of chance. For each neuron-channel pair, coherence was also calculated between the same LFP data and trial-shuffled spike data. Unshuffled "real" coherence values and the trial-shuffled coherence were compared for each neuron-channel pair as follows: first, the time and value of the maximum of the real coherence was found; if this value was greater or equal to 95% of the trial-shuffled coherence values at the same time, the coherence was considered to be "significantly task-modulating," as in "unlikely to have occurred by chance," and kept. If the real value did not exceed this threshold, the coherence values were not used in subsequent comparisons. A percentage of "significantly task-modulating" pairs was calculated as the number of modulating pairs to the total number of possible pairs. An example of the trial shuffling is shown in Figure 12. Note that the unshuffled spike-field coherence is consistently higher than the shuffled spike-field coherence, and especially so at the peak of coherence near movement onset.

To assess significant coherence above which could be attributed to common modulation of the constituent signals, trials were shuffled within subsets of similar trials. The grouping for similar trials is as described above. For the grasp data, each object induced the monkey to use highly similar kinematics of the hand and wrist, and so data were shuffled among trials with the same object. For the reach data, the average direction within 20 ms of the time of maximum cursor velocity prior to target acquisition was found (Figure 10). These directions at maximum velocity were sorted into 12 discrete bins, and trials were then shuffled within each direction bin. For the tongue force task, however, the kinematics were highly similar between trials (Figure 11), and so required no such restrictions on the trial shuffling.

Population Spike-Field Coherence

To compare the different populations of spike-channel pairs, the distributions of the maximum value of coherence were compared. One-way ANOVA tests between cortical areas compared the peak value distributions. As before, one asterisk indicates a p-value between 0.05 and 0.01; two, between 0.01 and 0.001; three, below 0.001.

Coherence Cross-Correlations

To compare the timing of the population spike-field coherences, a cross-correlation analysis between subsets of the spike-channel coherence pairs was performed. The data were subsampled for 1000 iterations at 10 percent of spike-channel pairs per iteration. Cross correlation was calculated for each iteration's subset of data. The distributions of the lag time of the peak correlation for each iteration were found, and used as a measure of which coherence occurred first, and by how many milliseconds. Note that the time resolution is limited by the 10 ms step size used in the calculation of the coherence, and the 500 ms data windows.

Divergence and Convergence of Coherent Connections

To examine the structure of connections between areas, specifically the divergence and convergence of the coherent connections, I calculated the proportion of coherent pairs to the possible number of coherent pairs. For each neuron, divergence is calculated as the number of LFP channels with which it was coherent divided by the total number of LFP channels with which it could be coherent. For example, a neuron in caudal M1 could be coherent with up to 96 LFP channels in rostral M1, the number of electrodes on a Utah array. Similarly, the convergence is calculated as the number of neurons a given local field potential is coherent with, scaled by the number of neurons in the projecting area.

III. Investigating the Hierarchical Functional Organization of Subdivisions of Primary Motor Cortex in Reaching and Grasping Behaviors

Introduction

Primary motor cortex is known to be critical to generating movement of the arm and hand, as evidenced by its descending projections, somatotopic organization, neural activity, and results of electrical stimulation and perturbation studies. It also receives significant sensory input, both from the periphery and from primary somatosensory cortex. However, there are important differences in these properties between the rostral (rM1) and caudal (cM1) subdivisions of primary motor cortex.

This section explores the differences between single neurons and populations of neurons simultaneously recorded in rM1 and cM1, and the coordination between these critical cortical regions in the context of naturalistic movements of the arm and hand. Spike-field coherence analyses are used to answer three questions: are these subdivisions coordinated, is the coordination dynamic and task-modulated, and what is the structure of this coordination?

The coherence analyses found bidirectional, task-modulating coordination between the subdivisions of motor cortex, suggesting ongoing interactions before, during, and after movement onset. Further, although the rM1-cM1 spike-field coherence leads the cM1-rM1 coherence, the cM1-rM1 coherence is stronger, cM1 neurons are more divergent, and cM1 fields receive more convergent inputs. Together, these findings suggest that although cM1 has a strong feedback influence on the population activity of rM1, rM1 may indeed be higher in the motor cortical hierarchy than cM1.

Descending Projections

Primary motor cortex is the main source of corticospinal tract projections. Monosynaptic projections from M1 to motoneurons in the ventral horn of the spinal cord have been implicated in

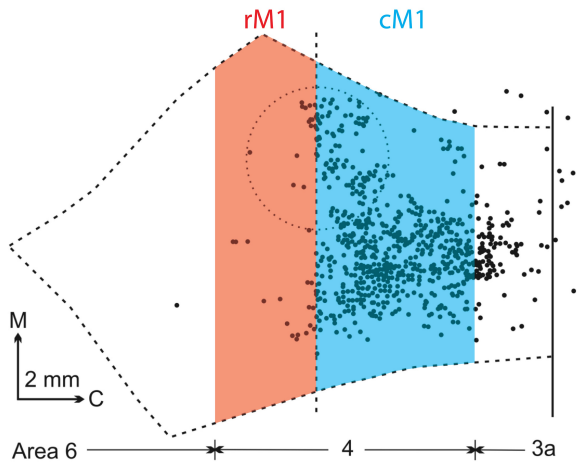

Figure 13 – Distribution of Corticomotoneuronal Cells in Rostral and Caudal Motor Cortex.
Each dot represents the cell body location of a corticomotoneuron innervating a digit muscle. Red shaded portion indicates rM1; blue shaded, cM1. Modified from Rathelot & Strick, 2009 [20].

dexterous movements of the fingers [70]. These corticomotoneuronal (CM) cells in M1, are involved in the control of finger force [71]. These CM cells produce rapid changes in EMG activity in forearm, wrist, and hand muscles [72–74]. Corticomotoneuronal cells have also been identified in humans [75]. Additionally, the projections from rostral and caudal M1 develop differently and project to different areas of the spinal cord [76,77].

Notably, there are differential distributions of corticomotoneuronal cells in rostral and caudal motor cortex (Figure 13). Rathelot and Strick injected retrograde trans-synaptic rabies virus into individual muscles in the shoulder, elbow, hand, and digits, and observed the location of the cell bodies of the CM cells. They found that CM cells are largely restricted to the caudal portion of M1 [20,78]. Therefore, while rostral M1 can only influence motor output indirectly, through spinal cord mechanisms, caudal M1 has more direct influence on the muscles of the upper limb.

The descending projections from motor cortex are also highly divergent, projecting on to multiple muscles, as has been determined through both electrophysiological studies [21,79–81] and anatomical studies [20,82]. In some cases, they even suppress the activity of antagonist muscles [79].

These divergent projections suggest that the motor cortex does not control individual muscles, but rather may control ensembles of muscles [81]. Indeed, these functional groups have been found to increase decoding accuracy [83,84] both for reach and grasp tasks. It is believed that complex movements may be built from simpler motor cortical ensembles [85].

Sensory Inputs

Although primary motor cortex is the main source of descending projections, and therefore motor commands, it is also a target of sensory inputs from the periphery [86–88]. Neurons within M1 modulate their firing in response to both cutaneous and proprioceptive stimulation. However, the distribution of neurons that respond to these different submodalities of stimulation is not uniform across primary motor cortex (Figure 14). Neurons that respond to cutaneous stimulation are predominantly found in caudal motor cortex, and neurons that respond to proprioceptive stimulation are predominantly found in rostral motor cortex [89–92]. Note that although Picard & Smith also found that cutaneous-receptive neurons are mostly found in caudal motor cortex, they found that proprioceptive-receptive neurons were found more evenly distributed through motor cortex [90].

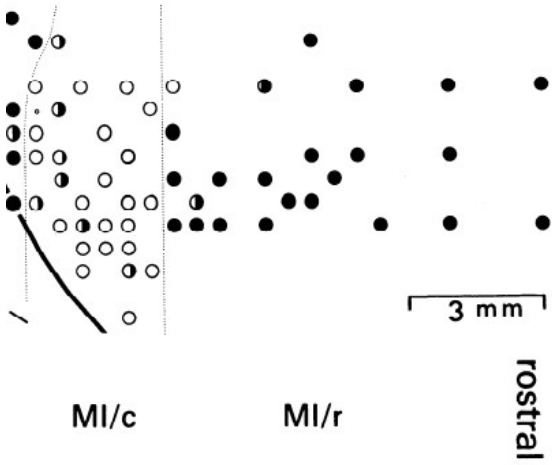

Figure 14 – Submodality Segregation in the Primate Motor Cortex.
Dotted lines separate the cortical areas; solid circles indicate locations of noncutaneous units; open circles indicate locations of cutaneous units. Tanji & Wise, 1981 [92].

Architectonics and Connectivity

In addition to the differences in descending projections between rostral and caudal motor cortex, there are differences in their architectonics, cortical connections, and subcortical connections [19,93]. Further, rM1 and cM1 are densely interconnected within, and weakly interconnected across, limb representations [16].

Motor cortex is not uniform in cell type composition across its rostral-caudal axis. Caudal motor cortex has larger pyramidal cells than rostral motor cortex [19]. The effects and significance of this

difference has yet to be elucidated. For example, larger cell bodies do not correlate well will longer axons, and therefore it is not a function of the location in the spinal cord. However, it is a feature that may be used to delineate between the two subdivisions, anatomically.

The subdivisions of motor cortex are densely interconnected. Huntley and Jones [16] injected neuroanatomical tracer into ICMS-defined thumb representations in both rostral and caudal motor cortex, and found dense bidirectional connections between the subdivisions of motor cortex. Further, the thumb representations were strongly connected to different forelimb movement representations across the entire forelimb, including digits, wrist, elbow and shoulder. These divergent connections may be recruited during complex movements to coordinate the activity of forelimb muscle groups. The connections between representations of different body parts exist, but are more limited.

Further, these interconnected representations also have different ipsilateral cortical connections [19]. Rostral motor cortex is densely connected with non-primary motor cortex, as well as somatosensory cortex, whereas caudal motor cortex is primarily connected with somatosensory cortex. Within somatosensory cortex, rostral motor cortex receives input preferentially from Brodmann area 2, and to a lesser extent, areas 1 and 3a, whereas caudal M1 receives input from predominantly from areas 3a and 1, and to a lesser extent 2 and 3b. Therefore, the strongest inputs to rostral M1 from S1 are from the proprioceptive area 2, and the strongest inputs into caudal M1 are from adjacent 3a and cutaneous area 1.

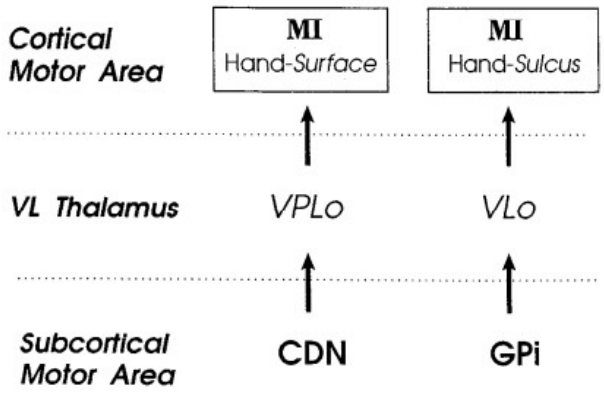

Figure 15 – Thalamic Inputs into Subdivisions of Motor Cortex.
Surface rostral M1 receives inputs primarily from VPLo, which in turn receives cerebellar input. Sulcal caudal M1 receives inputs primarily from VLo, which in turn receives palladial inputs. Holsapple, Preston, Strick, 1991 [93].

Additionally, the hand representations of the subdivisions of primary motor cortex

receive different thalamic inputs [93]. As shown in schematic in Figure 15, rostral M1's hand representation receives most of its thalamic input from VPLo (Ventralis Posterior Lateralis pars oralis), whereas caudal M1's hand representation receives most of its thalamic input from VLo (Ventralis Lateralis pars oralis). Furthermore, these thalamic nuclei are known to have different cerebellar and basal ganglial inputs: cerebellar nuclei project to VPLo, but not VLo; the globus pallidus internus (GPi) projects to VLo. It is beyond the scope of this dissertation to speculate on the excitatory role of the cerebellum on the thalamic nucleus VPLo, and therefore rostral motor cortex, or the inhibitory role of the GPi on the VLo, and therefore caudal motor cortex, except to say that the VLo may provide the basal ganglia with direct access to the hand representation primary motor cortex that it does not have to other limb representations.

Somatotopy

Rostral and caudal motor cortex have different but complementary somatotopic maps of the contralateral body. Although this has sometimes been described as a horseshoe organization [25,94], with distal joints represented in a core focused in caudal M1, surrounded by concentric horseshoes of increasingly proximal joints [22], nonetheless each subdivision contains its own complete body map (Figure 16). Note that caudal M1 has a disproportionately large representation of distal muscles. This is similar to the increased amount of cortical real estate dedicated to the hand, arm, and face in area 2 compared with areas 1 and 3b. That is

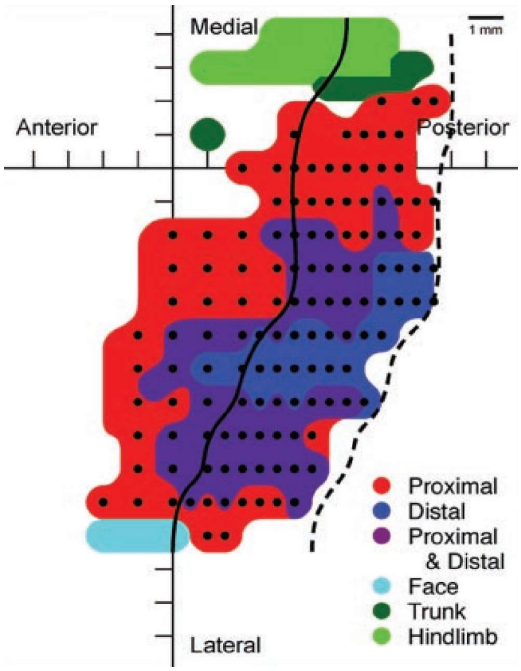

Figure 16 – Map of Contralateral Limb Muscles in Primary Motor Cortex.
Black dots indicate locations of electrode penetrations. Surrounding color indicates the location of the muscles that showed stimulation effects in EMG activity. Park & Cheney, 2001 [94].

not to say that the hand is not represented in rostral motor cortex, nor that the proximal shoulder and elbow are not represented in caudal motor cortex.

An important detail of maps of primary motor cortex is that, unlike somatosensory cortex, the maps are far more overlapping and distributed. For example, representations of contiguous joints may be found on adjacent or even the same electrode penetration. The cortical territories for corticomotoneuronal cells for different muscles often overlap [13], and representations of individual fingers are widely distributed in motor cortex [95]. This contrasts with primary somatosensory cortex, especially areas 3b and 1, where the representations are largely distinct [26].

Motor Hierarchy

The above studies provide substantial evidence that there are fundamental differences between rostral and caudal motor cortex, from the evolutionary history, architectonics, anatomical connectivity, and somatotopy. However, some functional differences have yet to be established. Here, I attempt to use correlational analyses to establish caudal M1's position in the motor cortical hierarchy. Van Essen [1], in his famous study analyzing distributed hierarchical cortical processing, used laminar connections to establish if a given cortical area provided forward or feedback connections. Forward connections are defined by terminations into the middle cortical layers, whereas feedback connections are defined by terminations into high and lower cortical layers (Figure 1). Unfortunately, the only two prior studies that have investigated anatomical connectivity between subdivisions of primary motor cortex focused on flattened projections of cortex, and so were unable to reliably identify cortical layers [16,19].

Nonetheless, based on caudal M1 having a higher proportion of direct descending projections to motor neurons, I hypothesize that rostral M1 is hierarchically superior, and therefore sends forward connections to caudal M1, and that caudal M1 sends feedback projections to rostral M1. In this dissertation, the correlative analysis used to address this hypothesis is spike-field coherence.

Here I find that “new M1” seems to influence “old” M1 more than old M1 influences the new. The cM1-rM1 coherence is stronger, both at peak, and baseline. However, rostral M1 exerts its influence on caudal M1 earlier, suggesting that it may be higher in the motor cortical hierarchy.

Results

Single Unit Analyses

The following results are from analyses performed comparing single unit responses and population responses in rostral and caudal M1. The tasks represented in these data are the grasp (hand) task and the reach (arm) task. Data are from four recording sessions with two recording sessions per task/animal recorded within a week apart and pooled across both recording sessions. Because the two sessions were recorded less than a week apart, it is possible that the same neuron are present in both datasets, but treated as two distinct neurons in the analyses [96].

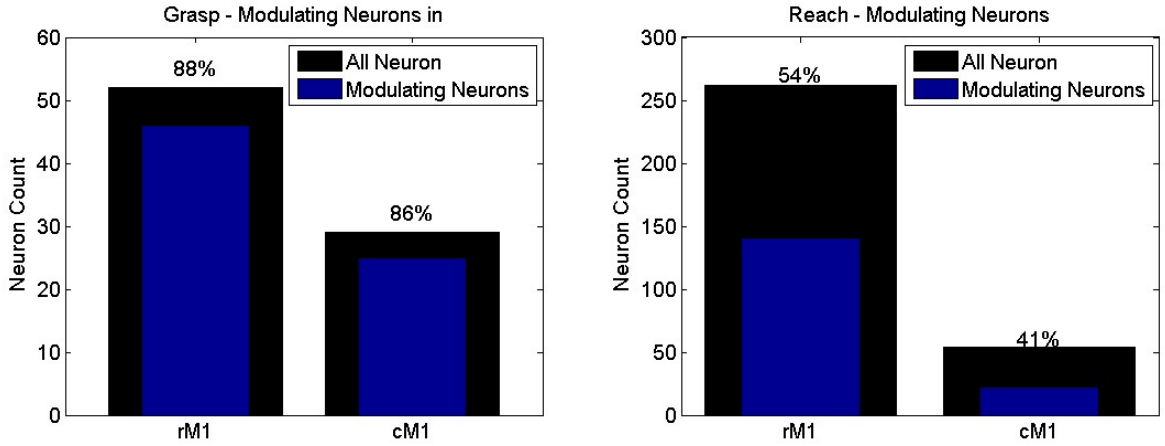

Figure 17 - Task Modulating Neurons.
Bar plots show the total number of neurons recorded in each area (black) and the subset of task modulating neurons (blue). Left: Grasp monkey had 88% of rM1 neurons task modulate; 86% of cM1 neurons task modulated. Right: Reach monkey had 54% of rM1 neurons task modulate; 41% of cM1 neurons task modulated.

Firing Rate Modulation

Neurons in both rostral and caudal M1 were strongly task modulated. For grasp Monkey Bu, in rM1, 88% (46/52) of neurons were task modulated; 86% (25/29) in cM1. For reach Monkey At, 54% of rM1 neurons task modulated, and 41% of cM1 neurons task modulated (Figure 17).

This modulation is clearly seen in the normalized firing rates in Figure 18. The heat maps show trial-averaged firing rate for every modulating neuron in both rostral and caudal M1. Each row in the heat map is a different neuron. The color indicates firing rate, normalized for each neuron to between zero (black) and one (white). The baseline period is the first second shown, from two to one second prior to

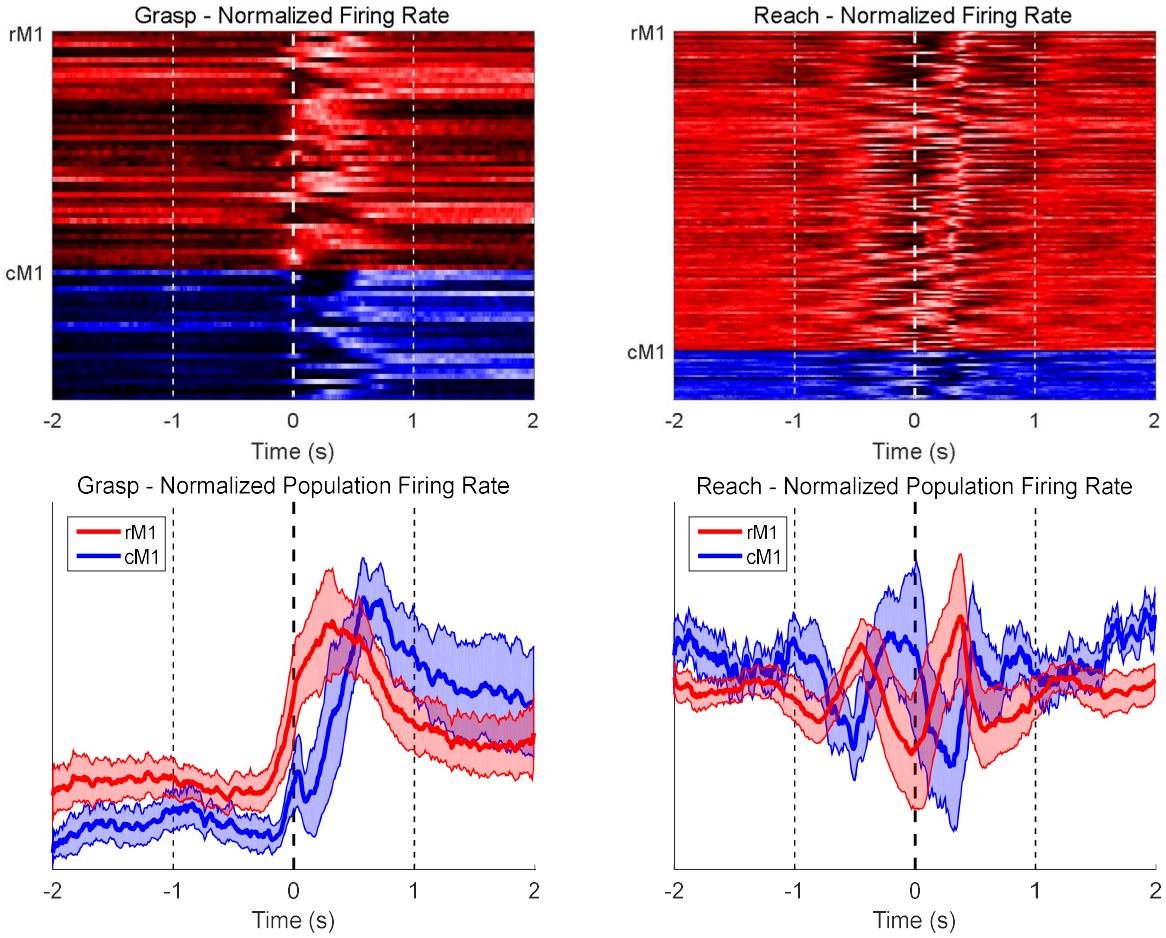

Figure 18 - Normalized Firing Rates and Population Firing Rates.
Top of each figure shows the normalized firing rate of each neuron, divided by cortical area. Bottom of each figure shows the population normalized firing rate for each cortical area. Left: Grasp monkey, aligned on movement onset. Right: Reach monkey, aligned on target acquisition.

movement onset or target acquisition. Note that for the grasp task, most neurons show modulation within one second of movement onset, but for the continuous reach task, the modulation is periodic, reflecting the ongoing nature of the task. Many of the trials will include more than one target reach within the analyzed 4 second window.

The bottom plots of Figure 18 shows the population normalized firing rate for rM1 (red) and cM1 (blue). Note that for the grasp task, although the population of rM1 neurons reaches maximum firing rate first, both populations begin to modulate at approximately the same time. In the reach task, the firing rate modulation is more undulating than in the grasp task; the population responses of rostral and caudal M1 seem out of phase with each other.

Firing Rate Comparisons

This subsection compares the distribution of maximum and mean firing rates of single units in rostral and caudal M1 across both the grasp and the reach tasks.

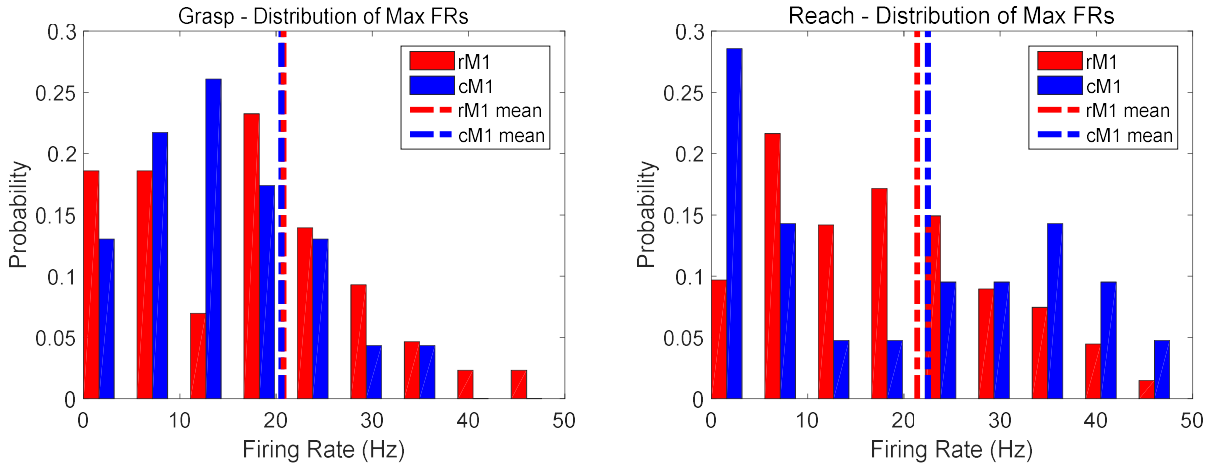

Figure 19 - Distribution of Maximum Firing Rates.
Means of the distributions (dashed lines) are not significantly different in either dataset. Left: Grasp Data; right: Reach data. Red indicates rM1 maximum firing rate; blue, cM1. Data plotted as probability of observed maximum firing rate.

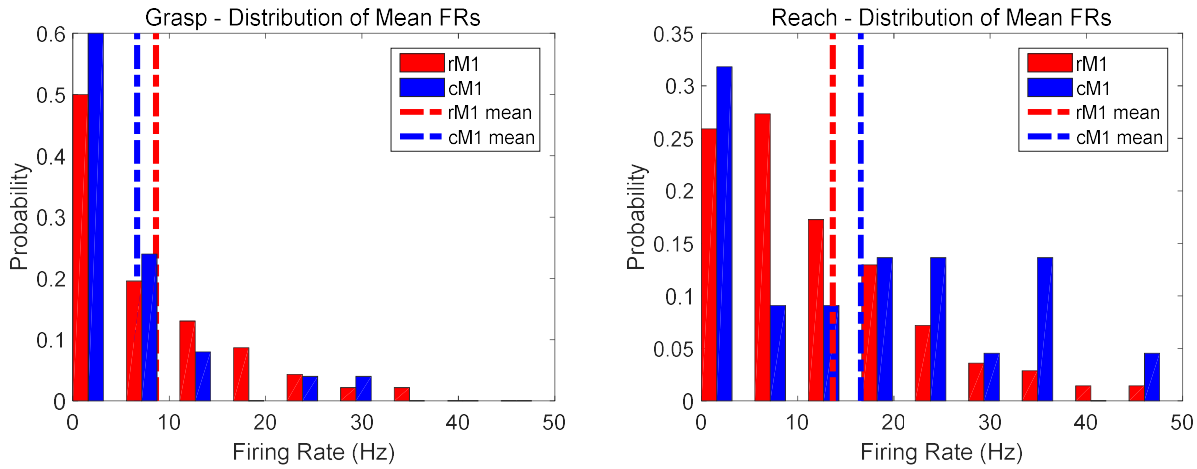

Figure 20 - Distribution of Mean Firing Rates.
Means of the distributions (dashed lines) are not significantly different in either dataset. Left: Grasp data; right: Reach data. Red indicates rM1 firing rate; blue, cM1. Data plotted as probability of observed mean firing rate.

The distributions of maximum firing rates (Figure 19) show that there is no significance difference. Further, the distributions are similar for both the grasp (p-value = 0.96) and the reach (p-value = 0.75) tasks. Similarly, the distributions of the mean firing rates (Figure 20) are also similar between M1 subdivisions for both grasp (p-value = 0.35) and reach (p-value = 0.29) tasks.

Cross-Correlations of Firing Rates

To compare the timing of the firing rates, rather than the magnitude as above, a cross-correlation analysis was performed on the population of normalized firing rate profiles (Figure 21), and examined the time of the peak correlation. The boot-strapped distributions of the time of peak correlation for the grasp and reach tasks are shown in Figure 22. The mean and 95% confidence interval of the grasp distribution

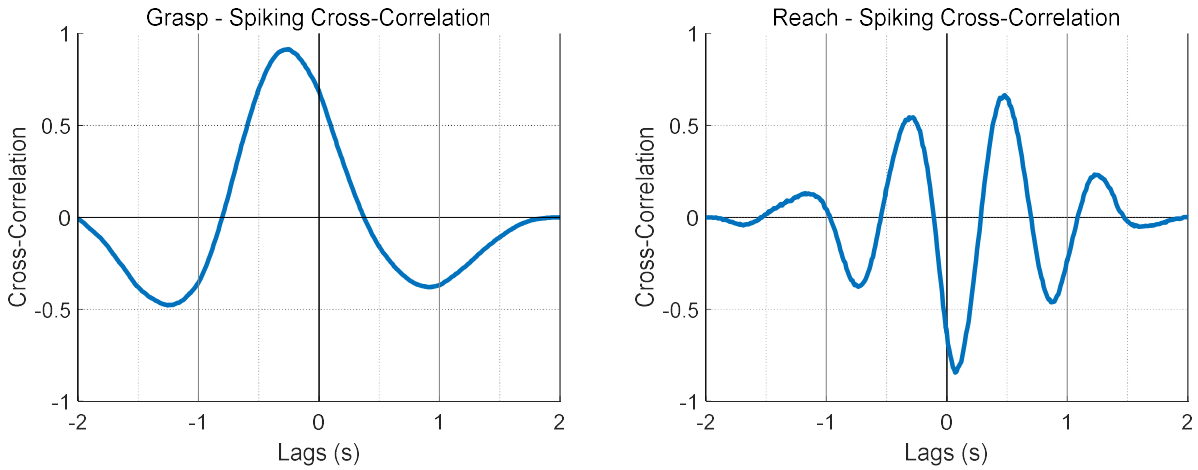

Figure 21 - Spiking Cross-Correlations.
Blue traces represent the population spiking in rostral M1 cross-correlated with the population spiking in caudal M1. Left: grasp data; right: reach data. Blue traces indicate the mean cross-correlation between the population of normalized firing rates in both M1 subdivisions.

are -261 ms and -232 to -289 ms, respectively. The mean and 95% confidence interval of the reach distribution are -289 ms and -243 to -334 ms, respectively.

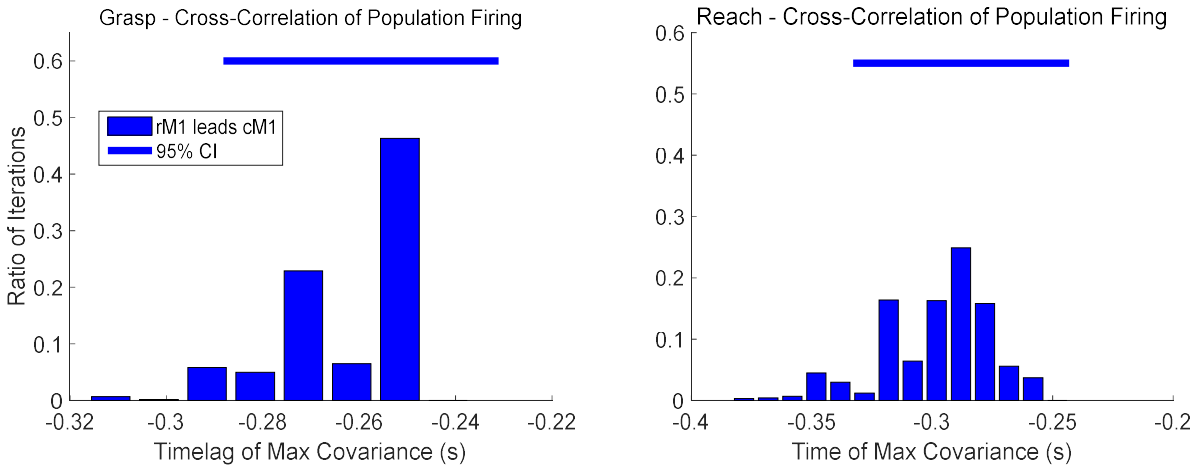

Figure 22 – Distributions of the Time of Peak Cross-Correlation of Population Firing Rates.
Left: Grasp monkey; right: Reach monkey. Horizontal bars represent 95% Confidence Interval for each distribution.

Spectral Analyses

The following spectral analyses were performed on single units and channels in rostral and caudal M1. The coherence analyses explore relationships between neurons in rostral M1 and channels in caudal

M1, and between neurons in caudal M1 and channels in rostral M1. Further, the population spiking and LFPs of each area are compared with each population coherence.

Spectral Content

Figure 23 shows the spectral content of an example rM1 neuron, cM1 channel LFP, and the coherence between them from 0.5 to 45 Hz. The theta band (2-6 Hz) shows clear task modulation in all three examples, either centered or following movement onset. Note that while there is power at higher frequencies, almost all of the task modulating spectral power and coherence are in the theta band.

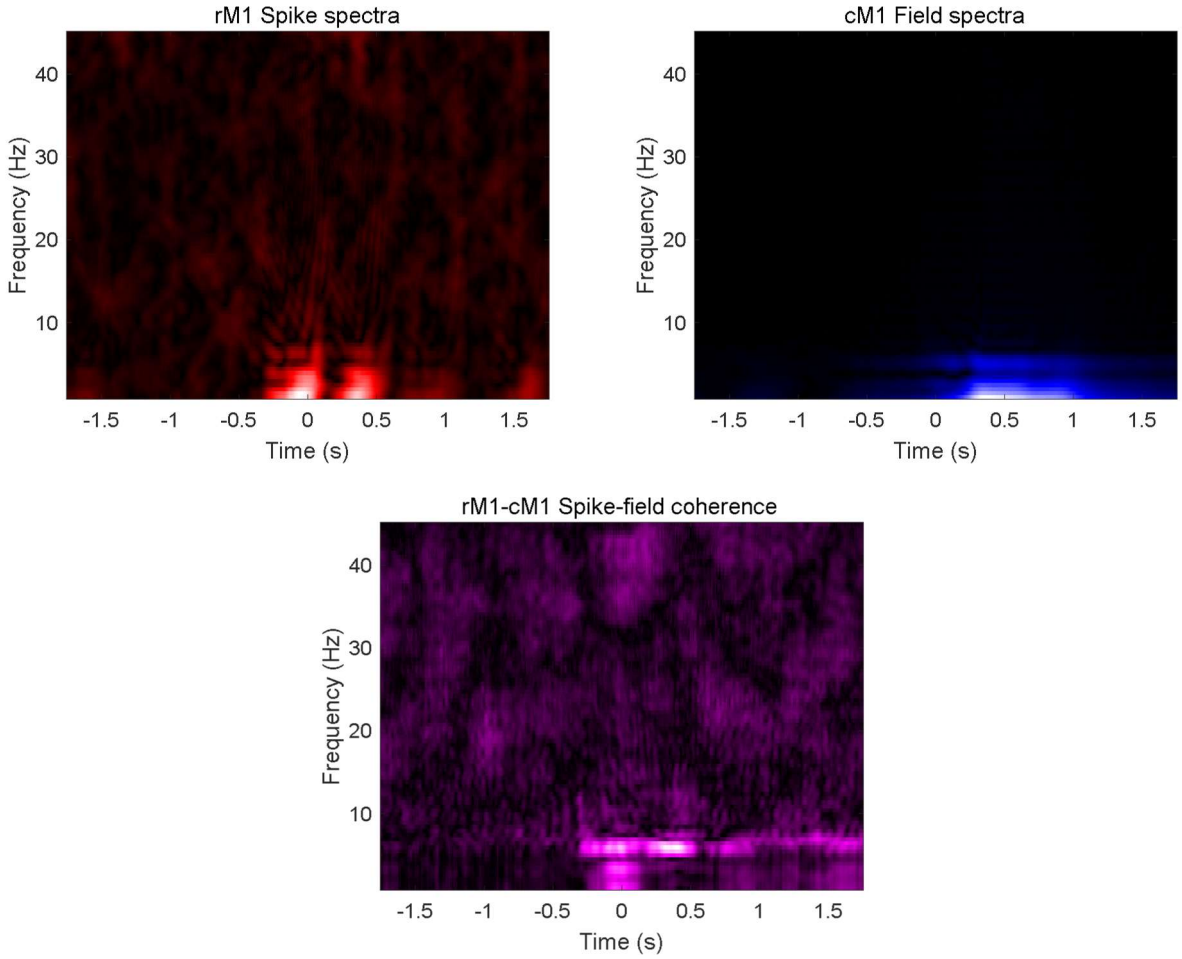

Figure 23 - Example Rostral M1 Neuronal Spectra, Caudal M1 Field Spectra, and rM1-cM1 Spike-Field Coherence for the Grasp Task.
The red plot shows the spectral power for an individual neuron in rostral M1; the blue plot shows the spectral power for a single local field potential signal in caudal M1. The purple plot shows the spike-field coherence between the examples shown in the red and the blue plots. Data are centered on movement onset. Frequencies range from 0.5 – 45 Hz.

Spike-Field Coherence

Time-varying coherence was calculated between every task-modulating neuron and LFP channel. Although not every such pair exhibits significant coherence, a majority do. For the grasp task, 60.37% of rM1-cM1 spike-field coherence pairs are significant, and 67.05% of the cM1-rM1 spike-field coherence pairs are significant. For the reach task, 92.04% of the rM1-cM1 spike-field coherence pairs are significant, and 91.36% of the cM1-rM1 spike-field coherence pairs are significant. Non-significant spike-field pairs are not included in the following results.

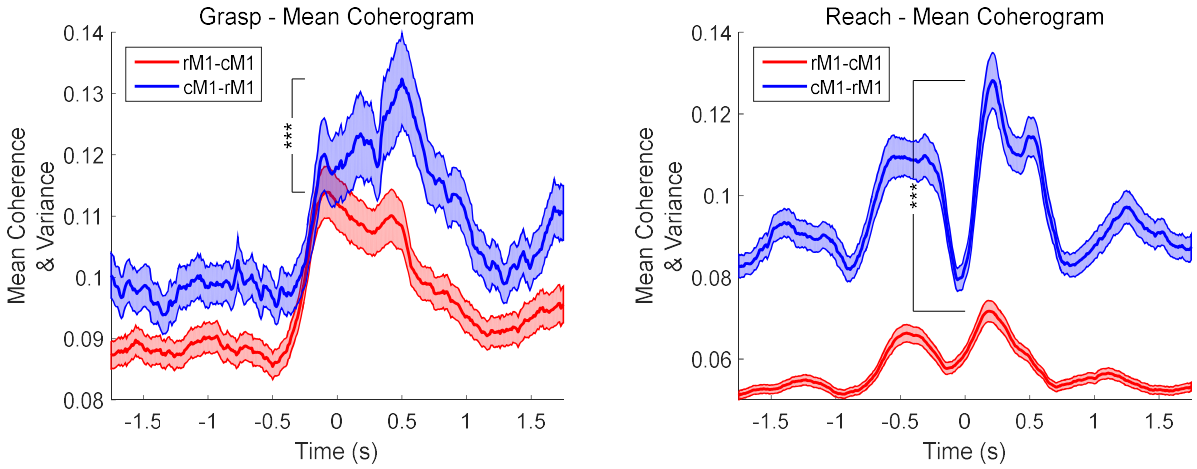

Figure 24 - Mean Coherograms.
Left = Grasp; right = Reach. Red = rM1-cM1 spike-field coherence; blue = cM1-rM1 spike-field coherence. Solid lines indicate means; shaded areas indicate variance. One asterisk indicates a p-value between 0.05 and 0.01; two, between 0.01 and 0.001; three, below 0.001. Note that the lower bound on the y-axes are different in each figure.

The mean coherence and variance for each area pair are shown in Figure 24. For the grasp task, the cM1-rM1 coherence is stronger and has a higher peak (p-value < 0.001). The magnitude of the peak cM1-rM1 coherence in the reach task is also higher than the rM1-cM1 coherence (p-value < 0.001).

The distributions of the peak coherence values are shown in Figure 25. The mean peak coherence is higher in the cM1-rM1 spike-field coherence in both the grasp (see above for p-values) and reach tasks.

To assess timing differences in the spike-field coherence between cortical areas, a cross-

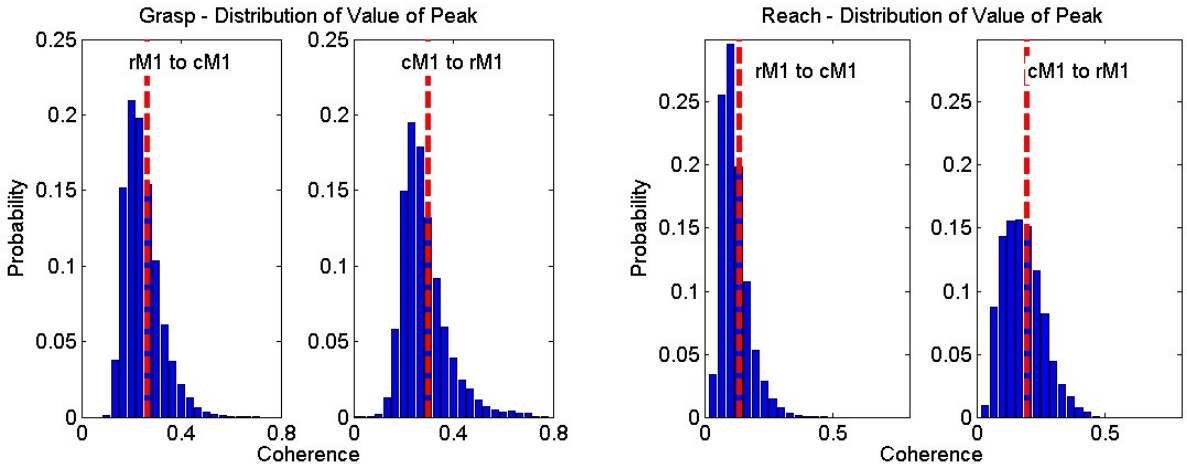

Figure 25 – Distributions of the Value of Peak Coherence.
As before, left shows grasp; right shows reach data. Red dashed line indicates the mean of each distribution. Note that the upper bound on the y-axis of the grasp and the reach figures are different.

correlation analysis was used. The average cross correlations and distributions of the time of the peak cross-correlations are shown in Figure 26. In both tasks, there is a strong peak before time lag 0 s. Accordingly, the average time of the peak is negative, indicating that the rM1-cM1 spike-field coherence led the cM1-rM1 coherence. Note that the time sensitivity is limited to 10 ms, the amount the moving windows (500 ms) were stepped.

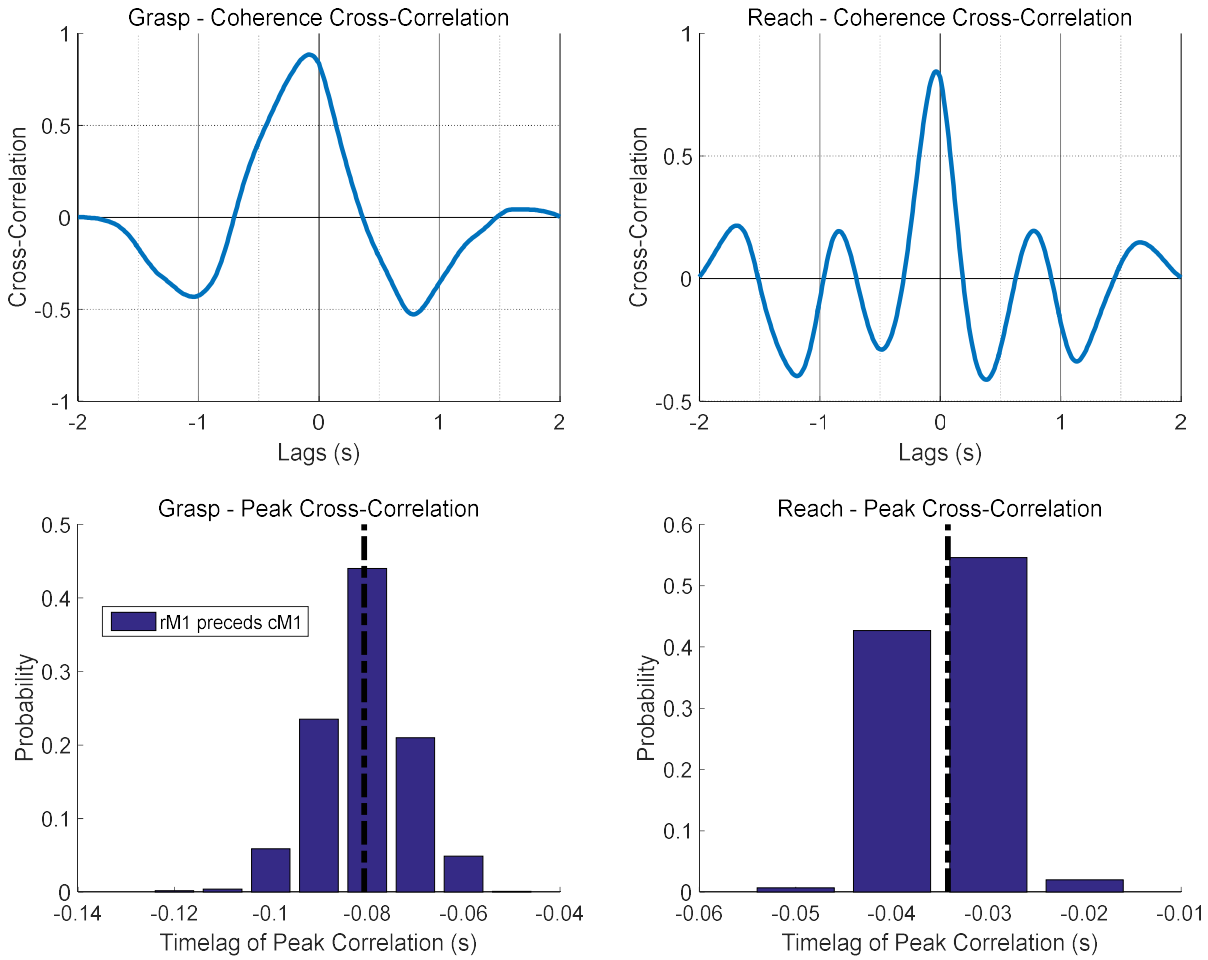

Figure 26 – Average Cross-Correlations and Distributions of Time of Peak Cross-Correlations. Left shows grasp; right shows reach. Top shows the average cross-correlation of the two spike-field coherence signals. Bottom shows the distributions of the time of the peak cross-correlation based on a boot strapping procedure. The black dashed lines indicate the mean of each distribution. Note that the upper bounds of the left and right distribution figures are different.

Comparisons of Firing Rates and Coherence

For these comparisons, the firing rates were recalculated to match the coherence analyses and to reduce the effects of bin sizes: rather than the 10 ms bins used for single unit analyses, here rates are calculated in sliding windows of 500 ms width, stepping by 10 milliseconds. Although the population firing rates in Figure 27 are similar to those shown previously in Figure 18, any differences may be attributed to the different parameters.

Figure 27, then, compares the population firing rates of the primary motor cortex subdivisions with the coherence analyses reported above. As before, in the grasp data the population firing rates of both areas begin to modulate prior to movement onset, and reach maximum firing rates after movement onset. Additionally, rM1 maximal firing precedes cM1. Similarly, the rM1-cM1 coherence peak precedes the cM1-rM1 coherence peak. However, both coherences increase faster than the firing rates do. Further, the rM1-cM1 spike-field coherence peaks before the rM1 spikes do, and the cM1-rM1 spike-field coherence peaks before the cM1 spikes do.

For the reach data, due to the continuous nature of the task, the modulating neurons exhibit continuously modulating firing. Additionally, the data are aligned on target acquisition, rather than movement onset. The rM1 population firing shows two peaks, surrounding target acquisition. The cM1 population firing shows one primary peak, between the two rM1 peaks, prior to target acquisition. As before, the population firing rates appear to be out of phase; that is to say that the cM1 firing rate troughs roughly line up with the rM1 firing rate peaks. Despite the population firing rates being out of phase, the population coherences seem to be in phase. The peaks and troughs roughly line up, with a trough shortly

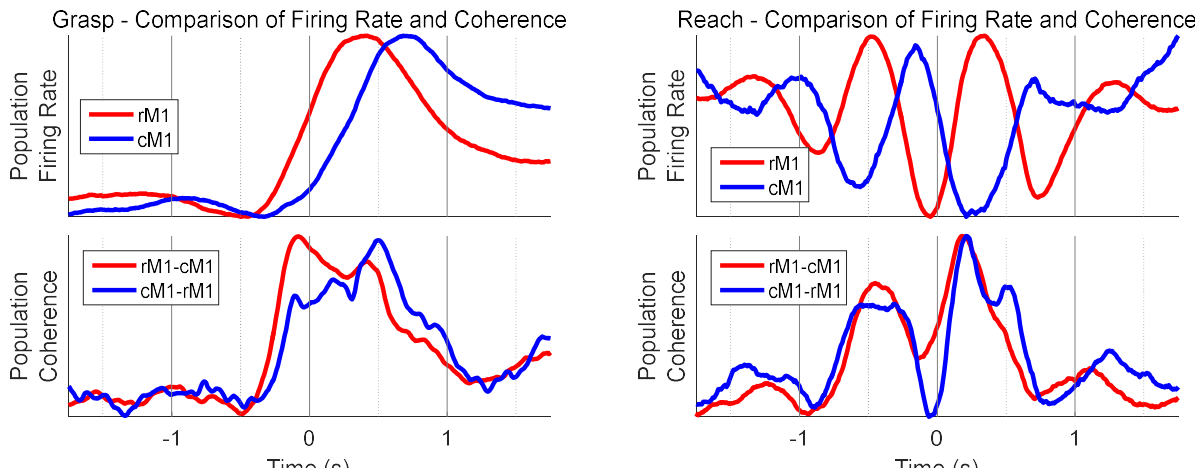

Figure 27 – Comparisons of Firing Rate and Coherence.

Left: Grasp data; Right: Reach data. Comparison of rM1 (red) and cM1 (blue) population firing rates (upper subplots) and rM1-cM1 (red) and cM1-rM1 (blue) population spike-field coherence (lower subplots). All traces have been individually normalized to visualize timing differences.

prior to target acquisition, and a peak shorty after. Further, both coherences are roughly aligned with the rM1 population firing.

Comparisons of Local Field Potential Spectra and Coherence

Figure 28 compares the average LFP power spectra for each subdivision of M1. As before, only LFP spectra and coherence in the theta frequency band are reported. The rM1-cM1 and cM1-rM1 spike-field coherences are plotted below for visual comparisons. Note that the data from both tasks, the spectra show clear task-modulation. However, the grasp cM1 spectra shows a wide valley with a trough after movement onset, and the other LFP signals show comparatively sharp peaks after movement onset/target acquisition. Additionally, although the population firing rates for the reach task show marked periodicity, the theta band of the LFP spectra does not.

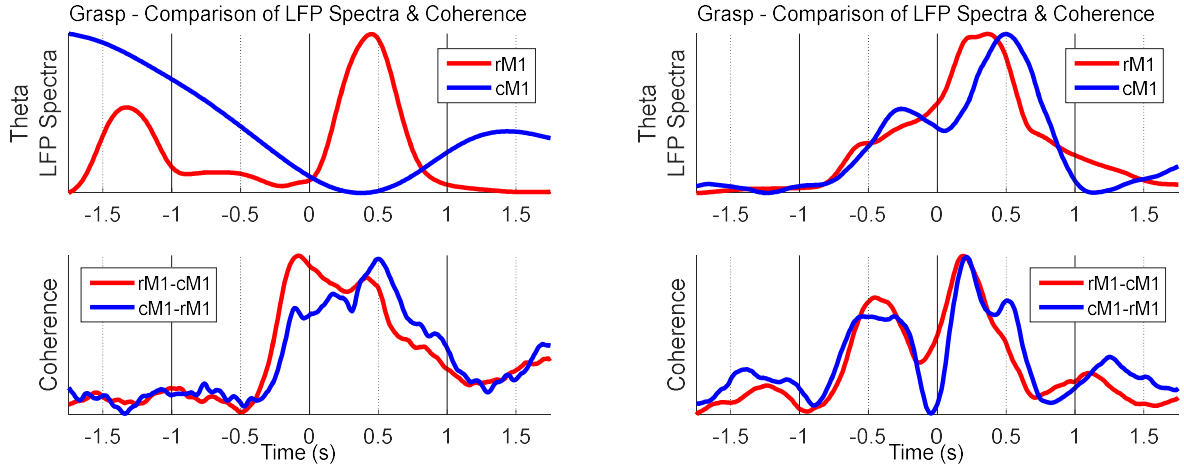

Figure 28 – Comparisons of Local Field Spectra and Coherence.
Left: Grasp data; Right: Reach data.
Top: Comparison of rM1 (red) and cM1 (blue) theta band (2-6 Hz) population local field spectra (upper subplots) and rM1-cM1 (red) and cM1-rM1 (blue) population spike-field coherence (lower subplots). Data have been scaled.

Divergence and Convergence of Coherence

To explore the functional structure of the coherent connections, I calculated divergence and convergence proportions. For both datasets, most neurons are highly divergent, in that they were coherent with proportionally many LFP signals (Figure 29). Further, the neurons in caudal M1 were

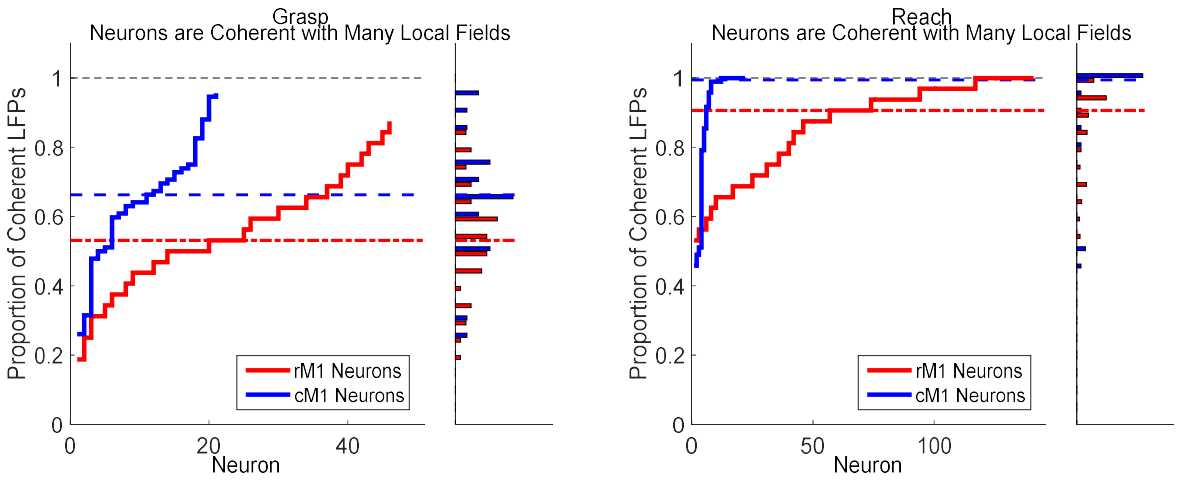

Figure 29 – Proportion of Local Fields Coherent with Each Neuron.
Left: Grasp data; Right: Reach data. Each value on the x-axis represents one neuron, and the y value indications the proportion of LFP channels with which it is coherent. Neurons are sorted in order of increasing divergence. Grasp p-value = 0.000. Reach p-value = 0.1301*10^-4.

significantly more divergent than neurons in rostral M1 (both *p*-values less than 0.001). That is to say, the populations of caudal M1 neurons were coherent with, on average, more LFP channels than the population of rostral M1 neurons.

Additionally, the LFPs receive highly divergent inputs: most LFP signal that showed significant coherence is coherent many neurons (Figure 30). Further, in the reach task, the LFP channels in caudal M1 receive significantly more convergent inputs than LFP channels in rostral M1 (*p*-value = 0). However, in the grasp task the means of the distributions are not different (*p*-value = 0.25).

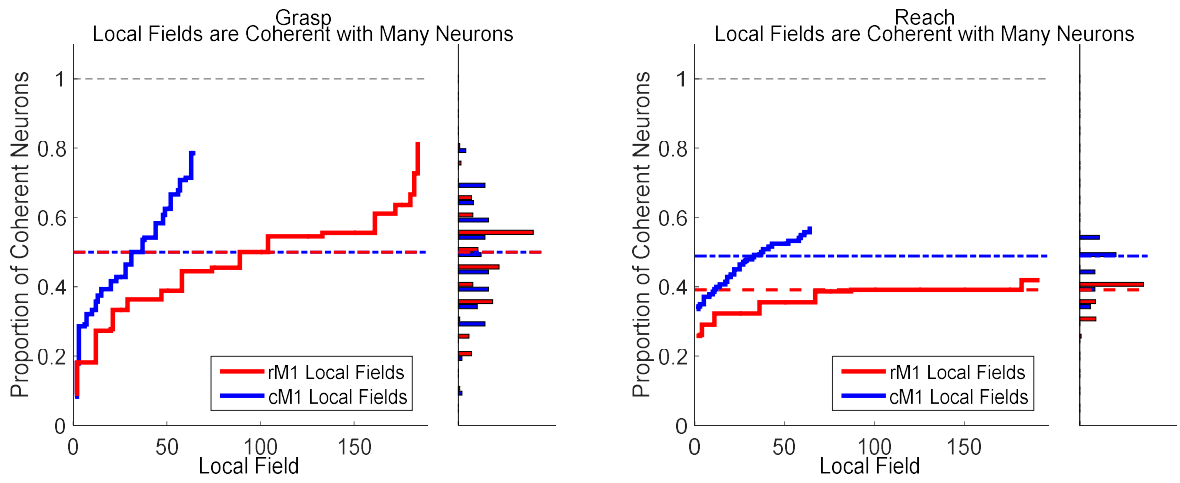

Figure 30 – Proportion of Neurons Coherent with Each Local Field.
Each value on the x-axis represents one local field, and the y value indications the proportion of neurons with which it is coherent. Fields are sorted in order of increasing convergence. Left: Grasp data; Right: Reach data. Grasp p-value = 0.2465. Reach p-value = 0.

Summary

A majority of neurons in both tasks and M1 subdivisions exhibit task modulation. At the population level, rM1 firing precedes cM1 firing in the grasp task, and rM1 firing is anti-phasic with cM1 firing in the reach task.

There is significant bidirectional spike-field coherence between rostral and caudal primary motor cortex. The coherences are strongly task modulated, and show interesting structure that is different for each subdivision.

Rostral M1-cM1 coherence precedes cM1-rM1 coherence in both tasks, although the latter shows stronger coherence. The time profiles of the population firing rates and the population LFPs do not align with the time profiles of the population spike-field coherences. Caudal M1 is more divergent than rostral M1, and tends to be more convergent as well.

Discussion

The central hypothesis of this chapter is that rostral motor cortex is higher in the motor cortical hierarchy than caudal motor cortex. I used coherence to explore this hierarchical organization, and found

evidence that supports the hypothesis. More specifically, I attempted to answer three questions: are these subdivisions coordinated; is the coordination dynamic and task modulated; and what is the structure of this coordination?

Figure 24 clearly addresses these questions. Neurons and local fields within these subdivisions consistently show bidirectional coherence, and the coherence is strongly task-modulated. Interestingly, this bidirectional coherence is not symmetric. That is to say that the rostral-caudal coherence leads the caudal-rostral coherence (Figure 26), and the caudal-rostral coherence is stronger (Figure 25). Further, the caudal-rostral coherence is more sustained throughout the movement. These findings suggest that rostral motor cortex is higher in the cortical hierarchy and that caudal motor cortex provides significant coherent connections to rostral during active movements.

However, it has been suggested in a paper dependent on models and simulations that spike-field coherence is largely dependent on firing rate [97], and thus not an appropriate statistical measure of spike-field synchrony. However, although I found that coherence was consistently stronger in the cM1-rM1 direction, significant differences in the firing rates did not exist (Figure 20 & Figure 19). Further, the time-course of the population firing rate and population coherence do not match (Figure 27). In both datasets, the peaks (and in the reach data, troughs) of the spiking do not align to the peaks of the coherence, even when spiking is recalculated in windows that match the coherence. The modulation of coherence also does not match the timing of the modulation of the population firing. Thus, experimental spike-field coherence may not be dependent on firing rate. Additionally, spike-field coherence is not largely dependent on field potentials, as demonstrated in Figure 28. Similar to population spiking, the time courses of population field potentials do not match the corresponding spike-field coherence in modulation or peak timing. Thus, spike-field coherence is not a simple result of spiking or local fields, but instead may represent the synchrony of neural populations in the cortical areas.

An additional concern is that the coherence between the two subdivisions of motor cortex are a result of common input from another neural source. However, as shown in Figure 15, each subdivision receives different thalamic inputs to each motor subdivision. Further, each has a different pattern of cortico-cortical connections, making it unlikely that a common neural source of input is driving the spike-field coherence.

Similarly, a concern is that the coherence between neural populations is instead indicative of the kinematics. However, in calculating significance, trials were separated into subgroups with similar kinematics (same object or same direction at peak velocity), and compared to "shuffled" versions of the data in which the spikes and fields came from different (but kinematically similar) trials. This shuffling minimally diminished the number of significant spike-field pairs, and minimally increased the magnitude of coherence.

A concern regarding the divergence results stems from the fact that local field potentials are highly consistent between nearby electrode channels. Therefore, a neuron that is coherent with one local field potential channel will likely be coherent with several channels, and one would thus expect most, if not all, neurons to be divergent, as is seen in the results. A similar logic holds true for convergence, though to a lesser extent: if individual neurons have similar representations in the frequency domain, then a field potential that is coherent with one neuron will likely be coherent with similar neurons. Thus, I expect all neurons to be somewhat divergent, and all local field potentials to be somewhat convergent. However, here I have compared the relative proportions, not absolute amounts, of convergence and divergence to each other. Accordingly, the statistically significant differences in the spike-field coherence divergence and convergence patterns are not solely the result of similar underlying neural activity.

Although there have been many studies exploring the role of neural oscillations in motor cortex, particularly rostral motor cortex, there have been no prior studies exploring interactions between

populations of neurons within rostral and caudal motor cortex to my knowledge. Indeed, modern neurophysiological studies investigating caudal motor cortex are rare. However, I believe there is more work to be done explore the role and interactions of caudal motor cortex in natural behaviors. For example, within the context of spike-field coherence, analysis of the relative phases of the coherences could prove insightful. Indeed, it may provide further insight to the directionality of coherence between the two neural populations. Further, additional data within each functional domain, reach or grasp, would provide beneficial confirmation to the findings presented in this dissertation.

IV. Investigating the Hierarchical Organization of Primary Motor and Somatosensory Cortices During Grasp and Tongue Behaviors

Introduction

Just as primary motor cortex is critical to the generation of movement, primary somatosensory cortex also plays a critical role during movement. This section explores the differences between single neurons and population of neurons simultaneously recorded in M1 and S1, in grasp and orofacial tasks, and the coordination between these primary cortical regions. As before, spike-field coherence is used to explore how the areas are coordinated, if the coordination is dynamic and task-modulated, and the structure of the coordination.

The previous section covered in detail the role of primary motor cortex in hand and arm use. Here, I expand the description to include the mouth and tongue, and provide a detailed description of primary somatosensory cortex, specifically area 2, in the use of these appendages. In this dissertation, the S1 arrays targeted Brodmann's area 2, but a few electrodes may have extended rostrally into area 1, or caudally into area 5. Nonetheless, without the ability to perform anatomical histology on the tissue, this dissertation assumes that all signals recorded from the arrays targeting S1 are indeed from area 2.

The coherence analyses found bidirectional, task-modulated coherence between M1 and S1. However, the coherence is not symmetrical: M1-S1 spike-field coherence peaks prior to S1-M1 coherence, and is higher in magnitude. Further, coherence from M1 is more divergent than coherence from S1. These results suggest that primary motor cortex has a strong influence on neural activity in the somatosensory cortex, perhaps providing an efference copy-like signal, and that somatosensory cortex may provide a feedback signal throughout movements.

Forelimb Movements in Somatosensory Cortex

Area 2, the subdivision of S1 that is focused on in this dissertation, contains a complete representation of the contralateral body that is similar in organization to its counterparts in S1 [98–100]. However, the somatotopic organization is not as precise as those in areas 3a, 3b, and 1, yet is less fractionated than in M1.

Neurons are strongly modulated by proprioceptive stimuli [101–104], with less modulation to cutaneous stimulation [98,105]. The hand and arm representations in area 2 are magnified compared to other representations (Figure 31) [26]. Indeed, the receptive fields themselves are also relatively large compared to other divisions of S1 [103,104]. Area 2 neurons respond to both passive and active movement [106,107], and modulate during grasping [108]. Neural activity in area 2 persists throughout movements, suggesting it is involved in monitoring and maintaining ongoing movements [109]. Additionally, activity of some neurons in area 2 often precedes self-generated movement [28]. Lesions involving somatosensory area 2 diminish accuracy of object shape, size and curvature determination [110,111], and impair active manual exploration [112]. Humans have an area 2 that seems similar in function to that of macaques [113].

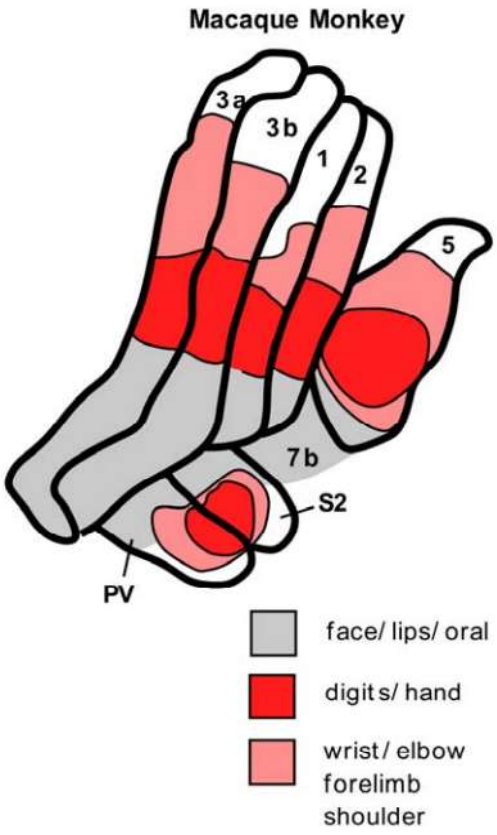

Figure 31 – Schematic of Somatotopic Organization of Area 2 Over Flattened Cortex.
Area 2 is located caudal to area 1, and rostral to area 5. Note that the hand and arm representations occupy a disproportionately large amount of cortical real estate. Krubitzer & Disbrow 2008 [26].

Primary somatosensory cortex has been shown to have oscillations similar to motor cortex [50,114,115]. This provides further evidence that M1 and S1 may be functionally linked, although it does not shed light on the hierarchical organization.

Area 2 is not only connected with other somatosensory cortical areas, but also M1 and posterior parietal cortex [19,23,116,117]. Thalamic projections to area 2 are primary from VPs and the anterior pulvinar [116,118]. Note that M1 receives different thalamic inputs than area 2 [119].

Thus, area 2 is primarily proprioceptive, involved in monitoring and maintaining movements, and monosynaptically interconnected with M1.

Orofacial Movements in Somatomotor Cortex

As well as the hand and arm, the primary motor cortex has been implicated in the complex control of tongue and jaw movements [120]. Indeed, neural activity within the face representation in motor cortex has been found to be very similar to that of hand and arm presentations. For example, motor cortex neurons modulate before and during orofacial movements [121]; tongue movements are

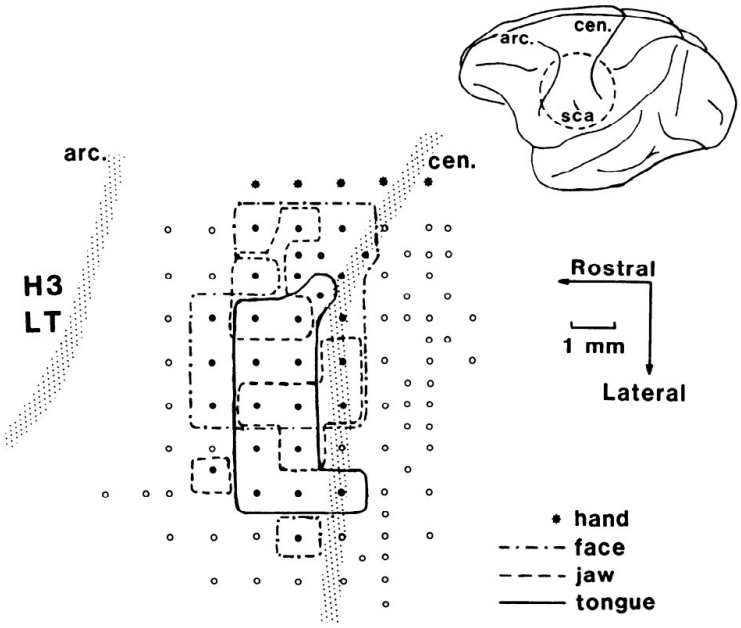

Figure 32 – Motor Map of Orofacial Representations in Motor Cortex
Dots indicate electrode penetration locations. Filled dots elicited movement; empty dots did not. Asterisks indicate stimulation locations that elicited hand movement. Solid, dashed, and dotted lines outline electrode locations that elicited tongue, jaw, and face movements, respectively. Note that the areas that elicited orofacial movements are fragmented and overlapping. Huang et al, 1989 [126].

highly represented in face area of motor cortex [122,123] (Figure 32); and tongue movements are overlapped with other movements in face area of motor cortex [122] (Figure 32). Further, neurons in primary motor cortex face area are directionally selective for tongue movements [124,125], and some motor cortex neurons fire stronger for more forceful orofacial movements [121], indicating force tuning.

Primary motor cortex receives orofacial, as well as forelimb, somatosensory inputs [126,127]. Some studies have shown that tongue representations in motor cortex receive predominantly cutaneous inputs, not proprioceptive [122], but these studies targeted area 2 less than areas 3b and 1.

Additionally, low amplitude stimulation in motor cortex induces tongue and face movements [122], and motor output and somatosensory input mappings within motor cortex are highly similar [122].

Orofacial M1 receives thalamic projections from the VL (Ventralis Lateralis) and VPL (Ventralis Posterior Lateralis) nuclei [128], similar to the forelimb representations. Cortico-cortical connections for orofacial M1 are also similar to the forelimb representations: orofacial M1 receives intracortical projections from the premotor areas include PMv, and somatosensory areas including primary somatosensory cortex and posterior parietal cortex [128].

Thus, principles established for the forelimb representation in motor cortex hold true for the orofacial representation. Additionally, somatosensory cortex is involved in orofacial movements, and the orofacial representation is largely similar to that of the forelimb.

Orofacial somatosensory cortex has a map of the body that is predominantly contralateral [129]. The face representation in S1 is more organized than in M1 [126] (Figure 33), and some neurons exhibit directional preference for movements [125,130], yet directional preferences are overlapped and fractionated [130]. Some neurons modulate prior to movement [129], and intracortical microstimulation in the face representation of S1 can induce movement [127] (Figure 33). Further, orofacial representations in M1 and S1 are densely monosynaptically interconnected [128].

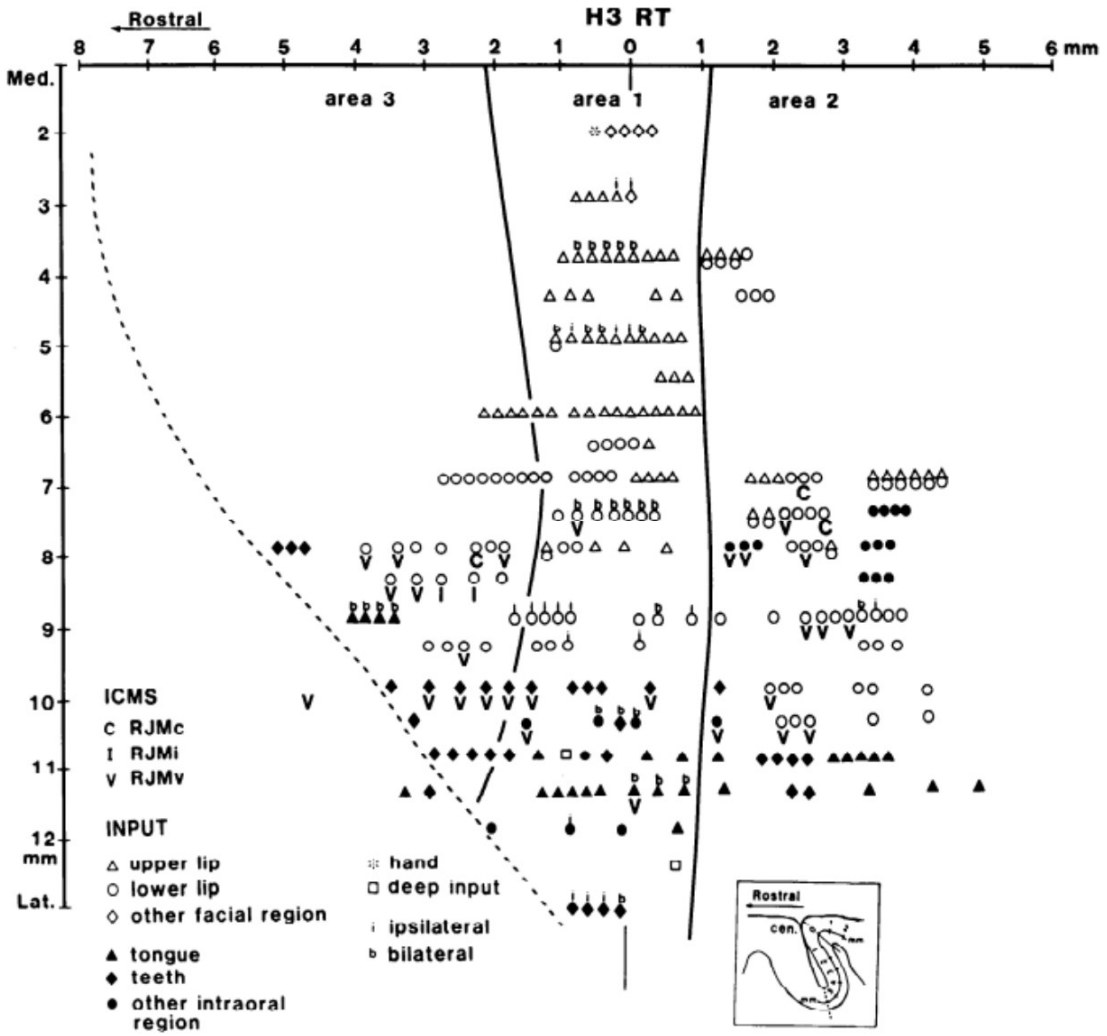

Figure 33 – Map of Orofacial Representation in Somatosensory Cortex
Map of somatosensory cortex and electrode locations from somatosensory mapping and ICMS. Note that the area 2 representation, at right, is relatively organized compared to the motor map in the previous figure. Huang et al 1989 [127].

Interactions Between S1 & M1

As area 2 is active throughout movements, it has been suggested that it may be the source of a motor error signal regarding active movements [131]. Indeed, a recent study by Menzer and colleagues found strong coherent connections between ensembles of neurons in areas 2 and 5 and LFPs in M1 in the 1-10 Hz frequency band [50]. Further, they found that this S1-M1 spike-field coherence typically modulated around movement onset, and peaked later. Interestingly, they found stronger coherence for

neural populations with similar direction preference than those with opposite preference. Other studies have also found weak coherence between S1 and M1 in the beta range during a finger flexion task [115]. Together, these results suggest that S1-M1 coherence contributes information about the ongoing movement to motor cortex, possibly as a sensory feedback signal.

Hierarchy

Primary motor and somatosensory cortices, despite their complementary functions, are less intuitive to place within a cortical hierarchy. Laminar connections, however, provide some insight: S1 projects strongly onto layer 3 of motor cortex, in an ascending pattern, and M1 projections to S1 tend to avoid middle layer 4 [15,23,24]. These patterns of connections imply that M1 is higher-order than S1.

Other research findings agree with this hierarchical structure. For example, as between PMv and M1, the motor representation in M1 is more complex than in S1 for both forelimb and orofacial representations [25,26,126]. Whereas somatosensory mappings are highly organized and structured, motor maps are highly fractionated and spread more diffusely across motor cortex. Further, task-modulated neural activity in M1 usually precedes S1, although S1 neurons often fire before movement onset [27,28,132]. These studies support the argument that, as M1 may be placed in somatosensory hierarchies [1,2], S1 may be placed in a motor cortex hierarchy.

Accordingly, several predictions may be made regarding activity between M1 and S1. First, I expect M1 firing to precede that in S1 in simultaneously recorded data. Further, M1-S1 will lead S1-M1 coherence.

Results

Single Unit Analyses

The following results are from analyses performed on single units in M1 and S1, from the grasp and tongue tasks. Note that the M1 units from the grasp monkey are the same as from rostral M1 analyses reported earlier. As before, data are based on 4 recording sessions, using two recording sessions for each task/monkey pooled across both datasets. Because the two sessions were recorded less than a week apart, it is possible that the same neuron are present in both datasets, but treated as two distinct neurons in the analyses [96].

Firing Rate Modulation

Neurons in both M1 and S1 were strongly task modulated (Figure 34). As before, for grasp Monkey B, in M1 88% (46/52) of neurons were task modulated; 60% (12/20) of S1 neurons were task modulated. In tongue Monkey Y, 85% (116/136) of M1 neurons task modulated; 76% (122/161) of S1 neurons task modulated.

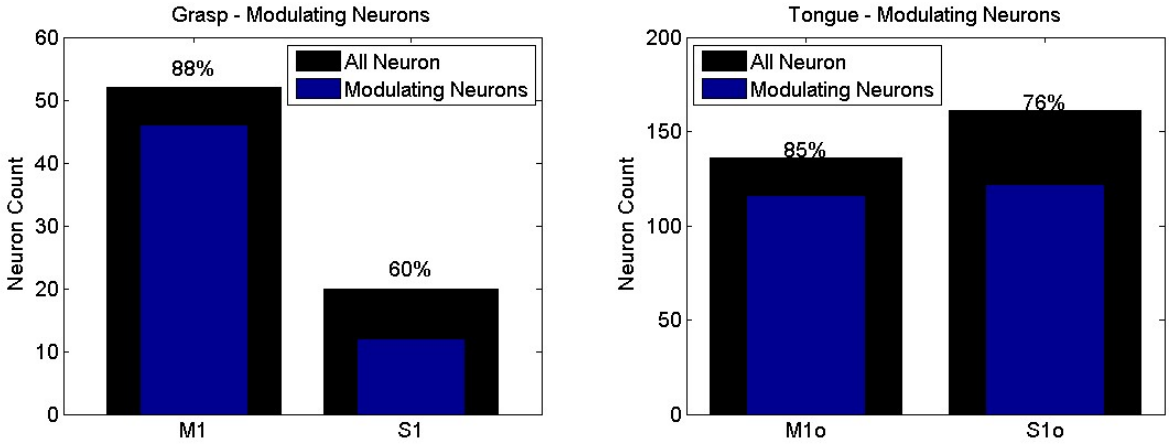

Figure 34 – Task Modulating Neurons.
Bar plots show the total number of neurons recorded in each area (black) and the subset of task modulating neurons (blue inset). Left: Grasp data; right: tongue data.

Figure 35 clearly shows this task modulation. The heat maps show trial-averaged firing rates for every task modulating neuron in both M1 and S1. Each row represents an individual neuron, and is normalized to between zero (black) and one (white). The first second, from -2 to -1 is considered the baseline period for modulation. Note that for the grasp task, most neurons modulate within one second of movement onset and then reach a steady rate for the duration of the trial. For the tongue task, most neurons modulate within one second of force onset, yet continue to modulate, as with the force profiles.

The bottom subplots of Figure 35 show the population-averaged normalized firing rates for M1 (red) and S1 (green). For the grasp data, the M1 popuplation firing rate modulates and peaks prior to S1

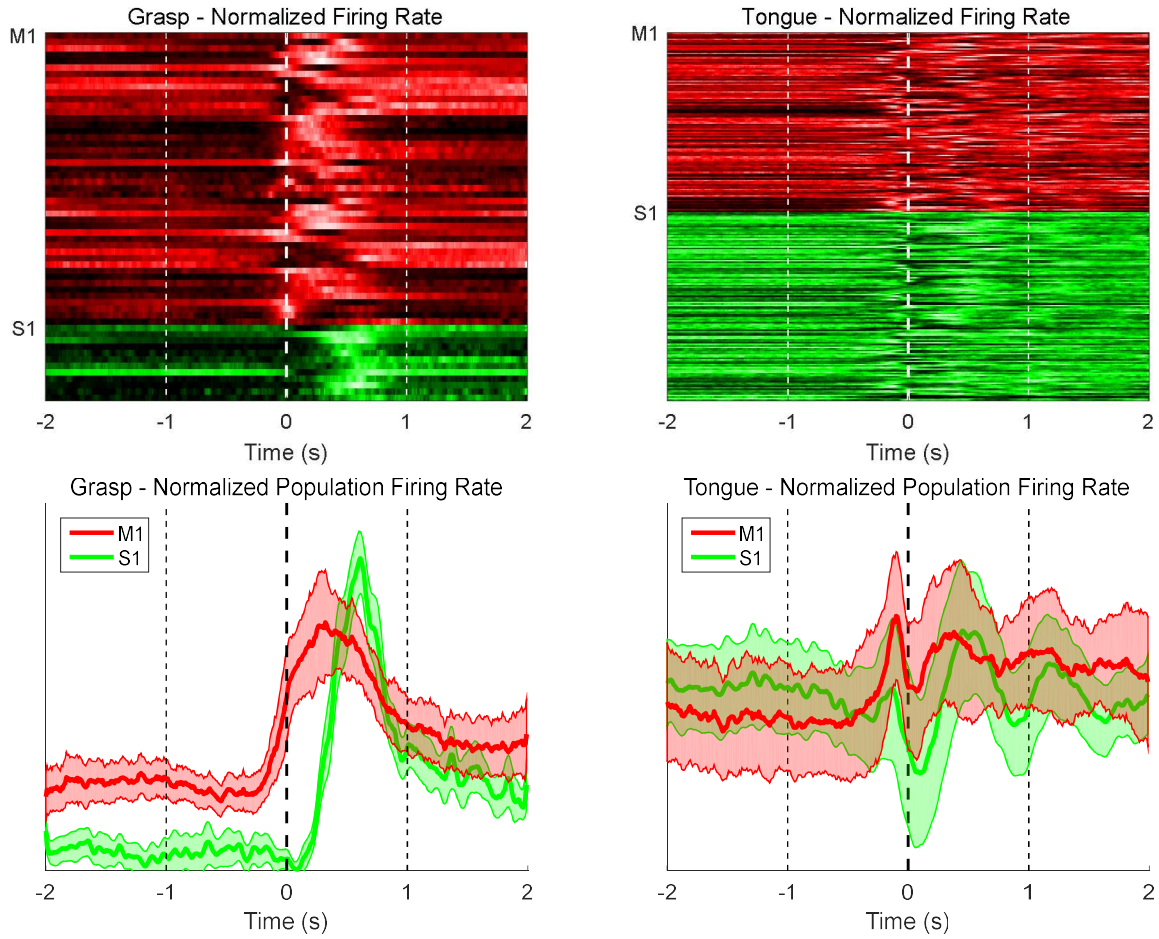

Figure 35 – Normalized and Population Firing Rates.
Left: Grasp data; right: tongue data. Top of each figure shows the normalized firing rate of each neuron, separated into cortical areas M1 and S1. Bottom of each figure shows the population normalized firing rate for each cortical area. M1 = red; S1 = green.

population firing rate, and both populations show ongoing increased firing rate. For the tongue data, M1 population firing rate also modulates and peaks prior to force onset, and then shows ongoing modulation. The S1 population firing rate modulates prior to movement onset, but shows a trough just after movement onset, and then shows sustained modulation.

Firing Rate Comparisons

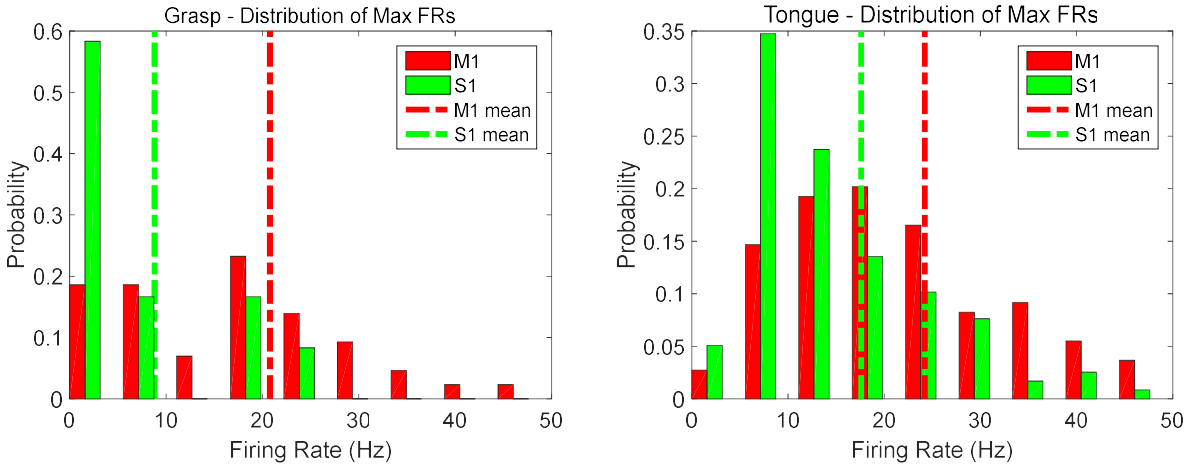

Figure 36 – Distribution of Maximum Firing Rates.
Means of the distributions for M1 and S1 are significantly different for both tasks. Left: grasp task; right: tongue task. Data plotted as probability of observed maximum firing rate. Vertical lines indicate the means of each distribution.

This subsection compares maximum and mean firing rates of single unit spiking in M1 and S1 for both the grasp and the tongue tasks. Figure 36 displays the distribution of maximum firing rates for each cortical area and task. The distribution of maximum firing rates is higher in M1 than S1 in both the grasp (p-value = 0.021) and tongue (p-value = 0.0002) tasks.

Figure 37 shows the distributions of mean firing rates across the 4 second window for each cortical area and task. Again, the mean firing rate in M1 is higher than in S1 for both the grasp (p-value = 0.028) and tongue (p-value = 0.0012) tasks.

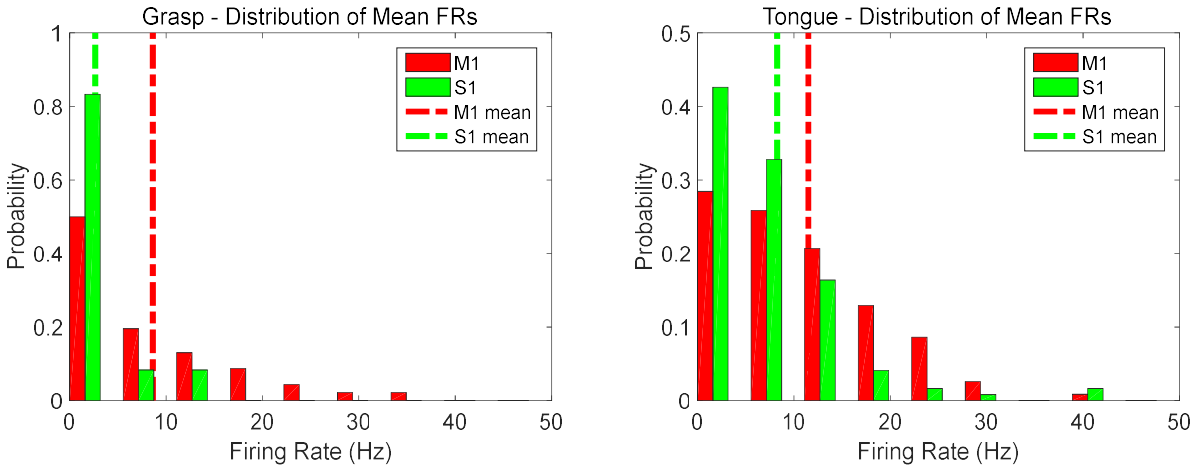

Figure 37 – Distribution of Mean Firing Rates.
Left = grasp; right = tongue. Red indicates rM1 firing rates; blue, cM1. Data plotted as probability of observed mean firing rate.

Cross-Correlation of Firing Rates

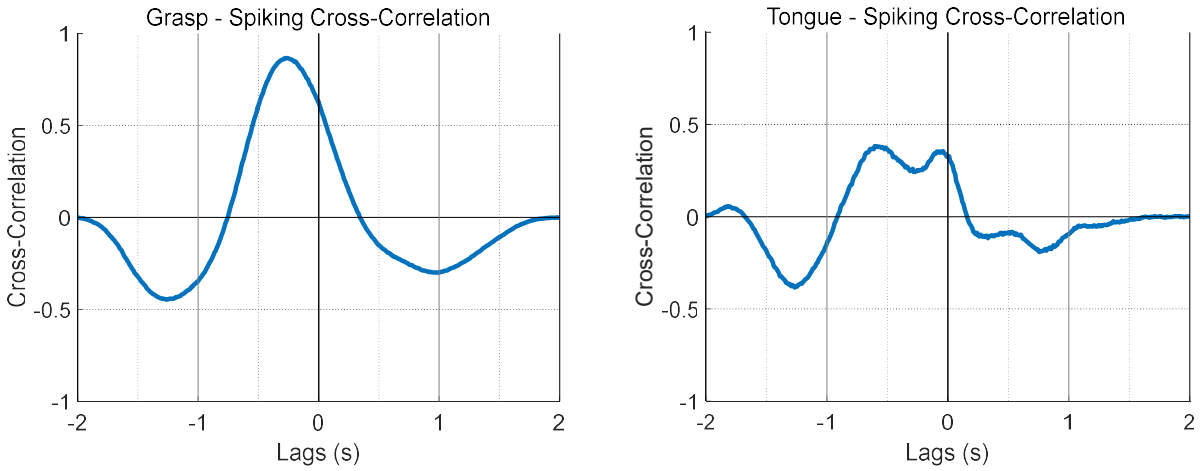

Figure 38 – Spiking Cross-Correlations.
Left: grasp data; right: tongue data. Blue traces indicate the mean cross-correlation between the populations of normalized firing rates in M1 and S1.

The cross-correlations shown in Figure 38 compare the timing of the population firing rates. The boot-strapped distributions of the time of peak correlation for each task, and the 95% confidence intervals, are shown in Figure 39. The mean and 95% confidence interval of the grasp distribution are -270 ms and -241 to -298 ms, respectively. The mean and 95% confidence interval of the tongue distributions are -429 ms and 24 to -890 ms, respectively. In both tasks, the peak cross-correlation occurs

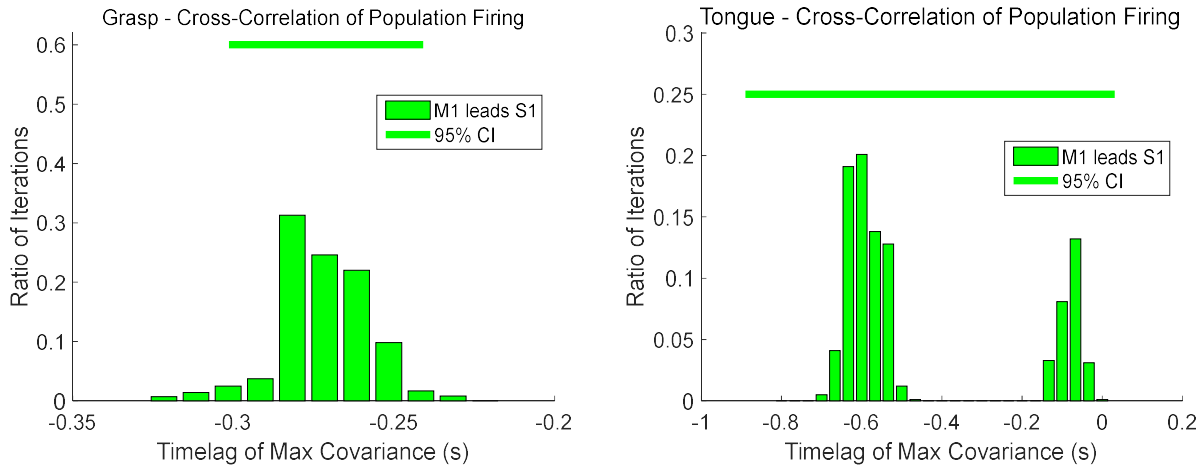

Figure 39 – Time of Maximum Cross-Correlations of Population Firing Rates Based on a Bootstrap Procedure.
Left: Grasp data; right: tongue. Horizontal bars represent 95% confidence interval for each distribution.

at negative lags, suggesting that the firing in M1 precedes that in S1. Thus, the population firing in M1 leads the population firing in S1 in every iteration of both the grasp and the tongue data.

Coherence Analyses

The following spectral analyses were performed on single units and LFP channels in M1 and S1. Coherence analyses are between single neurons in M1 and LFPs in S1, and single neurons in S1 and LFPs in M1. Additionally, population coherences are compared with population spiking and population LFPs from each cortical area. As before, the results here focus on the theta frequency band, 2-6 Hz.

Spectral Content

Figure 40 shows the spectral content of an example M1 neuron, S1 channel LFP, and the coherence between them from 0.5 to 45 Hz. The theta band (2-6 Hz) shows clear task modulation in all three examples, either centered or following movement onset. Note that while there is power at higher frequencies, almost all of the task modulating spectral power and coherence are in the theta band.

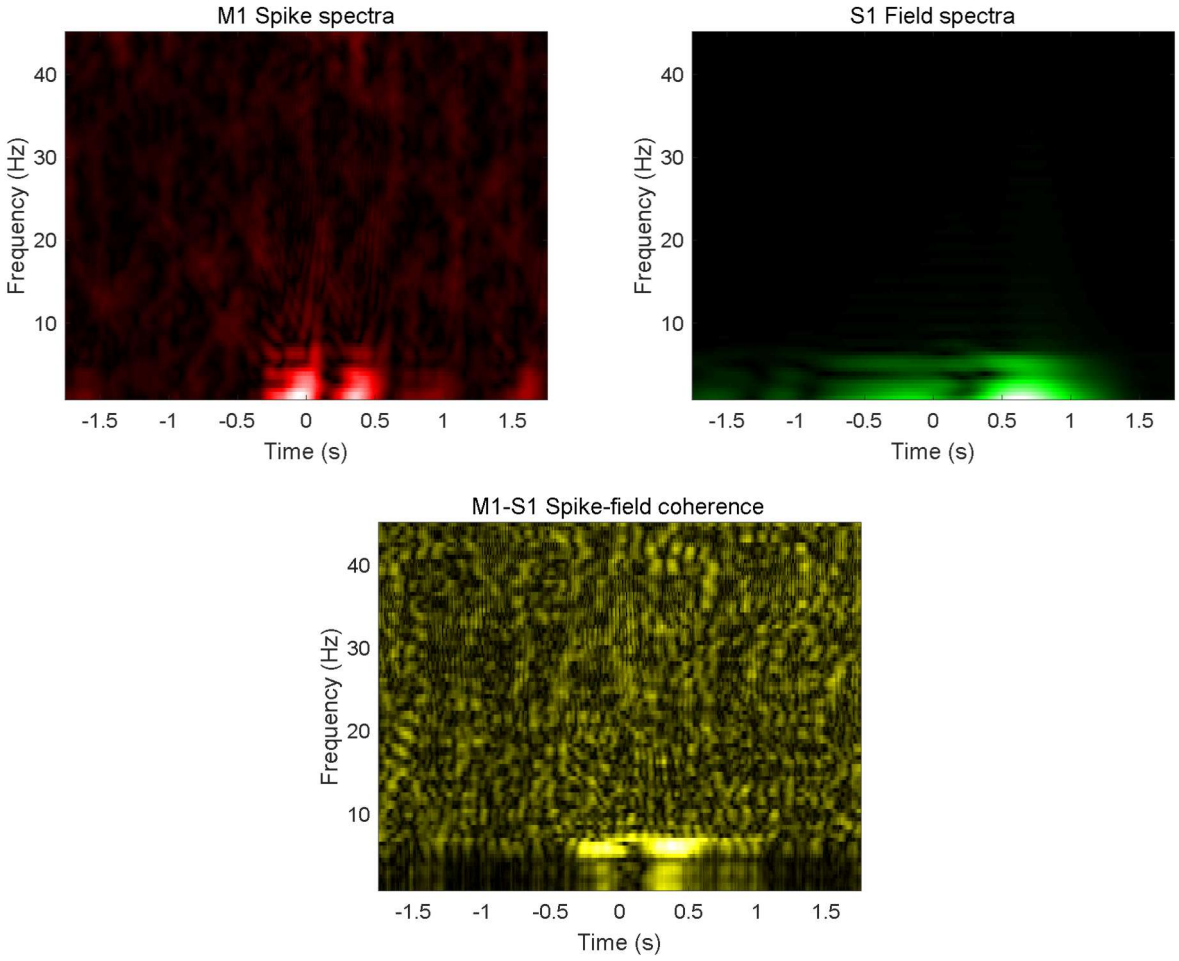

Figure 40 - Example M1 Neuronal Spectra, S1 Field Spectra, and M1-S1 Spike-Field Coherence.
Data are from the grasp task, and are centered on movement onset. The red plot shows the spectrogram for a single spiking unit in motor cortex; the green plot shows the spectrogram for a single local field in somatosensory cortex. The yellow plot shows the spike-field cohereogram between the two signals.

Spike-Field Coherence

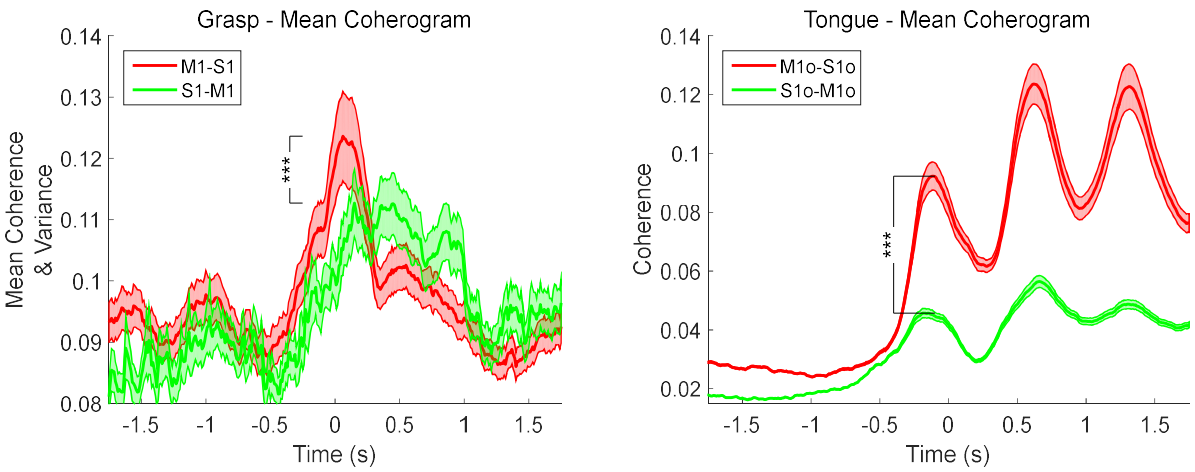

Figure 41 – Mean Coherograms.
Left = Grasp; right = tongue. M1-S1 spike-field coherence = red; S1-M1 coherence = green. Solid lines indicate means; dashed indicate variance. One asterisk indicates a p-value between 0,05 and 0,01; two, between 0.01 and 0.001; three, below 0.001. Note that the lower bound on the y-axes are different in each figure.

Coherence was calculated as a function of time for every neuron-field pair. 68.69 % of the M1-S1 spike-field coherence pairs and 54.59% of S1-M1 pairs for the grasp task exceeded 95% of the trial-shuffled coherence pairs. 86.22% of the M1-S1 spike-field coherence pairs and 87.24% of the S1-M1 coherence pairs for the tongue data exceeded 95% of the trial-shuffled coherence pairs. As with the rM1-

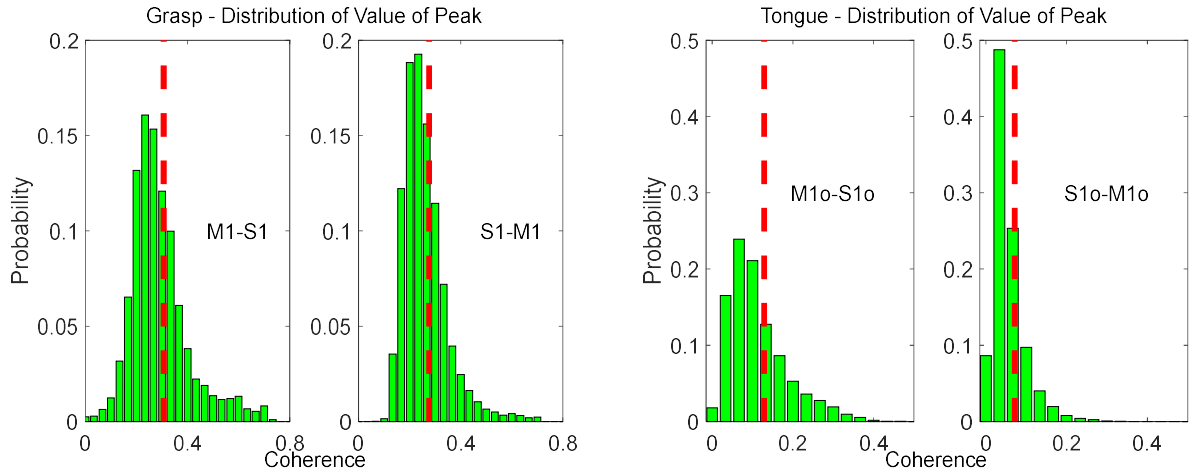

Figure 42 – Distributions of the Values of Peak Coherence.
Left = grasp; right = tongue. Red dashed lines indicate the means of each distribution. Note that the upper bounds of the grasp and the tongue data are different.

cM1 coherence, non-significant pairs (those that did not exceed 95% of the trial-shuffled coherence pairs) are not included in the following results.

Figure 41 shows the mean and variance for the spike-field coherence. In the grasp task, the M1-S1 spike-field coherence peaks is higher than the S1-M1 spike-field coherence (p-value < 0.001). In the tongue task, the M1-S1 coherence is stronger and has a higher peak (Figure 42; p-value < 0.001).

Figure 42 shows the distributions of the peak coherence values. For the grasp task, the mean for the M1-S1 peak value was 0.31; S1-M1 was 0.27. For the tongue task, the mean for the M1-S1 peak value

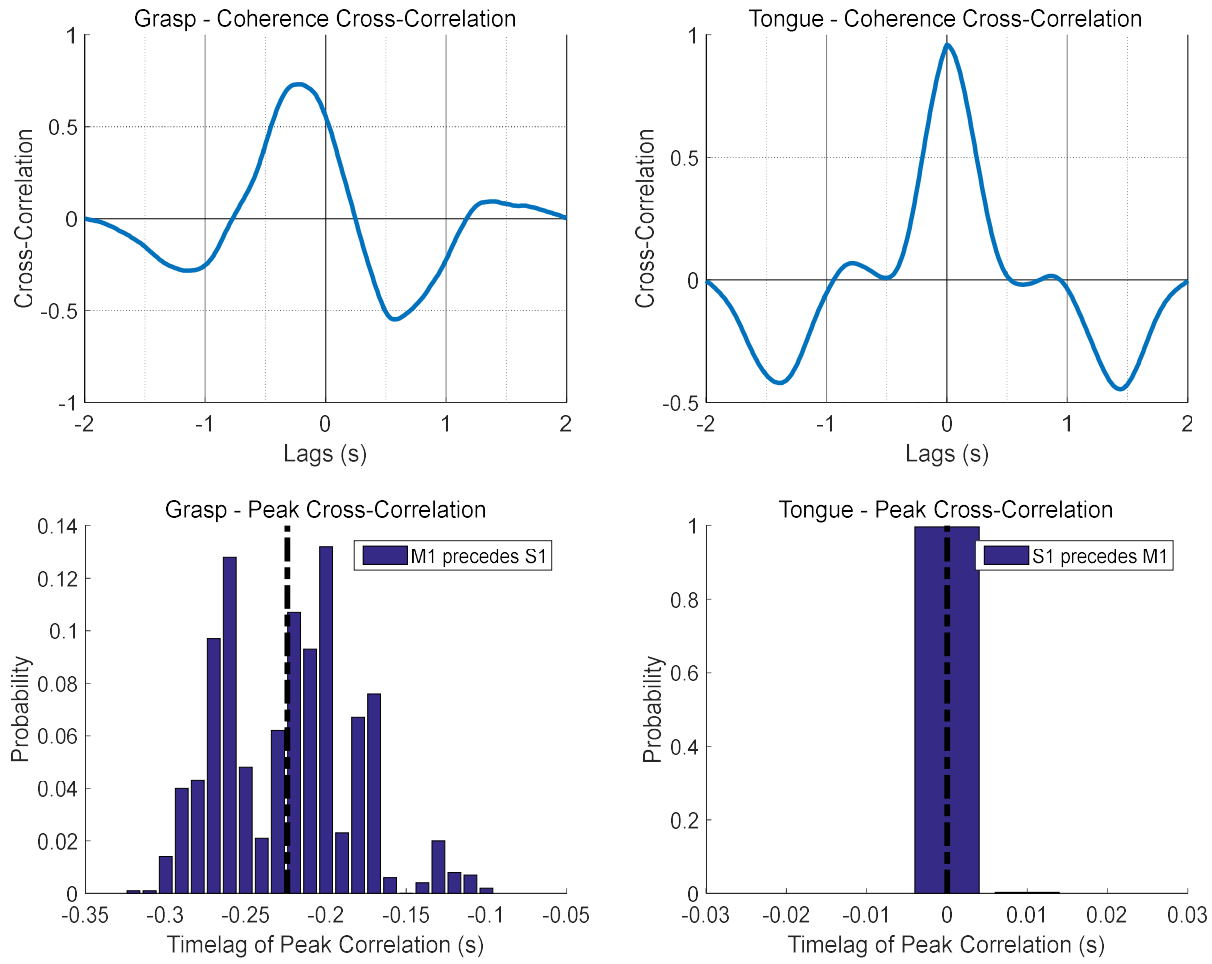

Figure 43 – Average Cross-Correlations and Distribution of Time of Peak Based on a Bootstrap Procedure.
Left plot shows grasp distributions; right shows tongue. Red dashed lines indicate the mean of the

was 0.17; for S1-M1 the mean is 0.09. Thus, for both tasks the M1-S1 spike-field coherence is higher than the S1-M1 coherence.

The average cross-correlations and distributions of the time of peak cross-correlations are shown in Figure 43. The grasp task shows a distribution of peaks centered around -200 ms, suggesting that the M1-S1 coherence leads the S1-M1 coherence. However, the tongue task has a slightly positive mean lag time, suggesting that the S1-M1 coherence slightly leads the M1-S1 coherence. Note that due to the constraints on the time-lag sensitivity, the average time of peak is only one time lag (10 ms).

Comparisons of Firing Rates and Coherences

Figure 44 shows the comparisons between the population firing rates and the population coherences. As noted previously, in the grasp task the M1 population firing rate begins to modulation prior to movement onset, and peaks after. The S1 population firing begins to modulate at movement onset, and peaks after the M1 population. Both populations show sustained firing after peaking. Both the M1-S1 and the S1-M1 spike-field coherences begin to modulate around the same time, similar to when

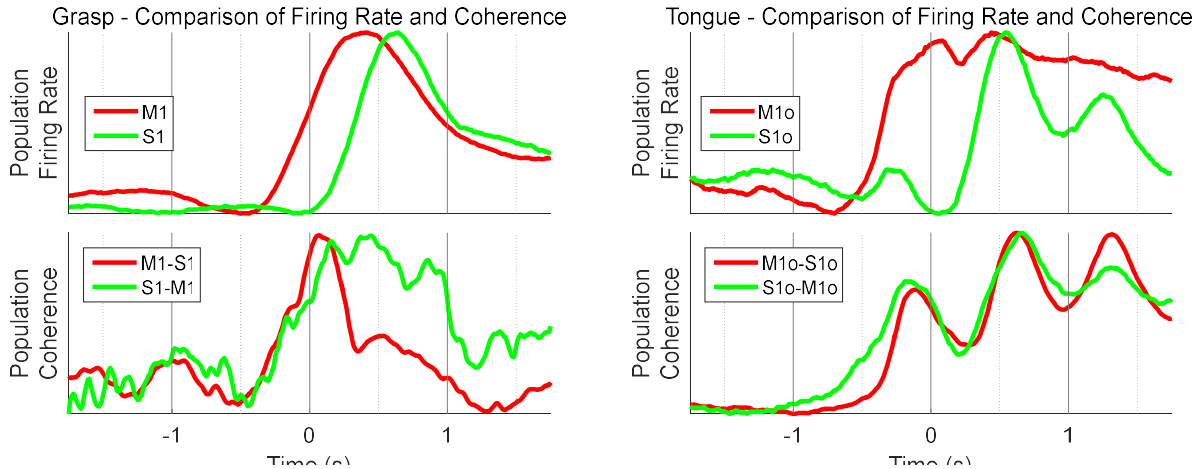

Figure 44 – Firing Rate & Coherence Correlations.
Left: Grasp data; Right: Tongue data.
Top: Comparison of M1 (red) and S1 (green) firing rates (upper subplots) and M1-S1 (red) and S1-M1 (green) spike-field coherences (lower subplots). All traces are individually normalized to visualize timing differences.

the M1 population firing rate begins to modulate. Both coherences peak soon after movement onset, but the S1-M1 coherence is more sustained after the peak coherence.

For the tongue task, both the M1 and S1 population firing rates show modulation well before force onset. The M1 population rate shows a peak near force onset, whereas the S1 population shows a trough near force onset, followed by a peak. Both the M1-S1 and S1-M1 spike-field coherences show modulation and small peaks prior to force onset, followed by ongoing modulation of troughs and peaks. Both coherences have similar profiles.

Comparisons of LFP Spectra and Coherence

Figure 45 compares the average LFP power spectra for M1 and S1. In both tasks, both cortical areas have population spectra that show clear modulation during the task window. The spectra for the grasp task begin to modulate near movement onset, and have large peaks at approximately 500 ms. The orofacial spectra modulate prior to force onset, and show strong decreases in power during force onset.

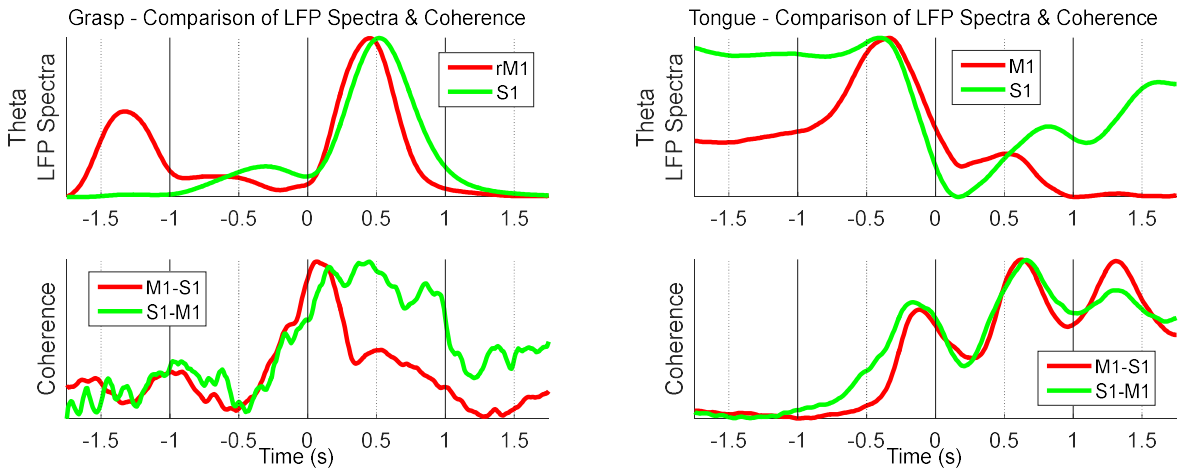

Figure 45 – LFP Spectra & Coherence Correlations.
Left: Grasp data; Right: Tongue data.
Top: Comparisons of M1 (red) and S1 (green) local field spectra (solid lines) and M1-S1 (dark gray) and S1-M1 (light gray) spike-field coherences (dashed lines). The y-axes apply only to the LFP spectra; the coherences have been normalized for visualization. Note that the y-axes for each subplot are on different orders of magnitudes.

Divergence and Convergence of Coherence

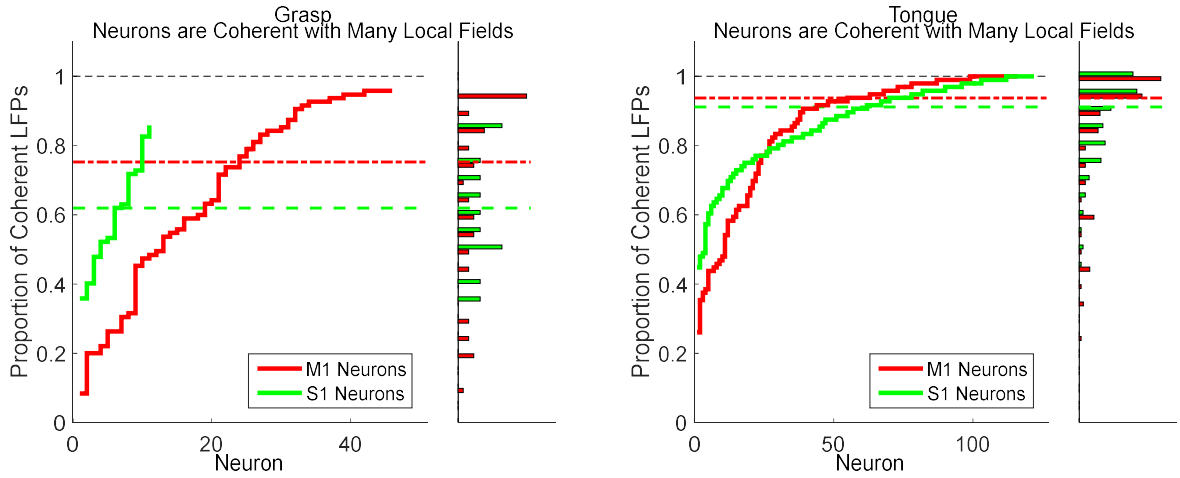

Figure 46 – Proportion of Local Fields Coherent with Each Neuron.
Each value on the x-axis represents one neuron, and the y value indications the proportion of local fields with which it is coherent. Neurons are sorted in order of increasing divergence. Left: Grasp data; Right: Reach data. Grasp p-value = 0.2465. Reach p-value = 0.

The functional structure of the coherent connections was explored by calculating the divergence and convergence proportions. For both the grasp and the tongue datasets, most neurons are highly divergent, coherent with proportionately many local fields (Figure 46). Further, M1 neurons are significantly more divergent than S1 neurons (grasp *p*-value <.001; tongue *p*-value 0.04). The population of M1 neurons were coherent with, on average, more S1 local fields than the population of S1 neurons with M1 fields.

Additionally, the local fields in each area receive highly convergent input. Most local fields showed significant coherence with many neurons (Figure 47). Further, in both tasks the local fields in S1

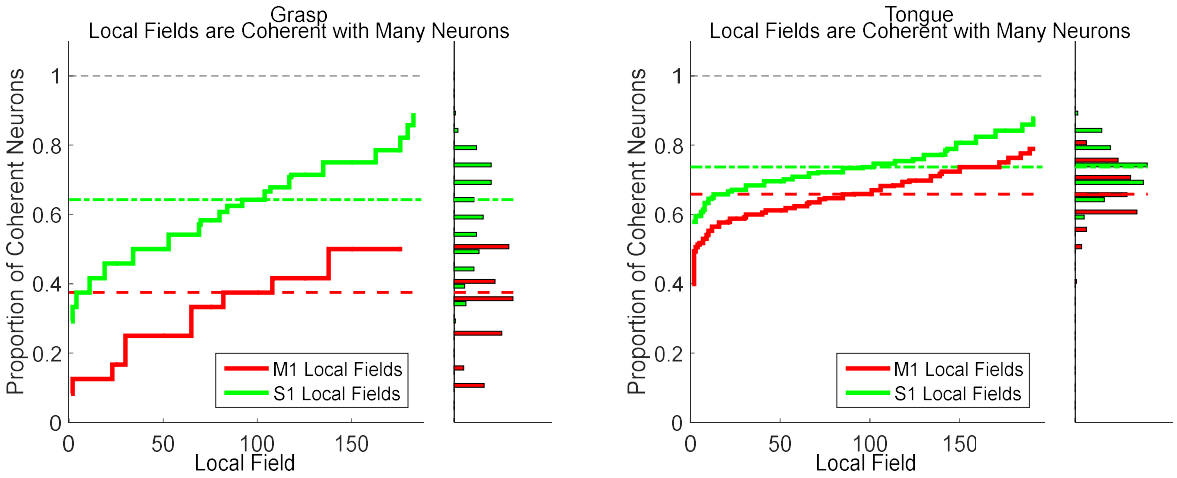

Figure 47 – Proportion of Neurons Coherent with Each Local Field.
Each value on the x-axis represents one local field, and the y value indications the proportion of neurons with which it is coherent. Fields are sorted in order of increasing convergence. Left: Grasp data; Right: Tongue data. Grasp p-value = 0. Tongue p-value = 0.

receive significantly more convergent input from M1 neurons than M1 local fields receive from S1 neurons (both p-values <0.001).

Summary

In both tasks, a majority of neurons in both M1 and S1 show task modulation. Population firing rates in M1 precede S1, but both show sustained firing after peaking.

There is significant bidirectional spike-field coherence between primary motor and somatosensory cortices. The coherences are strongly task modulated, and exhibit interesting structure that is different between each cortical area.

M1-S1 spike-field coherence is stronger than S1-M1 coherence in both tasks. Although M1-S1 coherence peaks prior to S1-M1 coherence in the grasp task, the converse is true in the tongue task. Although the rate-coherence correlations show peaks near zero lags, the spectra-coherence correlations show valleys for the tongue task. Nonetheless, as before, the differences in correlations tend to be more

driven by either the rates or the spectra than the spike-field coherences. M1 is more divergent than S1, yet S1 is more convergent than M1.

Discussion

The argument that primary motor cortex is hierarchically higher than primary somatosensory cortex is supported by the results shown here. Specifically, I attempted to address three questions: are these subdivisions coordinated; is the coordination task modulated; and what is the structure of this coordination?

The first two of these questions are addressed clearly in Figure 41. Neurons and local fields in these primary cortical areas consistently show bidirectional coherence, and this coherence is strongly task modulated. Further, the coherence is not symmetric. The M1-S1 spike-field coherence leads the S1-M1 spike-field coherence in the grasp task; in the orofacial task they seem to be synchronous (Figure 43). Further, the M1-S1 coherence is significantly stronger than the S1-M1 coherence (Figure 42). Additionally, in the grasp task the S1-M1 coherence is more sustained than the M1-S1 spike-field coherence, whereas in the tongue task they both continuously modulate. These findings suggest that motor cortex may be earlier in the cortical hierarchy, and that somatosensory cortex provides significant feedback to motor cortex during active movements.

As mentioned before, a theoretical paper suggested that spike-field coherence is largely dependent on firing rate [94], and thus not an appropriate statistical measure of spike-field synchrony. The results here may seem to confirm this hypothesis, as M1-S1 spike-field coherence is stronger, and M1 shows higher firing rates. However, this trend is not seen in the rostral-caudal motor cortex. Additionally, the time-course of the population firing rate and population coherence do not match (Figure 44). In both datasets, the peaks of the spiking do not align to the peaks of the coherence. The modulation of coherence also does not match the timing of the modulation of the population firing. Thus, experimental

spike-field coherence may not be dependent on firing rate. Additionally, spike-field coherence is not largely dependent on field potentials. As shown in Figure 45, population field potentials do not match the corresponding spike-field coherence in modulation or peak timing. Thus, spike-field coherence is not a simple result of spiking or local fields, but instead may represent the synchrony of neural populations in the cortical areas.

Another concern is that the coherence shown here is a result of common input from another neural source. However, these cortical areas receive different thalamic inputs to each motor subdivision, as well as having similar yet distinct cortical connections.

An additional concern is that the coherence between neural populations is instead caused by kinematics being represented in each region. However, in calculating significance for the grasp data, trials were separated into subgroups with similar kinematics (same object or same direction at peak velocity), and this significantly diminished neither the number of significant spike-field pairs, nor the magnitude of coherence. However, force data were so consistent between trials in the tongue force task that this separating the trials based on force profiles would not have had an effect.

The concern that coherence structure is necessarily convergent and divergent, as mentioned in the previous chapter, is avoided by comparing proportions of convergence and divergence, rather than absolute amounts.

Thus, the findings presented here regarding the spike-field coherence between primary motor and somatosensory cortices lend support to the hypothesis that M1 precedes and is superior to S1 in a somatomotor hierarchy. Nonetheless, these results are not conclusive, and would benefit from further research and additional data within each task and somatotopic representation. For example, the relative phase of the spike-field coherence could be explored to elucidate differences in the timing of the simultaneous coherence seen in the tongue task.

V. Conclusion

In this dissertation I have presented the results of analyses with the hopes of clarifying the relative positions of neural populations within cortical hierarchies in order to provide some insight as to how they functionally interact during naturalistic behaviors. Coherence may provide a mechanism by which neural populations dynamically weight the anatomical connections. Thus, by exploring spike-field coherence in this context, I have provided supporting evidence that rostral motor cortex sits hierarchically higher to, and receives dynamic feedback during movements from, caudal motor cortex. Additionally, I have provided evidence that primary motor cortex is positioned hierarchically above, and may be receiving dynamic feedback regarding limb state from, somatosensory cortex. However, more work is needed to confirm the evidence provided here.

Evolution of the Motor Cortex

The primary motor cortex evolved from primary somatosensory cortex approximately 100 million years ago, when placental mammals diverged from early mammals such as marsupials [133]. This is believed to be true based on motor representations in the neocortex in exemplar mammals. From species representative of the earliest mammals, for example Monodelphis opossum to Didelphis opossum, there is an increased representation of the motor map within somatosensory cortex. At the divergence between placental mammals, for example rodents, and marsupials, the motor cortex diverged into an adjacent cortical area that was mostly, but not completely distinct from somatosensory cortex. Thus, the existence of motor cortex, and of a distinct motor cortex, has increased with evolutionary time.

For example, in Monodelphis marsupials, an exemplar species of the earliest mammals, there is a complete sensory representation of the contralateral body surface contained within S1 [133]. This representation extends from the tail and hindlimb, through the forelimb and into the face and vibrissae. However, the motor representation is very limited. In a survey of ICMS in the neocortex, only facial

movements of the vibrissae and lower jaw were elicited. Additionally, these motor representations were completely contained within somatosensory cortex.

However, in Didelphis marsupials, the motor representation is expanded to include the entire contralateral body [133]. It isn't until placental mammals, for example, rodents, that there is a complete and mostly distinct primary motor cortex. This representation is completely distinct within primates. Further, the number of corticospinal projecting neurons has increased along with the divergence of motor cortex from somatosensory cortex and is believed to correlate with increased behavioral repertoire and manual dexterity.

Within motor cortex in primates, there has been another emergence of a new cortical area. A "new" motor cortex is believed to have evolved from the classical "old" motor cortex about 25 million years ago, when old world monkeys diverged from new world monkeys. There are several lines of evidence supporting the existence of these two distinct and complementary subdivisions of primary motor cortex in higher primates, including man. These distinctions, discussed at length in the Introduction to Chapter III, include different patterns of descending projections, different submodalities of sensory inputs, and complementary motor maps in each subdivision of primary motor cortex.

These evolutionary events provide an interesting timeline, where motor cortex evolved from somatosensory cortex, and then itself diverged into distinct cortical areas. This timeline provides an interesting context to interpret the results presented earlier. For example, the M1-S1 spike-field coherence is stronger than the S1-M1 spike-field coherence, and the cM1-rM1 coherence is stronger than the rM1-cM1 coherence. Thus, in all behavioral contexts presented here, the evolutionarily newer cortical area has stronger coherence with the older area than vice versa. Additionally, M1 neurons are more divergent in their coherent connections to S1 than S1 to M1, and cM1 neurons are more divergent to rM1

than rM1 to cM1. Thus, neurons in the evolutionarily newer areas have broader divergent coherent connections with their evolutionary roots.

The consistent findings that the newer cortical areas have stronger and more divergent coherence with older cortical areas, their evolutionary origins, suggests that evolution of novel cortical areas may have similar effects on the coordination between these areas. Although the results are only presented for three animals, the fact that they are so consistent between three different behavioral domains suggests that they may not have occurred by chance. Thus, there may be evolutionary constraints on the interactions between cortical areas that share common evolutionary origins.

Motor Control

The findings presented here also have implications for the role of active and dynamic interactions between the cortical areas during motor control. As seen in Figure 41, in particular in the grasp results, the M1-S1 coherence rises quickly and has a sharp peak before declining, whereas the S1-M1 coherence rises more slowly and is more sustained throughout the movement. This suggests that moto cortex may provide an initial efference copy-like signal to somatosensory cortex, alerting somatosensory cortex to the intended upcoming movement. Further, the slower and more sustained S1-M1 coherence may represent somatosensory feedback regarding the ongoing movement.

Likewise, Figure 24 may have interesting implications for motor control in the primary motor cortex. Rostral-caudal spike-field coherence shows an initial strong peak that leads the cM1-rM1 spike field coherence, suggesting that rostral motor cortex may provide an efference copy-like signal to cM1 regarding the initial, ballistic stage of a voluntary movement. Further, as seen in the cM1-rM1 coherence which has a peak later in the movement, cM1 may be involved in the online control and correction of movement after the ballistic stage.

Future Directions

There are several interesting directions to take this body of work, to expand its scope, and to further clarify its assertions. For example, it is possible that an analysis of the phase of the coherence, in combination with the magnitude, as presented herein, may provide a better basis for comparing the relative timings of the spike-field coherence between cortical areas. Additionally, exploring the relationship between tuning properties, such as preferred hand joint or movement direction, and the magnitude of coherence between spike-field pairs may provide further insight. For example, as mentioned previously, Menzer and colleagues [50] found that spike-field coherence is stronger between populations of neurons with similar directional tuning. Thus, it would be interesting to explore these relationships, particularly in the reach and grasp tasks in which joint selectivity and directional tuning may play a role. For the tongue task, it is possible that force tuning correlates with spike-field coherence magnitude.

Another route for further exploration would be to explore a more causal interaction between cortical areas, rather than relying on correlative analyses. Intracortical microstimulation is an obvious choice, and early attempts were made in Monkey At, but will be actively pursued soon in the grasping task as well.

Finally, I would like to expand these comparisons to other cortical areas, with the hope of assessing if the suggested evolutionary rules, that newer cortical areas show strong and divergent coherence with their evolutionary roots, hold true in other areas. If true, these rules may provide insight for how novel cortical areas dynamically interact with their evolutionary origins during natural behaviors.

Bibliography

1. Felleman DJ, Van Essen DC. Distributed Hierarchical Processing in the Primate Cerebral Cortex. Cereb. Cortex. 1991 Jan 1;1–47.
2. Shipp S. The importance of being agranular: a comparative account of visual and motor cortex. … Trans. R. Soc. …. 2005;
3. Hauk O, Johnsrude I, Pulvermüller F. Somatotopic representation of action words in human motor and premotor cortex. Neuron. 2004;
4. Caminiti R, Johnson P. Making arm movements within different parts of space: the premotor and motor cortical representation of a coordinate system for reaching to visual targets. J. …. 1991;
5. Kakei S, Hoffman DS, Strick PL. Sensorimotor transformations in cortical motor areas. Neurosci. Res. 2003 May;1–10.
6. Mushiake H, Inase M, Tanji J. Neuronal activity in the primate premotor, supplementary, and precentral motor cortex during visually guided and internally determined sequential movements. J Neurophysiol. 1991 Sep 1;705–18.
7. Soechting JF, Flanders M. Moving in three-dimensional space: frames of reference, vectors, and coordinate systems. Annu. Rev. Neurosci. Annual Reviews 4139 El Camino Way, P.O. Box 10139, Palo Alto, CA 94303-0139, USA; 1992 Jan 28;167–91.
8. Gallese V, Goldman A. Mirror neurons and the simulation theory of mind-reading. Trends Cogn. Sci. 1998;
9. Ferrari P, Gallese V. Mirror neurons responding to the observation of ingestive and communicative mouth actions in the monkey ventral premotor cortex. Eur. J. …. 2003;
10. Takada M, Tokuno H, Nambu A, Inase M. Corticostriatal projections from the somatic motor areas of the frontal cortex in the macaque monkey: segregation versus overlap of input zones from the primary motor cortex, the supplementary motor area, and the premotor cortex. Exp. Brain Res. 1998 Apr 27;114–28.
11. FULTON JF. A NOTE ON THE DEFINITION OF THE “MOTOR” AND “PREMOTOR” AREAS. Brain. 1935 Jun 1;311–6.
12. Maier M, Armand J, Kirkwood P. Differences in the corticospinal projection from primary motor cortex and supplementary motor area to macaque upper limb motoneurons: an anatomical and. Cereb. …. 2002;
13. Rathelot J, Strick P. Muscle representation in the macaque motor cortex: an anatomical perspective. Proc. Natl. …. 2006;
14. Fu QG, Flament D, Coltz JD, Ebner TJ. Temporal encoding of movement kinematics in the discharge of primate primary motor and premotor neurons. J Neurophysiol. 1995 Feb 1;836–54.
15. Friedman D, Murray E. Cortical connections of the somatosensory fields of the lateral sulcus of macaques: evidence for a corticolimbic pathway for touch. J. …. 1986;
16. Huntley GW, Jones EG. Relationship of intrinsic connections to forelimb movement representations in monkey motor cortex: a correlative anatomic and physiological study. J.

Neurophysiol. 1991;390–413.

17. Primrose D, Strick P. The organization of interconnections between the premotor areas in the primate frontal lobe and the arm area of primary motor cortex. Soc. Neurosci. Abstr. 1985;

18. Dancause N, Barbay S, Frost SB, Plautz EJ, Popescu M, Dixon PM, et al. Topographically divergent and convergent connectivity between premotor and primary motor cortex. Cereb. Cortex. 2006 Aug 1;1057–68.

19. Stepniewska I, Preuss TM, Kaas JH. Architectonics, somatotopic organization, and ipsilateral cortical connections of the primary motor area (M1) of owl monkeys. J. Comp. Neurol. 1993;238–71.

20. Rathelot J-A, Strick PL. Subdivisions of primary motor cortex based on cortico-motoneuronal cells. Proc. Natl. Acad. Sci. U. S. A. 2009 Jan 20;918–23.

21. Porter R, Lemon R. Corticospinal function and voluntary movement. 1993;

22. Kwan HC, MacKay WA, Murphy JT, Wong YC. Spatial organization of precentral cortex in awake primates. II. Motor outputs. J. Neurophysiol. 1978;1120–31.

23. Jones E. Intracortical connectivity of architectonic fields in the somatic sensory, motor and parietal cortex of monkeys. J. Comp. …. 1978;

24. Andersen R, Asanuma C. Corticocortical connections of anatomically and physiologically defined subdivisions within the inferior parietal lobule. J. …. 1990;

25. Park MC, Belhaj-Saïf A, Cheney PD. Properties of primary motor cortex output to forelimb muscles in rhesus macaques. J. Neurophysiol. 2004 Nov 1;2968–84.

26. Krubitzer L, Disbrow E. The evolution of parietal areas involved in hand use in primates. Somat. London Elsevier. 2008;

27. Soso MJ, Fetz EE. Responses of identified cells in postcentral cortex of awake monkeys during comparable active and passive joint movements. J. Neurophysiol. 1980 Apr 1;1090–110.

28. Nelson RJ. Activity of monkey primary somatosensory cortical neurons changes prior to active movement. Brain Res. 1987 Mar;402–7.

29. Bensmaia SJ, Denchev P V, Dammann JF, Craig JC, Hsiao SS. The representation of stimulus orientation in the early stages of somatosensory processing. J. Neurosci. 2008 Jan 16;776–86.

30. Georgopoulos A, Schwartz A, Kettner R. Neuronal population coding of movement direction. Science (80-.). American Association for the Advancement of Science; 1986 Sep 26;1416–9.

31. Hatsopoulos NG, Ojakangas CL, Paninski L, Donoghue JP. Information about movement direction obtained from synchronous activity of motor cortical neurons. Proc. Natl. Acad. Sci. 1998 Dec 22;15706–11.

32. Bokil H, Andrews P, Kulkarni JE, Mehta S, Mitra PP. Chronux: a platform for analyzing neural signals. J. Neurosci. Methods. 2010 Sep 30;146–51.

33. Mitzdorf U. Properties of the Evoked Potential Generators: Current Source-Density Analysis of Visually Evoked Potentials in the Cat Cortex. Int. J. Neurosci. Taylor & Francis; 1987 Jul 7;33–59.

34. Okun M, Naim A, Lampl I. The subthreshold relation between cortical local field potential and neuronal firing unveiled by intracellular recordings in awake rats. J. Neurosci. 2010 Mar 24;4440–8.

35. Xing D, Yeh C-I, Shapley RM. Spatial spread of the local field potential and its laminar variation in visual cortex. J. Neurosci. 2009 Sep 16;11540–9.

36. Hwang EJ, Andersen RA. The utility of multichannel local field potentials for brain-machine interfaces. J. Neural Eng. IOP Publishing; 2013 Aug 1;046005.

37. Buzsáki G, Draguhn A. Neuronal oscillations in cortical networks. Science. American Association for the Advancement of Science; 2004 Jun 25;1926–9.

38. Bansal AK, Truccolo W, Vargas-Irwin CE, Donoghue JP. Decoding 3D reach and grasp from hybrid signals in motor and premotor cortices: spikes, multiunit activity, and local field potentials. J. Neurophysiol. 2011 Dec 7;1337–55.

39. Donoghue JP, Sanes JN, Hatsopoulos NG, Gaal G. Neural Discharge and Local Field Potential Oscillations in Primate Motor Cortex During Voluntary Movements. J Neurophysiol. 1998 Jan 1;159–73.

40. Murthy VN, Fetz EE. Oscillatory activity in sensorimotor cortex of awake monkeys: synchronization of local field potentials and relation to behavior. J Neurophysiol. 1996 Dec 1;3949–67.

41. Donchin O, Gribova A, Steinberg O, Bergman H, de Oliveira C, Vaadia E. Local field potentials related to bimanual movements in the primary and supplementary motor cortices. Exp. Brain Res. 2001 Sep 1;46–55.

42. Gemba H, Hashimoto S, Sasaki K. Cortical field potentials preceding visually initiated hand movements in the monkey. Exp. Brain Res. 1981 May;

43. Rickert J, Oliveira SC de, Vaadia E, Aertsen A, Rotter S, Mehring C. Encoding of movement direction in different frequency ranges of motor cortical local field potentials. J. Neurosci. 2005 Sep 28;8815–24.

44. Mehring C, Rickert J, Vaadia E, Cardosa de Oliveira S, Aertsen A, Rotter S. Inference of hand movements from local field potentials in monkey motor cortex. Nat. Neurosci. 2003 Dec;1253–4.

45. Asher I, Stark E, Abeles M, Prut Y. Comparison of direction and object selectivity of local field potentials and single units in macaque posterior parietal cortex during prehension. J. Neurophysiol. 2007 May 1;3684–95.

46. Stark E, Abeles M. Predicting movement from multiunit activity. J. Neurosci. 2007 Aug 1;8387–94.

47. Bansal AK, Vargas-Irwin CE, Truccolo W, Donoghue JP. Relationships among low-frequency local field potentials, spiking activity, and three-dimensional reach and grasp kinematics in primary motor and ventral premotor cortices. J. Neurophysiol. 2011 Apr 1;1603–19.

48. Mitzdorf U. Current source-density method and application in cat cerebral cortex: investigation of evoked potentials and EEG phenomena. Physiol Rev. 1985 Jan 1;37–100.

49. Logothetis NK. The neural basis of the blood-oxygen-level-dependent functional magnetic resonance imaging signal. Philos. Trans. R. Soc. B Biol. Sci. 2002 Aug 29;1003–37.

50. Menzer DL, Rao NG, Bondy A, Truccolo W, Donoghue JP. Population interactions between parietal and primary motor cortices during reach. J. Neurophysiol. 2014 Dec 1;2959–84.

51. Mirollo RE, Strogatz SH. Synchronization of Pulse-Coupled Biological Oscillators. SIAM J. Appl. Math. Society for Industrial and Applied Mathematics; 1990 Dec 10;1645–62.

52. Buzsáki G, Geisler C, Henze DA, Wang X-J. Interneuron Diversity series: Circuit complexity and axon wiring economy of cortical interneurons. Trends Neurosci. 2004 Apr;186–93.

53. Womelsdorf T, Schoffelen J. Modulation of neuronal interactions through neuronal synchronization. …. 2007;

54. Schoffelen J, Oostenveld R, Fries P. Neuronal coherence as a mechanism of effective corticospinal interaction. Science (80-.). 2005;

55. Gregoriou G, Gotts S, Zhou H, Desimone R. High-frequency, long-range coupling between prefrontal and visual cortex during attention. Science (80-.). 2009;

56. Fries P. A mechanism for cognitive dynamics: neuronal communication through neuronal coherence. Trends Cogn. Sci. 2005 Oct;474–80.

57. Kopell N, Ermentrout GB, Whittington MA, Traub RD. Gamma rhythms and beta rhythms have different synchronization properties. Proc. Natl. Acad. Sci. 2000 Feb 15;1867–72.

58. Anastassiou CA, Perin R, Markram H, Koch C. Ephaptic coupling of cortical neurons. Nat. Neurosci. Nature Publishing Group, a division of Macmillan Publishers Limited. All Rights Reserved.; 2011 Feb;217–23.

59. Fröhlich F, McCormick DA. Endogenous electric fields may guide neocortical network activity. Neuron. 2010 Jul 15;129–43.

60. Rizzuto DS, Madsen JR, Bromfield EB, Schulze-Bonhage A, Kahana MJ. Human neocortical oscillations exhibit theta phase differences between encoding and retrieval. Neuroimage. 2006 Jul 1;1352–8.

61. Engel A, Roelfsema P, Fries P, Brecht M, Singer W. Role of the temporal domain for response selection and perceptual binding. Cereb. Cortex. 1997 Sep 1;571–82.

62. Canolty RT, Ganguly K, Kennerley SW, Cadieu CF, Koepsell K, Wallis JD, et al. Oscillatory phase coupling coordinates anatomically dispersed functional cell assemblies. Proc. Natl. Acad. Sci. U. S. A. 2010 Oct 5;17356–61.

63. von Stein A, Chiang C, König P. Top-down processing mediated by interareal synchronization. Proc. Natl. Acad. Sci. U. S. A. 2000 Dec 19;14748–53.

64. von Stein A, Sarnthein J. Different frequencies for different scales of cortical integration: from local gamma to long range alpha/theta synchronization. Int. J. Psychophysiol. 2000 Dec;301–13.

65. Buschman T, Miller E. Top-down versus bottom-up control of attention in the prefrontal and posterior parietal cortices. Science (80-.). 2007;

66. Thelen SLD; FCA; ASA; PL; AH; CTJ; EG; DG. OpenSim: open-source software to create and analyze dynamic simulations of movement. Biomed. …. 2007;

67. Holzbaur K, Murray W, Delp S. A model of the upper extremity for simulating musculoskeletal

surgery and analyzing neuromuscular control. Ann. Biomed. Eng. 2005;

68. Suminski AJ, Tkach DC, Fagg AH, Hatsopoulos NG. Incorporating feedback from multiple sensory modalities enhances brain-machine interface control. J. Neurosci. 2010 Dec 15;16777–87.

69. Arce-McShane FI, Hatsopoulos NG, Lee J-C, Ross CF, Sessle BJ. Modulation dynamics in the orofacial sensorimotor cortex during motor skill acquisition. J. Neurosci. 2014 Apr 23;5985–97.

70. Bortoff G, Strick P. Corticospinal terminations in two new-world primates: further evidence that corticomotoneuronal connections provide part of the neural substrate for manual dexterity. J. Neurosci. 1993;

71. M a Maier, K M Bennett, M C Hepp-Reymond RNL. Contribution of the monkey corticomotoneuronal system to the control of force in precision grip. J. Neurophysiol. 1993 Mar 1;772–85.

72. Cheney PD, Fetz EE. Functional classes of primate corticomotoneuronal cells and their relation to active force. J. Neurophysiol. 1980;773–91.

73. Muir R, Lemon R. Corticospinal neurons with a special role in precision grip. Brain Res. 1983;

74. Lemon R, Mantel G, Muir R. Corticospinal facilitation of hand muscles during voluntary movement in the conscious monkey. J. Physiol. 1986;

75. Palmer E, Ashby P. Corticospinal projections to upper limb motoneurones in humans. J. Physiol. Wiley-Blackwell; 1992 Mar 1;397–412.

76. Armand J, Olivier E, Edgley SA, Lemon RN. Postnatal Development of Corticospinal Projections from Motor Cortex to the Cervical Enlargement in the Macaque Monkey. J. Neurosci. 1997 Jan 1;251–66.

77. Kuypers HGJM. Corticospinal Connections: Postnatal Development in the Rhesus Monkey. Science (80-.). American Association for the Advancement of Science; 1962 Nov 9;678–80.

78. Rathelot J-A, Strick PL. Muscle representation in the macaque motor cortex: an anatomical perspective. Proc. Natl. Acad. Sci. U. S. A. 2006 May 23;8257–62.

79. Fetz EE, Cheney PD, Mewes K, Palmer S. Chapter 36 Control of forelimb muscle activity by populations of corticomotoneuronal and rubromotoneuronal cells. Prog. Brain Res. Affer. Control Posture Locomot. 1989. page 437–49.

80. Fetz E, Cheney P. Postspike facilitation of forelimb muscle activity by primate corticomotoneuronal cells. J. Neurophysiol. 1980;

81. Cheney P, Fetz E. Comparable patterns of muscle facilitation evoked by individual corticomotoneuronal (CM) cells and by single intracortical microstimuli in primates: evidence for functional groups of CM cells. J. Neurophysiol. 1985;

82. Shinoda Y, Yokota JI, Futami T. Divergent projection of individual corticospinal axons to motoneurons of multiple muscles in the monkey. Neurosci. Lett. 1981;7–12.

83. Saleh M, Takahashi K, Amit Y, Hatsopoulos NG. Encoding of coordinated grasp trajectories in primary motor cortex. J. Neurosci. 2010 Dec 15;17079–90.

84. Saleh M, Takahashi K, Hatsopoulos NG. Encoding of coordinated reach and grasp trajectories in

primary motor cortex. J. Neurosci. 2012;1220–32.

85. Hatsopoulos N, Amit Y. Synthesizing complex movement fragment representations from motor cortical ensembles. J. Physiol. 2012;

86. Malis LI, Pribram KH, Kruger L. Action potentials in “motor” cortex evoked by peripheral nerve stimulation. J. Neurophysiol. 1953;161–7.

87. Asanuma H. Recent developments in the study of the columnar arrangement of neurons within the motor cortex. Physiol. Rev. 1975;143–56.

88. Brooks VB, Stoney SD. Motor mechanisms: the role of the pyramidal system in motor control. Annu. Rev. Physiol. 1971;337–92.

89. Wong YC, Kwan HC, MacKay WA, Murphy JT. Spatial organization of precentral cortex in awake primates. I. Somatosensory inputs. J. Neurophysiol. 1978;1107–19.

90. Picard N, Smith AM. Primary motor cortical activity related to the weight and texture of grasped objects in the monkey. J. Neurophysiol. 1992 Nov 1;1867–81.

91. Strick P, Preston J. Multiple representation in the motor cortex: a new concept of input-output organization for the forearm representation. Integr. Nerv. Syst. 1979;

92. Tanji J, Wise SPS. Submodality distribution in sensorimotor cortex of the unanesthetized monkey. J. Neurophysiol. 1981 Mar 1;467–81.

93. Holsapple J, Preston J, Strick P. The origin of thalamic inputs to the “hand” representation in the primary motor cortex. J. Neurosci. 1991 Sep 1;2644–54.

94. Park MC, Belhaj-Saif A, Gordon M, Cheney PD. Consistent Features in the Forelimb Representation of Primary Motor Cortex in Rhesus Macaques. J. Neurosci. 2001 Apr 15;2784–92.

95. Schieber M, Poliakov A. Partial inactivation of the primary motor cortex hand area: effects on individuated finger movements. J. Neurosci. 1998;

96. Dickey AS, Suminski A, Amit Y, Hatsopoulos NG. Single-unit stability using chronically implanted multielectrode arrays. J. Neurophysiol. 2009 Aug 1;1331–9.

97. Lepage KQ, Kramer MA, Eden UT. The dependence of spike field coherence on expected intensity. Neural Comput. MIT Press 238 Main St., Suite 500, Cambridge, MA 02142-1046, USA email: journals-info@mit.edu; 2011 Sep 2;2209–41.

98. Pons TP, Garraghty PE, Cusick CG, Kaas JH. The somatotopic organization of area 2 in macaque monkeys. J. Comp. Neurol. 1985 Nov 22;445–66.

99. Toda T, Taoka M. The complexity of receptive fields of periodontal mechanoreceptive neurons in the postcentral area 2 of conscious macaque monkey brains. Arch. Oral Biol. 2001 Nov;1079–84.

100. Toda T, Taoka M. Integration of the upper and lower lips in the postcentral area 2 of conscious macaque monkeys (Macaca fuscata). Arch. Oral Biol. 2002 Jun;449–56.

101. Hyvärinen J, Poranen A. Receptive field integration and submodality convergence in the hand area of the post-central gyrus of the alert monkey. J. Physiol. 1978 Oct;539–56.

102. Taoka M, Toda T, Iwamura Y. Representation of the midline trunk, bilateral arms, and shoulders

in the monkey postcentral somatosensory cortex. Exp. Brain Res. 1998 Nov 16;315–22.

103. Taoka M, Toda T, Iriki A, Tanaka M, Iwamura Y. Bilateral receptive field neurons in the hindlimb region of the postcentral somatosensory cortex in awake macaque monkeys. Exp. Brain Res. 2000 Sep 5;139–46.

104. Iwamura Y, Tanaka M, Iriki A, Taoka M, Toda T. Processing of tactile and kinesthetic signals from bilateral sides of the body in the postcentral gyrus of awake monkeys. Behav. Brain Res. 2002 Sep;185–90.

105. Ageranioti-Bélanger S, Chapman C. Discharge properties of neurones in the hand area of primary somatosensory cortex in monkeys in relation to the performance of an active tactile discrimination task. Exp. brain Res. 1992;

106. Wolpaw JR. Correlations between task-related activity and responses to perturbation in primate sensorimotor cortex. J Neurophysiol. 1980 Dec 1;1122–38.

107. Gardner EP. Somatosensory cortical mechanisms of feature detection in tactile and kinesthetic discrimination. Can. J. Physiol. Pharmacol. NRC Research Press Ottawa, Canada; 1988 Apr 13;439–54.

108. Debowy D, Ghosh S, Ro J, Gardner E. Comparison of neuronal firing rates in somatosensory and posterior parietal cortex during prehension. Exp. Brain Res. 2001;

109. Burbaud P, Doegle C, Gross C, Bioulac B. A quantitative study of neuronal discharge in areas 5, 2, and 4 of the monkey during fast arm movements. J. Neurophysiol. 1991 Aug 1;429–43.

110. Randolph M, Semmes J. Behavioral consequences of selective subtotal ablations in the postcentral gyrus ofMacaca mulatta. Brain Res. 1974 Apr;55–70.

111. Carlson M. Characteristics of sensory deficits following lesions of brodmann's areas 1 and 2 in the postcentral gyrus ofMacaca mulatta. Brain Res. 1981 Jan;424–30.

112. Schwartz AS. Functional relationship between somatosensory cortex and specialized afferent pathways in the monkey. Exp. Neurol. 1983 Feb;316–28.

113. Moore C, Stern C, Corkin S. Segregation of somatosensory activation in the human rolandic cortex using fMRI. J. …. 2000;

114. Murthy V, Fetz E. Coherent 25-to 35-Hz oscillations in the sensorimotor cortex of awake behaving monkeys. … Natl. Acad. Sci. 1992;

115. Witham CL, Baker SN. Network oscillations and intrinsic spiking rhythmicity do not covary in monkey sensorimotor areas. J. Physiol. 2007 May 1;801–14.

116. Pons T, Kaas J. Connections of area 2 of somatosensory cortex with the anterior pulvinar and subdivisions of the ventroposterior complex in macaque monkeys. J. Comp. Neurol. 1985;

117. Strick P, Kim C. Input to primate motor cortex from posterior parietal cortex (area 5). I. Demonstration by retrograde transport. Brain Res. 1978;

118. Friedman D, Jones E. Thalamic input to areas 3a and 2 in monkeys. J. Neurophysiol. 1981;

119. Gharbawie O, Stepniewska I. Thalamocortical connections of functional zones in posterior parietal cortex and frontal cortex motor regions in New World monkeys. Cereb. …. 2010;

120. Lowe A. The neural regulation of tongue movements. Prog. Neurobiol. 1980;295–344.

121. Hoffman DS, Luschei ES. Responses of monkey precentral cortical cells during a controlled jaw bite task. J. Neurophysiol. American Physiological Society; 1980 Aug 1;333–48.

122. Murray GM, Sessle BJ. Functional properties of single neurons in the face primary motor cortex of the primate. I. Input and output features of tongue motor cortex. J Neurophysiol. 1992 Mar 1;747–58.

123. Murray GM, Sessle BJ. Functional properties of single neurons in the face primary motor cortex of the primate. II. Relations with trained orofacial motor behavior. J Neurophysiol. 1992 Mar 1;759–74.

124. Murray GM, Sessle BJ. Functional properties of single neurons in the face primary motor cortex of the primate. III. Relations with different directions of trained tongue protrusion. J.Neurophysiol. 1992;775–85.

125. Arce FI, Lee J-C, Ross CF, Sessle BJ, Hatsopoulos NG. Directional information from neuronal ensembles in the primate orofacial sensorimotor cortex. J. Neurophysiol. 2013 Sep 15;1357–69.

126. Huang CS, Hiraba H, Sessle BJ. Input-output relationships of the primary face motor cortex in the monkey (Macaca fascicularis). J Neurophysiol. 1989;350–62.

127. Huang CS, Hiraba H, Murray GM, Sessle BJ. Topographical distribution and functional properties of cortically induced rhythmical jaw movements in the monkey (Macaca fascicularis). J. Neurophysiol. 1989;635–50.

128. Hatanaka N, Tokuno H, Nambu A, Inoue T, Takada M. Input-output organization of jaw movement-related areas in monkey frontal cortex. J. Comp. Neurol. 2005;401–25.

129. Lin LD, Murray GM, Sessle BJ. Functional properties of single neurons in the primate face primary somatosensory cortex. I. Relations with trained orofacial motor behaviors. J Neurophysiol. 1994 Jun 1;2377–90.

130. Lin LD, Murray GM, Sessle BJ. Functional properties of single neurons in the primate face primary somatosensory cortex. II. Relations with different directions of trained tongue protrusion. J Neurophysiol. 1994 Jun 1;2391–400.

131. Kalaska J, Scott S, Cisek P, Sergio L. Cortical control of reaching movements. Curr. Opin. Neurobiol. 1997;

132. Lin LD, Sessle BJ. Functional properties of single neurons in the primate face primary somatosensory cortex. III. Modulation of responses to peripheral stimuli during trained orofacial motor behaviors. J Neurophysiol. 1994 Jun 1;2401–13.

133. Frost SB, Milliken GW, Plautz EJ, Masterton RB, Nudo RJ. Somatosensory and motor representations in cerebral cortex of a primitive mammal (Monodelphis domestica): a window into the early evolution of sensorimotor cortex. J. Comp. Neurol. 2000 May 22;29–51.

Appendix: The Effects of Chronic Intracortical Microstimulation On Neural Tissue and Fine Motor Behavior

ALEXANDER T. RAJAN[1,2], JESSICA L. BOBACK[2], JOHN F. DAMMANN[2], FRANCESCO V. TENORE[3], BROCK A. WESTER[3], KEVIN J. OTTO[4], ROBERT A. GAUNT[5], & SLIMAN J. BENSMAIA[1,2¥]

[1]COMMITTEE ON COMPUTATIONAL NEUROSCIENCE, UNIVERSITY OF CHICAGO, CHICAGO, IL

[2]DEPARTMENT OF ORGANISMAL BIOLOGY AND ANATOMY, UNIVERSITY OF CHICAGO, CHICAGO, IL

[3]RESEARCH AND EXPLORATORY DEVELOPMENT DEPARTMENT, JOHNS HOPKINS UNIVERSITY APPLIED PHYSICS LABORATORY, LAUREL, MD

[4]DEPARTMENT OF BIOMEDICAL ENGINEERING, UNIVERSITY OF FLORIDA, GAINESVILLE, FL

[5]DEPARTMENT OF PHYSICAL MEDICINE AND REHABILITATION, UNIVERSITY OF PITTSBURGH, PITTSBURGH, PA

Acknowledgments: This material is based upon work supported by the Defense Advanced Research Projects Agency under Contract N66001-10-C-4056. KJO was supported by DARPA (N66001-11-1-4013) and NIH (NIDCD R03DC009339-02).

Abstract

Objective: One approach to conveying sensory feedback in neuroprostheses is to electrically stimulate sensory neurons in cortex. For this approach to be viable, it is critical that intracortical microstimulation (ICMS) cause minimal damage to the brain. Here, we investigate the effects of chronic ICMS on the neuronal tissue across a variety of stimulation regimes in non-human primates. We also examine each animal's ability to use their hand – the cortical representation of which is targeted by the ICMS – as a further assay of possible neuronal damage. *Approach*: We implanted electrode arrays in the primary somatosensory cortex of three Rhesus macaques and delivered ICMS four hours per day, five days per week, for six months. Multiple regimes of ICMS were delivered to investigate the effects of stimulation parameters on the tissue and behavior. Parameters included current amplitude (10-100 μA), pulse train duration (1s, 5s), and duty cycle (1/1, 1/3). We then performed a range of histopathological assays on tissue near the tips of both stimulated and unstimulated electrodes to assess the effects of chronic ICMS on the tissue and their dependence on stimulation parameters. *Main results:* While the implantation and residence of the arrays in the cortical tissue did cause significant damage, chronic ICMS had no detectable additional effect; furthermore, the animals exhibited no impairments in fine motor control. *Significance:* Chronic ICMS may be a viable means to convey sensory feedback in neuroprostheses as it does not cause significant damage to the stimulated tissue.

Introduction

The loss of sensorimotor function has devastating consequences on quality of life. In an attempt to restore motor function, anthropomorphic robotic arms are being developed, as are algorithms to control these arms using signals from the brain [1]. Previously, signals from the motor cortex of tetraplegic patients have been used to control a robotic limb to perform motor tasks [2, 3]. While this is a remarkable accomplishment, upper-limb neuroprostheses may not be clinically viable until they include

somatosensory feedback [1, 4]. Indeed, tactile and proprioceptive feedback is critical for grasping and manipulating objects and performing activities of daily living [5]. Furthermore, somatosensation plays a critical role in emotional communication and in the embodiment of our limbs. One approach to providing somatosensory feedback is to stimulate neurons in somatosensory cortex through chronically implanted microelectrodes. Intracortical microstimulation (ICMS) can elicit somatosensory percepts that can be used to guide behavior by primates [4, 6-11] and rodents [12-15]. However, to be clinically relevant, ICMS must be demonstrated to be safe and robust over years or decades.

Previous studies have suggested that repetitive electrical stimulation may damage the brain. Indeed, long term ICMS has been shown to cause dynamic changes in electrode impedance, an assay of the tissue/electrode interface [16, 17], and to lead to higher stimulation thresholds [18, 19], depression of neuronal excitability [20], and neuronal loss [21, 22]. Importantly, neuronal loss has been reported at or below stimulation parameters that may be required to elicit behaviorally relevant responses [21]. We extend these previous findings by investigating the effects of chronic ICMS on neuronal tissue over a wide range of stimulation conditions. Specifically, we chronically delivered ICMS, spanning a range of stimulation parameters, to the primary somatosensory cortex (S1) of non-human primates (NHPs) over a period of six months. A range of histopathological assays were performed on slides of cortex including tissue near the tips of both stimulated and unstimulated electrodes. These slides were analyzed in three stages: first, a histopathologist examined each slide and described any large-scale changes in the tissue; second, the histopathologist qualitatively examined tissue around electrode tips and rated the damage in each sample (initially blinded to the stimulation regime to which the electrode had been subjected); third, a quantitative analysis on the neural density around a subset of electrode tips was performed. By carefully evaluating differences in tissue damage between stimulated and non-stimulated tissue, we determined how much damage occurred as a result of stimulation beyond that sustained as a result of implantation and explantation, and assessed the degree to which damage, if any, differed across stimulation regimes.

As a further assay of the effects of chronic ICMS, we assessed its consequences on fine motor control by evaluating the animals' ability to perform precision grips. We found that, while the implantation and residence of the arrays caused significant tissue damage, chronic ICMS delivered over the span of months causes minimal additional tissue damage and no detectable behavioral deficits over the range of parameters tested.

Methods

All procedures were approved by the University of Chicago Institutional Animal Care and Use Committee (IACUC), the Animal Care and Use Review Office (ACURO), and complied with the guidelines set by the Association for Assessment and Accreditation of Laboratory Animal Care (AAALAC) International. Furthermore, experiments were conducted under Good Laboratory Practices (GLP, Code of Federal Regulations, Title 21).

Arrays

ICMS was delivered to the primary somatosensory cortex via Utah Electrode Arrays with Cereport connectors (UEAs, Blackrock Microsystems, Salt Lake City, UT). Electrodes were 1.5 mm in length and their tips were coated with a sputtered iridium oxide film (SIROF) using the standard process [16, 23]. The electrode shaft was

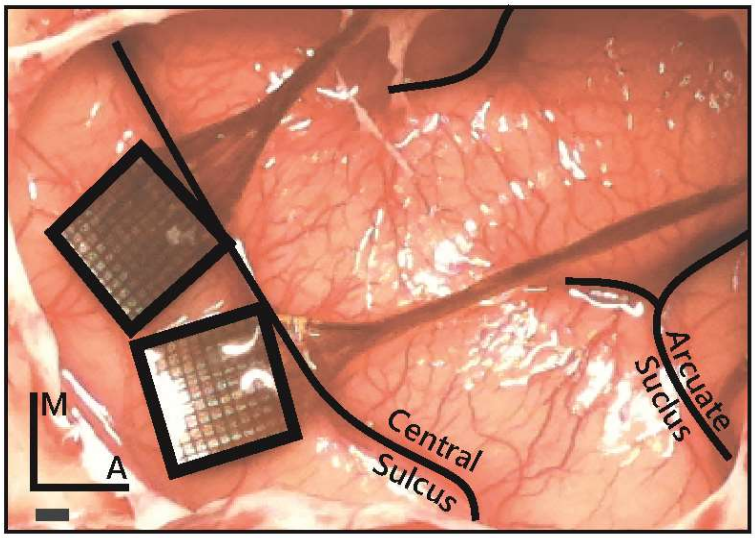

Figure 48 - Placement of the Utah electrode arrays in one NHP. The arrays were placed in the postcentral gyrus closely abutting the central sulcus to target the hand representations in areas 1 and 2, just posterior and medial to the termination of the intraparietal sulcus. Scale bar = 1 mm.

insulated with parylene-C along its length, with the exception of the tip, which had a targeted exposure length of 50-µm. Electrode impedances were measured to be between 10 and 80 kΩ prior to implantation. Each NHP was implanted with two UEAs: one posterior and medial to the other (Figure 48). We verified that receptive fields were located in the hand representation by monitoring multi-unit activity of each electrode in each UEA through speakers while palpating the hand.

Subjects

Three rhesus macaques (two male, one female) were each surgically implanted with two UEAs in the hand representation of somatosensory cortex. Two of the NHPs were research naïve prior to the study, and the third was involved in a study that did not involve the brain. All NHPs were between 6 and 8 years of age at the date of implantation.

Surgical Implantation

Having been administered atropine preoperatively (0.04 mg/kg, IM), NHPs were anesthetized with a mix of ketamine hydrochloride (2-3mg/kg, IM) and dexmedetomidine (75 µg/kg, IV), placed in a stereotaxic coordinator (Kopf Instruments, Tujunga, CA), and intubated. Anesthesia was maintained with isoflurane (1-3%). IV fluids and remifentanil (0.1-0.5µg/kg/min) were delivered throughout the procedure. Two UEAs were implanted using standard methods [6, 24-27] in the hand representation of primary somatosensory cortex (areas 1 and 2), identified in each case based on stereotaxic coordinates (approximately 6 mm anterior and 22mm lateral in ear-bar-based coordinates), and adjusted to anatomical landmarks (Figure 48). Indeed, we have found the hand representation to be consistently located medial and posterior (following the central sulcus) to where the intraparietal sulcus curls towards the central sulcus.

Stimulation Protocol

Each NHP was subjected to a 4-hour block of ICMS, 5 days per week (at the same time each day), for a period of six months (not including a one-week break during the winter holidays) beginning 9-11 weeks after implantation of the arrays. We report data from the time after onset of stimulation, not the time after array implantation. ICMS trains consisted of anodal phase-leading symmetrical pulses, (manufacturer default), with phases lasting 200 μs and an inter-phase delay of 53 μs, delivered at a frequenc y of 300 Hz using a CereStim R96 (Blackrock Microsystems Inc., Salt

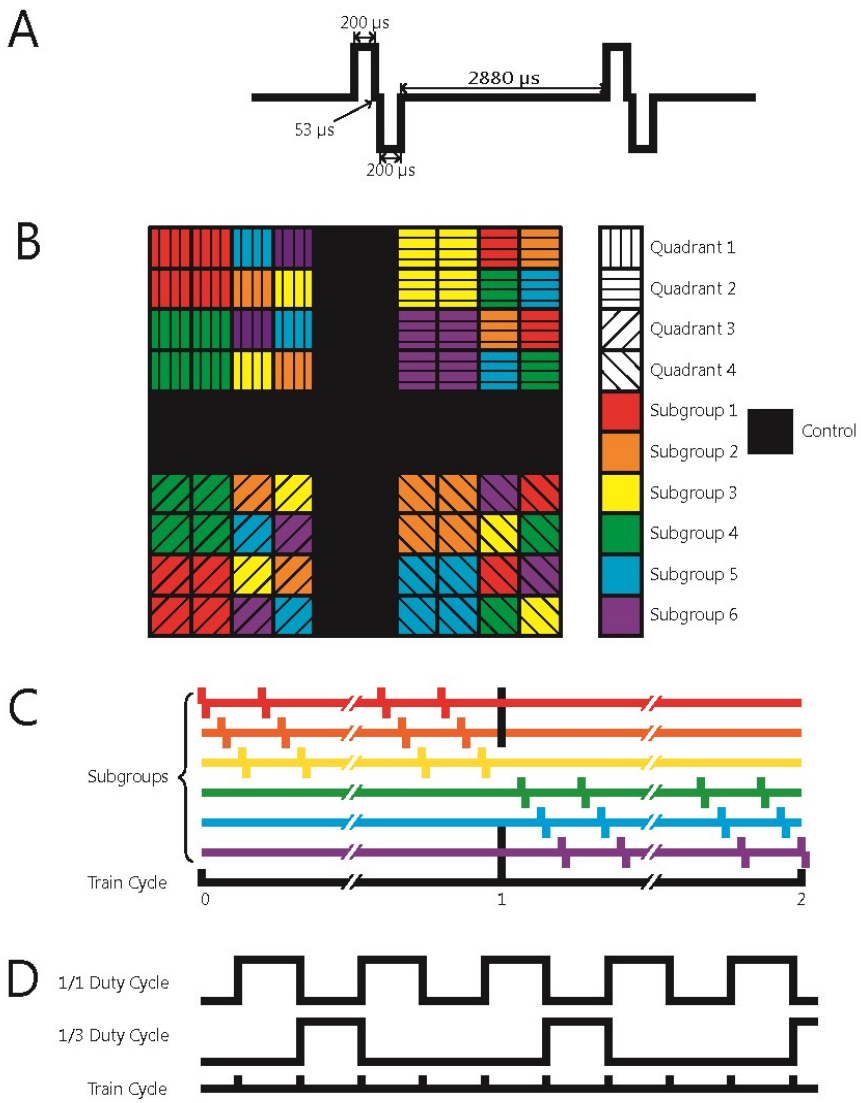

Figure 49 – Stimulation Protocol
A| Schematic of two charge-balanced stimulation pulses at 300 Hz. B| Electrode arrangement in each array. Each quadrant of electrodes was subjected to a different regime of stimulation. Black squares denote control electrodes. Arrays were divided into subgroups designed to control the amount of charge that was simultaneously delivered to the subject. Within a given quadrant, all subgroups were stimulated with the same stimulation parameters. C| Different stimulation regimes were also interleaved to distribute the current as evenly over time as possible. D| Interleaving of the 1/1 (50%) and 1/3 (25%) duty cycles.

Lake, City, UT) (Figure 49A). All stimulation pulses were delivered in a monopolar configuration with the titanium pedestal acting as the return electrode. Each UEA was divided into 4 non-contiguous quadrants, each receiving a different stimulation regime. Each quadrant consisted of a 4x4 grid of 16 electrodes at the corners of the 100- electrode array. Quadrants were separated by rows or columns, two electrodes wide, which received no stimulation (control electrodes) (Figure 49B). Each quadrant was further divided into two groups of 4 electrodes and 4 groups of 2 electrodes (Figure 49B). Stimulation was delivered in 6 asynchronous sets, each containing 1 group from each of the 4 quadrants (Figure 49C). While electrodes within each quadrant were subjected to pulse trains with the same parameters, the subgroups defined which electrodes were activated synchronously so that a maximum of 12 electrodes per array were simultaneously activated at any given time. The goal of this grouping strategy was to limit the amount of charge that was instantaneously injected in a localized region of tissue because we found that high levels of synchronous current resulted in rhythmic muscle contractions.

Three parameters varied across stimulation regimes: charge amplitude, duty cycle, and train duration (Figure 49). Charge amplitudes – 10 μA (2 nC/phase), 20 μA (4 nC/phase), and 100 μA (20 nC/phase) – were selected to span a range that have been shown to elicit a range of sensations [6] and we deemed based on previous studies to be safe [21]. Detection thresholds in primary somatosensory cortices of primates range in amplitude from 20-40 μA (4-8 nC/phase) [6], but lower thresholds can be achieved by simultaneously stimulating through multiple electrodes under some circumstances [28] but not others [29]. Thus, 10 μA and 100 μA amplitudes represented the lower and upper extremes of ICMS respectively and 20 μA served as a near-threshold stimulus. These stimulus amplitudes correspond to charge densities of 0.1, 0.2 and 1.0 mC/cm^2 assuming (per the manufacturer) that the electrodes have an exposed area of ~2000 μm^2. Both charge density and charge per phase are important as it has been understood for some time that these parameters play synergistic roles in shaping the behavior of the electrode-tissue interface [30, 31]. While electrode tip exposure can vary somewhat [16], charge per phase and charge density were

below the damage threshold for SIROF electrodes (see Figure 14 in ref. [16]). Duty cycle was included as a parameter because different stimulation duty cycles have been shown to lead to different tissue responses [21]. The duty cycles were either 1:1 or 1:3. Pulse train durations were either 1 second or 5 seconds (Figure 49C), to span the range of what might occur during object manipulation with a prosthetic hand.

Behavioral assessment

In order to provide a metric of the functional consequences of the long-term ICMS performed in this study, NHPs were tested on a grasping task after each stimulation session using small (<1 cm, e.g. raisin), medium (2-3 cm, e.g. grape) and large (>4 cm, e.g., apple slice) treats. Performance on each of the grasps was documented each day. Failure to grasp objects could indicate damage to somatosensory cortex based on the findings that small lesions within the fingertip regions of S1 can lead to difficulties in performing dexterous tasks [32].

Histology and microscopy

NHPs were first anesthetized with ketamine/dexmedetomidine and isoflurane then sacrificed with a lethal dose of Pentobarbitol (100 mg/Kg IP). The descending aorta was clamped, and the NHP was transcardially perfused with heparinized phosphate buffered saline, followed by 10% neutral buffered formalin. Whole brains were sent to Charles River Laboratories (CRL), Pathology Associates (Durham, NC) for qualitative histopathological evaluation under GLP controls.

Formalin fixed, paraffin embedded tissue sections overlapping with the locations of electrode implantation were sectioned coronally at 5 µm, mounted on glass slides, and then stained. Four stains and biomarkers were used to assess tissue health around the electrodes. Neuronal Nuclei (NeuN) was used as a marker of the presence of neuronal cell bodies, for which a reduction in NeuN density compared to the control tissue (around unstimulated electrodes or unimplanted tissue) indicates damage. Fluoro-

Jade B staining was used to detect degenerating neurons. Glial fibrillary acidic protein (GFAP) was used as a marker for astrocytes; an increase in the density of GFAP indicates an increase in reactive astrocytes near the electrode. Ionized calcium binding adaptor molecule 1 (Iba1) is a calcium-binding protein that is specifically expressed in microglia in the brain. An increase in Iba1 expression in microglia indicates neuroinflammation, infection, degeneration, or ischemia. Hematoxylin & Eosin (H&E), Luxol Fast Blue (LFB) and Cresyl Violet (CV) were used to stain nuclei and myelin, to identify astrocytic scars, to identify anatomical landmarks and for laminar identification.

Tissue slide evaluation

Tissue slides were evaluated by a board certified veterinary pathologist using light microscopy for any evidence of morphological changes and lesions in the somatosensory cortex. First, a gross histopathological analysis was performed, comparing implanted tissue with unimplanted tissue. Second, slides were scanned at a high resolution using an Aperio ScanScope slide scanner (Buffalo Grove, IL) and the scanned tissue was used to reconstruct the position of the array in the brain (see below). This reconstruction allowed us to identify the location of each electrode tip in the tissue and thus the stimulation regime to which that patch of tissue was subjected. Note that sections stained with Fluoro-Jade B and GFAP were examined but not scanned. As a result, they could not be not used in the three dimensional reconstructions or, therefore, in the side-by-side comparison of control electrodes and electrodes with specific stimulation regimes (since the 3D reconstruction was necessary to determine to which stimulation regime tissue on each slide was subjected). They were used, however, in the gross histopathological analysis. Third, the histopathologist visually examined the tissue surrounding each identified electrode tip (but blinded to the stimulation regime to which it had been subjected) and assigned ratings based on the quality of damage. These qualitative assessments were used to make histopathological comparisons between tissue samples that experienced different stimulation regimes.

Fourth, we verified the qualitative assessment of neural density by performing a quantitative assessment in a subset of samples.

Three dimensional reconstructions

We focused the histopathological analysis on the tissue within 250 µm of electrode tips. To identify these regions within each section, we matched patterns of lesions in each slice with electrodes on the array that caused those lesions, and then identified regions that were near a specific electrode tip. To this end, we reconstructed, based on scanned images of the slides, the position of the array in the tissue, matching individual tissue

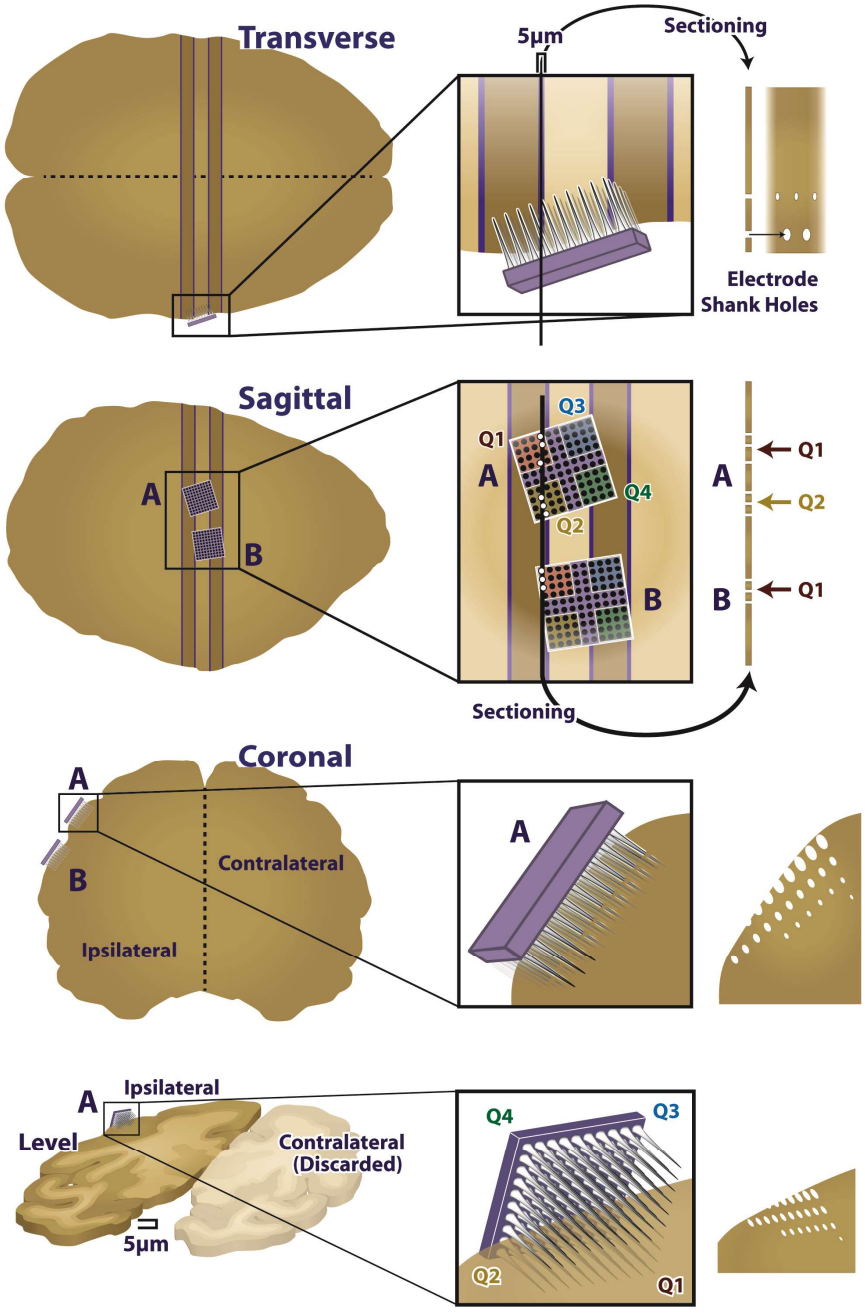

Figure 50 - Diagram of the Reconstruction Approach.
Example two-dimensional image of the three-dimensional reconstruction. Note the electrodes piercing the plane of the tissue, through the ellipsoid gaps in the tissue.

lesions with individual electrodes. To achieve this reconstruction, we aligned the two-dimensional tissue sections with three-dimensional models of UEAs (Adobe Illustrator; Google SketchUp, Pro/Engineer) (Figure 50). Given the known (approximate) location of the slice relative to the array, the layout and number of insertion tracks produced from each array, and the orientation of the array in the tissue, we were able to reconstruct the position of each slice with respect to the array. Insertion tracks were noted when there was a round or oblong hole in the tissue that could not be attributed to vasculature, at an appropriate distance from nearby insertion tracks, and shaped similarly to nearby insertion track holes. These reconstructions were performed independently by two investigators, and the same results were obtained from both analyses. We then identified 79 regions of tissue that were within 250 μm of the electrode tip and focused all histopathological analysis on these regions. Based on these reconstructions, we were able to unambiguously determine the stimulation paradigm to which each region of tissue was exposed.

Histopathological assessment

Images of tissue surrounding each identified electrode tip were captured, their order randomized, and sent to CRL for a "blind" qualitative histopathological assessment of the condition of the tissue. The histopathologist performing the assessment did not know from which NHP the tissue originated, nor the stimulation regime that had been delivered through the nearby electrode. The histopathologist examined the neuroparenchyma adjacent to the electrode tips for damage, including but not limited to neuronal necrosis or loss, gliosis and/or inflammation, astrocytic scarring, and pigmentation. After this examination, the stimulation condition was revealed, and a comparison of the amount of damage based on different stimulation regimes was performed. The images were graded based on four criteria: presence of insertion track; amount of gliosis; astrocytic scarring; and pigmentation. Other histopathological conditions were not evident in the tissue.

Ongoing neuronal degeneration and necrosis was diagnosed by the observation of Fluoro-Jade B positive neurons. Neuronal loss was evaluated by comparing the density of neurons near an electrode tip sample to adjacent intact tissue.

Gliosis was diagnosed when an increase in the number of microglia was observed (based on Iba1-stained slides). Gliosis was characterized as “minimal” when very few glial cells were present, and were restricted to an area of tissue with a radius of 60 µm or less. “Mild” was assigned when larger numbers of glial cells were present, and formed a small nodular cluster surrounding the insertion track, extending into the adjacent parenchyma with a radius of 60 – 135 µm. Glial scarring greater than ‘mild’ (that is, ‘moderate’ or ‘marked’) was not observed in the tissue samples. These ratings were based on standard pathology rating scales [33].

Astrocytic scars are bundles of astroglial fibers that typically surround insertion tracks [34-36] (based on primarily on H&E-stained slides). These fibers respond to the presence of foreign material by increasing the number and size of their cellular processes. Astrocytic scarring was judged on a scale analogous to that of gliosis.

Pigmentation refers to the presence of golden-brown pigment in glial cells surrounding electrode tracks. This discoloration might stem from a localized hemorrhage caused by the array implantation [35].

In order to quantify differences in tissue response across stimulation regimes, each sample was assigned a numerical score based on gliosis and astrocytic scarring. A score of 0 was ascribed when no damage was apparent, a score of 1 corresponded to minimal damage, and a score of 2 corresponded to mild damage. The scores for each stimulation regime were then compared to the control scores using an 8x3 Fisher-Freeman-Halton exact test, which is an extension of a 2x2 Fisher’s exact test that is applicable to multiple stimulation conditions (in this case eight) and outcome categories (in this case three: “none,” “minimal,” and “mild,”), and can be used with small sample sizes [37].

To validate the qualitative assessments of neuronal density provided by the histopathologist, we performed a quantitative analysis of density on a subset of samples. Specifically, we counted the number of neurons within concentric annuli defined by radii of 50, 100, and 150 µm from the electrode tips identified in NeuN-stained tissue. Neuronal densities were normalized with respect to unimplanted tissue sampled from the same neuronal layers within 1 to 4 mm from the edge of the array on the same slice of tissue. This analysis was carried out on 9 NeuN-stained samples that had been subjected to 20-µA (across duty cycles and durations) and 9 NeuN-stained samples with unstimulated electrode tips. If a given annulus was missing more than 50% of the tissue, the data was removed from the analysis (this occurred only in five 50 µm circles: two controls, and three stimulated; no 100-µm or 150-µm annuli were excluded). We could not perform this analysis on other stimulation conditions given the small number of slides stained with NeuN for those conditions.

Results

Two UEAs were implanted between the central and intraparietal sulci, within the hand representation in areas 1 and 2 of primary somatosensory cortex of the right hemisphere (Figure 48). After six months of chronic ICMS, the NHPs were perfused, and their brains were removed with the arrays and dura mater intact. After explantation of the arrays, depressions were visible in the cortex that corresponded to the shape, size, and orientation of the arrays (Figure 51A).

Effects of implantation and residence of arrays

The findings from gross histopathological analysis were similar across all NHPs and arrays. The tissue under all arrays was minimally to moderately atrophied. The remaining cortical thickness was usually approximately 70% of normal, adjacent tissue (range: 50-80%). The atrophy typically resulted from a partial loss of neurons from all cortical layers, and was never focused near electrode tips. Two

implantations resulted in atrophy that was focused in (but not limited to) specific cortical layers: layers I & II in one array in one animal, and layer III in another array in a different animal.

In two animals, a very small number of Fluoro-Jade B positive neurons were present in the superficial cortex immediately deep to the array, adjacent to the interface between the array and the cerebral cortex. These neurons are indicative of ongoing neuronal degeneration and necrosis. No Fluoro-Jade B positivity was detected in the third animal, or in the deep cortex at the site of stimulation of any animal.

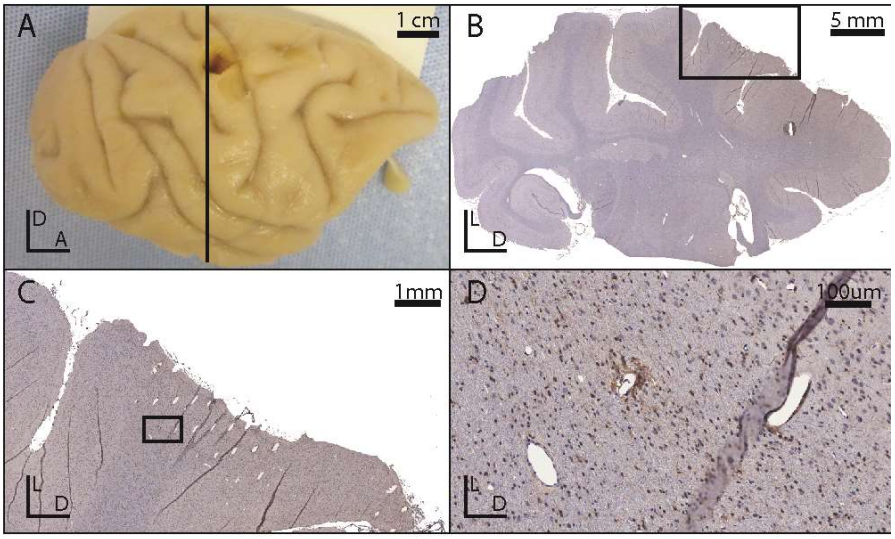

Figure 51 – Brain Slice Slides
A| Photograph of the right hemisphere of an explanted brain. Scale bar: 1 cm. B| Picture of a coronal slice with Iba1 stain from the brain show in panel A. The black box indicates the region shown in panel C. Scale bar: 5 mm. C| Close-up of the explanted tissue immediately deep to an implanted site. The black box indicates the region shown in panel D. Scale bar: 1mm. D| A close up of a lesion associated with an electrode tip. Note that the holes in the tissue which do not match the orientation of the other electrode tracks are likely vasculature. Scale bar: 100 µm.

Insertion tracks from the microelectrodes were evident in all sections deep to all of the electrode arrays (Figure 51B). Although all arrays were implanted such that the electrodes were normal to the cortical surface, the angle of the electrode tracks relative to the sectioned tissue varied according to the plane of section. More superficial tracks were larger in diameter and wedge or ovoid in shape (Figure 51C), whereas deeper tracks were smaller in diameter and tended to be circular rather than ovoid (Figure 51D).

Morphological changes near the electrode tip interface were localized to the immediately adjacent parenchyma, and consisted of increased number of hypertrophied astrocytes (with numerous cellular processes) and minimal aggregates of microglial cells lining the perimeter of the electrode insertion tracks. Intact neurons typically remained immediately adjacent to the tips (and were intertwined with the hypertrophied astroglial processes) suggesting the presence of astroglia did not preclude the presence of healthy neurons. No evidence of ongoing neuronal degeneration was present in the deep cortex adjacent to the electrode tips in any animal.

For the gross histopathology, the histologist was unable to identify with certainty whether individual electrodes received stimulation. However, in several slides, a sufficient number of electrode tracks were visible that these would necessarily span both stimulated and unstimulated electrodes. In these cases, the histologist found no morphological differences in the adjacent parenchyma. Thus, while the implantation and residence of the arrays in cortex did cause significant damage, the initial, gross histopathological assessment suggested that stimulation did not contribute additional damage.

Qualitative assessment of the effects of stimulation

Next, we describe the changes to the cortical tissue near electrode tips, described by the histopathologist, grouping these descriptions by stimulation regime, which was only revealed after the assessment was made.

* Unstimulated electrodes (Figure 52 A-D): We identified 39 samples near unstimulated electrode tips across all 6 arrays: 7 in slices stained with Iba1, 9 with NeuN, 14 with H&E, and 9 with LFB/CV. While no significant change (other than the presence of the electrode track) was typically seen, gliosis and/or astrocytic scarring was observed around the shaft or tip of a few electrodes. No reduction of the density of neuronal nuclei was observed near the tip.

* 10 µA, 1/1 duty cycle, 5 s: Four samples were identified in one array: 2 stained with Iba1, 1 with NeuN, and 1 with H&E. Iba1 antibody stains did not exhibit an increase near electrode tips. The H&E stain showed minimal non-specific damage to the tissue near an electrode tip. The NeuN-stained tissue did not show a qualitative reduction in neural density.

* 20 µA, 1/1 duty cycle, 1 s (Figure 52 E-H): The one tissue sample that corresponded to this condition was stained with Iba1 antibody and exhibited no qualitative increase in antibody density.

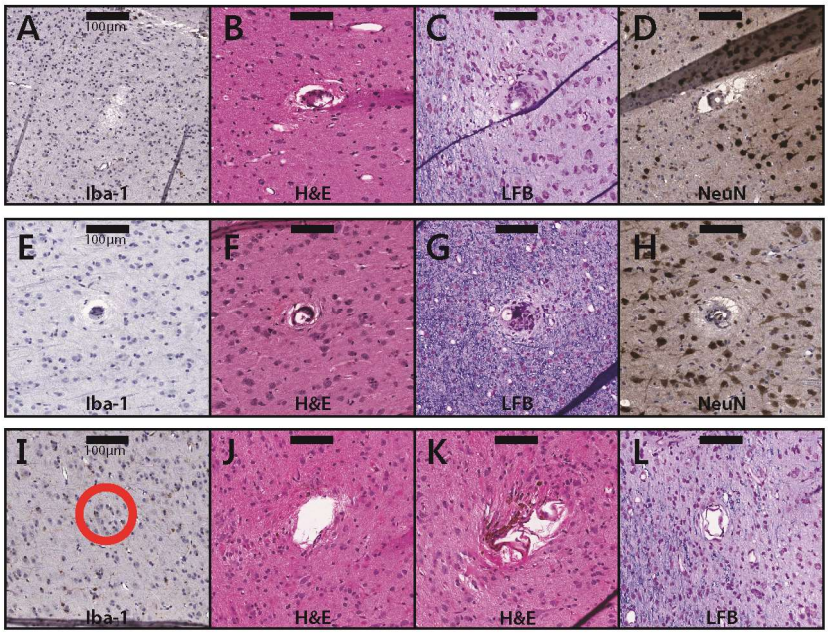

Figure 52 - Tissue samples near electrode tips subjected to different conditions.

A-D| Samples near electrode tips in unstimulated (control) tissue. The samples are taken from slices that were stained with Iba1 (A), H&E (B), LFB (C), and NeuN (D), respectively. The scale bars represent 100 µm. Note that, in these samples, the observed damage can only be attributed to the implantation, residence, or explantation of the array.

E-H| Samples near electrode tips that were subjected to 20-µA stimulation. Duty cycles were all 1/3; stimulation durations were 1s (E), 1s (F), 5s (G), and 1s (H). The tissue samples are taken from slices that were stained with Iba1 (E), H&E (F), LFB (G), and NeuN (H).

I-L| Samples near electrode tips that were subjected to 100-µA stimulation. Duty cycles were 1/1 (I) and 1/3 (J-L). All stimulation durations were 1 second. The tissue samples are taken from slices that were stained with Iba1 (I), H&E (J&K), and LFB (L). The scale bar represents 100 µm.

* 20 µA, 1/1 duty cycle, 5 s: Seven samples were identified across 2 arrays: 5 in slices stained with the Iba1 antibody, 1 with NeuN, and 1 with H&E. An increase in Iba1 antibodies was only observed in one of the five sections. There was no qualitative reduction in the density of neuronal nuclei and the H&E stain showed no abnormalities.

* 20 µA, 1/3 duty cycle, 1 s (Figure 52 E-F,H) : Fifteen samples were identified in 1 array: 5 stained with H&E, 6 with Iba1 antibody, and 4 with NeuN. The H&E stains show tissue adhesion to the electrodes, similar to other stimulation paradigms. Tissue in the Iba1 antibody-stained sections appeared healthy and NeuN stains did not indicate any qualitative reduction in the density of neuronal nuclei.

* 20 µA, 1/3 duty cycle, 5 s (Figure 52 G): Fifteen cortical samples were identified within 3 arrays: 5 stained with H&E, 6 with LFB/CV, 4 with NeuN. There were no samples with Iba1 antibody treatment. Several sections with anatomical stains (H&E & LFB/CV) showed a small increase in gliosis and astrocytic scarring in the neuroparenchyma along the perimeter of electrode tracks. However, there was no increase in inflammation, and NeuN stains did not indicate a reduction in the number of neuronal nuclei around the electrode tips.

* 100 µA, 1/1 duty cycle, 1 s (Figure 52 I): Four samples were identified from 1 array, on slices stained with the Iba1 antibody. No significant increase in the presence of Iba1 antibodies was observed near any of the four electrode tips. However, there is significant tissue damage, likely due to the removal of the array because similar damage was observed on control electrodes.

* 100 µA, 1/3 duty cycle, 1 s (Figure 52 J-L): Four samples were identified in 1 array: 2 in slices stained with H&E, and 2 with LFB/CV. The H&E stains showed slight damage to tissue along the perimeter of the electrode tracks, whereas the LFB/CV stains did not exhibit such damage (Figure 52 J-L).

Scoring of tissue damage

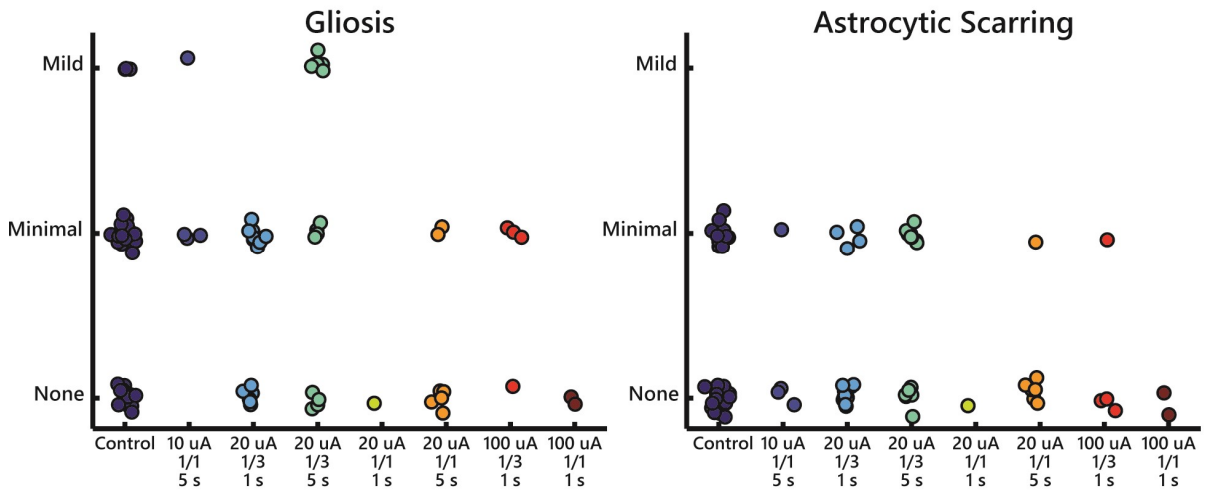

Figure 53 - Distribution of scores for each sample.
The only group whose score distribution was significantly different from the control condition was the 20 µA, 1/3 duty cycle, 5 second condition (p = 0.03, Fisher-Freeman-Halton exact test).

The damage of the tissue around each electrode tip was also scored by the histopathologist (Figure 53 & Figure 54). Statistical analysis revealed that only one regime – 20 µA, 1/3 duty cycle, 5 s – yielded a significantly different gliosis score compared to the control group (Fisher-Freeman-Halton exact test, p=0.03). No groups showed a difference in astrocytic scarring or pigmentation. Even the strongest

	Amp. (µA) Duty Cycle Duration (s)	Control	10 1/1 5	20 1/3 1	20 1/3 5	20 1/1 1	20 1/1 5	100 1/3 1	100 1/1 1
Scarring	No Damage	25	3	11	6	1	6	3	4
	Minimal	11	1	4	8	0	1	1	0
	Mild	0	0	0	0	0	0	0	0
Gliosis	No Damage	15	0	6	4	1	5	1	4
	Minimal	18	3	9	4	0	2	3	0
	Mild	3	1	0	6	0	0	0	0

Figure 54 – Table of Tissue Sample Counts

Number of tissue samples near identified electrode tips that received each score given by the histopathologist, who had been blinded to the stimulation condition. The only group whose score distribution was significantly different from the control condition was the 20 µA, 25% duty cycle, 5 second condition (p = 0.03, Fisher-Freeman-Halton exact test).

stimulation regimes (100 µA) did not exhibit significant changes relative to control electrodes, and no relationship was observed between stimulation regime and score. This semi-quantitative analysis supports the claim that chronic ICMS does not produce any detectable tissue damage. It should be noted, however, that few samples were available for the most intense stimulation regime – namely 100 µA – so results from this condition should be interpreted with caution.

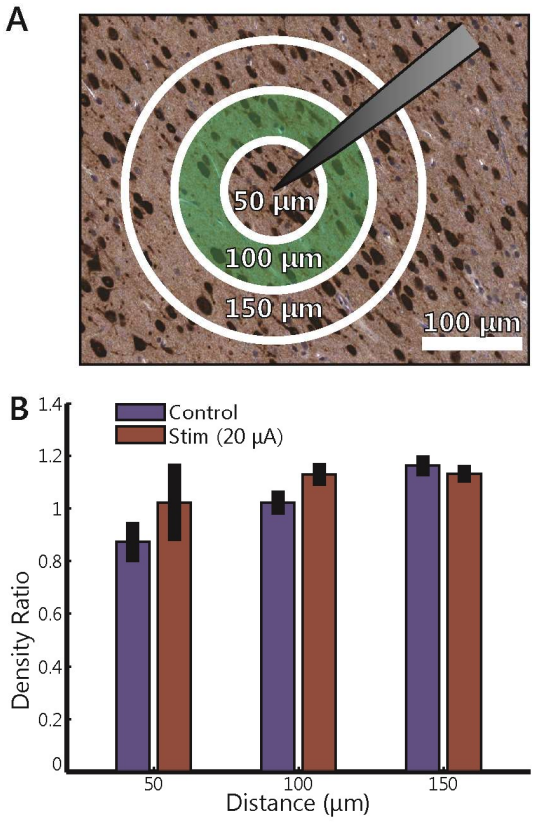

Figure 55 - Quantitative analysis of neuronal density.

A| Example of tissue showing the concentric annuli of increasing radii. Sample shown was stimulated at 20 µA.

B| Average normalized neuronal density for control tissue and tissue stimulated at 20 µA within distances of 50, 100, and 150 µm of the electrode tip. Error bars indicate standard error of the mean. Although there is a general (non-significant) trend of increased density as distance increases, there are no differences between control and stimulated tissue.

Quantitative comparison of neuronal Density

To validate the qualitative assessments of neuronal density provided by the histopathologist described above, we performed a quantitative analysis of density on the 20 µA samples, comparing these to control samples. We did not observe significant differences in neuronal density between the stimulated and unstimulated tissue (Figure 55 B) (ANOVA: $F(1,48) = 0.3$, $p = 0.59$). Further, there was no difference in density across tissues that were sampled at different distances (from 50 to 150 µm) from the electrode tip ($F(2,48) = 0.7$, $p = 0.52$), nor was there an interaction between stimulation condition and distance ($F(2,48) = 0.16$, $p = 0.85$). While this analysis was performed with a limited number of samples (a total of 18), results support

the conclusion of the qualitative histopathological analysis that neuronal density was not affected by stimulation.

Effects on behavior

The daily assessment of behavior revealed no effect of stimulation on the NHPs' ability to retrieve any of the treats presented, regardless of the size of the treat. Additionally, there were no noticeable abnormalities in the strategies used, preshaping, time to contact, or the accuracy and precision of retrieval for the duration of the implants. Ability to grasp or manipulate any of the presented treats was unimpaired, and the use of the hand contralateral to the stimulation appeared to be completely normal in these daily tests as well as in their behavior in the cage. In summary, neither the implantation process, the residence of the arrays, nor stimulation regime produced detectable deficits in the animals' ability to perform fine motor behaviors.

Discussion

Effect of array implantation and residence

Stimulation would be expected to result in "dose dependent" effects on tissue: higher stimulation amplitudes and durations would cause greater neuronal necrosis, gliosis, atrophy, etc. In contrast, morphological changes that are apparent uniformly across the array, or that are limited to the superficial layers of cortex are unlikely to be caused by stimulation. Instead, these effects are likely to be caused by implantation of the array and its chronic residence in cortex.

According to the histopathologist, Insertion and removal of the array likely caused most if not all of the tissue damage through shearing of tissue adhered to the electrodes and substrate. Tissue damage was observed both immediately deep to the array and along the shank of the electrodes and is consistent with the damage caused by arrays without any stimulation [35, 36, 38]. That the damage in control samples

was comparable to that observed in stimulated samples further supports the conclusion that the observed damage is primarily attributable to the implantation, residence, and explantation of the electrode arrays.

Histologic changes were limited to cortex underneath the implanted arrays, and included cortical atrophy, gliosis, macrophage infiltration with pigmentation, insertion tracks from the arrays, and neuronal necrosis. All of the observed changes are consistent with limited damage caused by the initial implantation of the array, and minimal to mild ongoing degeneration resulting from the chronic residence of the array. The changes at depths near electrode tips were minimal, and there was no evidence of ongoing neuronal degeneration at these depths. Rather, changes occurred either throughout all layers, or were focused around superficial cortex, at or near the interface between the array and the cortical surface.

Effects of stimulation parameters

Charge amplitude Stimulation amplitude, within the range delivered in this study, was not predictive of tissue health. The tissue surrounding the electrode tips that were subjected to the highest current amplitude (100 μA) did not exhibit more damage than tissue surrounding the tips of electrodes that had not been stimulated or that had been subjected to lower currents. Unfortunately, the sample size of tissue samples near stimulated electrodes was small, and did not include every stain for every stimulation condition. The 100-μA conditions in particular were underrepresented, especially compared to the 20 μA conditions. Even so, in only one of the four 20 μA stimulation condition (1/3 duty cycle, 5 s duration) did several samples exhibit noticeable changes compared to controls (along a single measure, namely gliosis, Figure 6). Astrocytic scarring for the 20-μA samples was equivalent to that of control samples, as was neuronal density. If charge amplitude (or charge density) were a determining factor in tissue health, other stimulation regimes with 20 μA amplitude would have exhibited signs of tissue damage (not to mention the more intense stimulation regimes).

Duty cycle: There was no evidence that varying duty cycle between stimulation regimes had any effect on cortical tissue. Indeed, at 20 μA and 5 s duration, samples from the 1/3 duty cycle tended to exhibit greater tissue damage than samples from its 1/1 counterpart, a paradoxical effect that is likely due to the small sample size of the 1/1 duty cycle condition (7 sections, compared to 15 sections for the 1/3 duty cycle).

Interval duration: Stimulation duration may have had a small effect on tissue health. The largest observed difference was between the 20 μA, 1/3 duty cycle, 1 s condition compared to the corresponding 5 s condition. The tissue that received the longer duration stimulation showed a significant increase in gliosis and astrocytic scarring. On the other hand, there was no difference in the NeuN densities between the two conditions, suggesting that the populations of neurons near these electrode tips were still healthy.

Overall, the histological analysis revealed that tissue surrounding stimulated and non-stimulated tissue exhibit similar attributes, suggesting that functionally relevant stimulation regimes do not cause implantation reduction in the density of healthy neurons. The only stimulation regime that yielded detectably greater gliosis and astrocytic scarring than unstimulated electrodes was the 20 μA, 1/3 duty cycle, 5 s duration condition. However, gliosis and astrocytic scarring are expected biological responses to the presence of the electrodes in the neural tissue and vary widely even given the same electrode geometry [34, 35, 38] so the observed effect may have been an artifact of a small sample size. With more samples (15) for the two 20 μA, 1/1 conditions, the small differences in tissue attributes between these two regimes may be evidence that stimulation duration may have a small effect on tissue damage. Overall, however, while individual conditions often had small sample sizes, we identified 40 sections that were near stimulated electrode tips, and another 39 that contained the tips of control electrodes. Over this large sample, the effects of ICMS were largely absent.

Comparison with other studies

Previous studies have reported significant changes in neural tissue morphology and associated neural recording capacity due to chronic electrode array implantation and residence. A well-organized sheath of fibroblast-generated collagen has been shown to form around chronically implanted electrodes [36], which is thought to contribute to an increase in electrode impedance [36, 39] as observed changes in impedance tend to be larger to the extent that this sheath is present [39]. Increased impedance and tissue reactions also follow a similar time course: impedance ramps up for approximately one week then exhibits a slow decline [39] while the electrode-tissue interface stabilizes during the first two weeks [40]. The evolution of the impedance for the control electrodes of the present study has recently been documented to follow the typical time course [41].

In acute ICMS studies, microstimulation at amplitudes ranging from 25 to 140 µA was found to induce no tissue damage or gliosis [42]. In a study on chronic ICMS, McCreery [30] stimulated electrodes for 7 hours at 50 Hz (at 800 and 1600 µC/cm2 or 52 and 104 nC/ph or 130 to 260 µA) for 10 days and found that no neuronal damage was induced, but immune responses were triggered. However, it is important to note that the stimulation parameters used in this previous study (high amplitude, low frequency) were very different from those used in the present study. In another study, fibrous tissue was found to form around UEA electrodes after being stimulated for up to 3 months at 250 Hz and 100 µA [27]. Using a quantitative approach to histology, McCreery and colleagues observed a loss of neurons within 60 µm to 150 µm of electrode tips after stimulating at 50 Hz, 8 hours a day for 30 days, with the extent of neuronal loss depending on the stimulation parameters [21]. Continuous stimulation at 10 µA did not cause any discernible damage, as there was no difference in neural density around electrodes stimulated at that amplitude compared to unstimulated electrodes. Stimulation at 20 µA, with a 1/1 duty cycle and 1-s pulse trains, induced a reduction in neuronal density that was greater within 60 µm of stimulated electrode tips. When stimulation was continuous rather than intermittent, the radius of damaged tissue increased to 150

µm. At an equivalent amplitude, we did not observe such significant neuronal damage, suggesting that continuous stimulation contributed to the damage in the previous study. However, we too found that longer pulse trains tended to produce more gliosis than shorter ones (among the 20 µA stimulation regimes, at least).

Finally, that our pulses were anodal phase-leading rather than the standard cathodal phase-leading might account for some of the differences between our results and those of previous studies. Indeed, stimulation with cathodal phase-leading is more effective at eliciting percepts than is stimulation with reversed polarity [43-45]. One possibility is that the efficiency of cathodal phase-leading stimulation is accompanied by an increased tendency to damage the neuronal tissue.

Consequences of chronic ICMS on electrode performance

Despite the changes to the neural substrate caused by implantation, recordings have been successfully obtained with UEAs even after months of ICMS, indicating the presence of functional neurons in close proximity to electrode tips. Rousche & Normann [27] found that multiple stimulation sessions did not significantly alter the signal to noise ratio or the number of recordable units. Parker and colleagues found that stimulated and non-stimulated arrays exhibited comparable declines in the number of action potentials recorded [17]. In fact, under certain circumstances and for short periods of time, stimulation may reverse the impedance drops due to tissue encapsulation [46] thereby actually improving single-unit recordings [47].

Further, stimulation seems to remain effective despite any changes to neural tissue and reductions in the quality of neural recordings that may occur. First, deep brain stimulation has been found to be effective for years [48], although the surface area of these electrodes is many times larger than the microelectrodes investigated here. Second, Parker and colleagues were able to evoke EMG responses after months of ICMS

[17]. Third, studies have shown that ICMS applied to primary sensory areas can evoke percepts over months or years [18, 27, 49-51].

In summary, studies of chronic ICMS have reported three main findings: both implanted and stimulated tissue react to the electrodes in a similar way; the quality of single-unit recordings usually decreases over time; despite damage to the neural tissue, the ability to stimulate is maintained over long periods with, in some cases but not others, small but progressive decreases in sensitivity to ICMS.

Consequences of chronic ICMS on fine motor control

Critically, any damage that may have resulted from the implantation of and stimulation through the electrodes did not result in behavioral deficits in our subjects. Previous studies with primates have explored the consequences of chemical inactivation of S1 [52] and of surgically induced microlesions in S1 [32] on performance in prehension tasks. Both studies reported profound sensory and motor impairments, as evidenced by discoordination of finger movements, misapplied forces, and the use of alternate movement strategies. These studies demonstrate that fine motor tasks are sensitive to small lesions in S1. While it is possible that the behavioral assays used in this study were insufficiently sensitive to detect deficits in fine motor control, at the very least they show that no coarse motor impairment is caused by chronic ICMS. That the NHPs in this study were completely unimpaired in this fine motor task supports the conclusion that chronic ICMS produces only minimal damage in S1 if any.

Conclusions

Our results suggest that chronic ICMS causes minimal tissue damage over a wide range of stimulation conditions and does not result in any detectable deficits in fine sensorimotor behavior. The stimulation parameters used in the present study have been shown to elicit meaningful percepts [6, 7]. Thus, our findings suggest that intracortical microstimulation from chronically implanted microelectrode arrays may be a viable approach to convey sensory feedback in upper limb neuroprostheses.

Bibliography

[1] S. J. Bensmaia and L. E. Miller, "Restoring sensorimotor function through intracortical interfaces: progress and looming challenges," *Nat Rev Neurosci,* vol. 15, pp. 313-25, Apr 17 2014.

[2] J. L. Collinger, B. Wodlinger, J. E. Downey, W. Wang, E. C. Tyler-Kabara, D. J. Weber, A. J. McMorland, M. Velliste, M. L. Boninger, and A. B. Schwartz, "High-performance neuroprosthetic control by an individual with tetraplegia," *Lancet,* vol. 381, pp. 557-64, Feb 16 2013.

[3] L. R. Hochberg, D. Bacher, B. Jarosiewicz, N. Y. Masse, J. D. Simeral, J. Vogel, S. Haddadin, J. Liu, S. S. Cash, P. van der Smagt, and J. P. Donoghue, "Reach and grasp by people with tetraplegia using a neurally controlled robotic arm," *Nature,* vol. 485, pp. 372-5, May 17 2012.

[4] G. A. Tabot, S. S. Kim, J. E. Winberry, and S. J. Bensmaia, "Restoring tactile and proprioceptive sensation through a brain interface," *Neurobiol Dis,* Sep 6 2014.

[5] R. S. Johansson and J. R. Flanagan, "Coding and use of tactile signals from the fingertips in object manipulation tasks," *Nat Rev Neurosci,* vol. 10, pp. 345-59, May 2009.

[6] G. A. Tabot, J. F. Dammann, J. A. Berg, F. V. Tenore, J. L. Boback, R. J. Vogelstein, and S. J. Bensmaia, "Restoring the sense of touch with a prosthetic hand through a brain interface," *Proc Natl Acad Sci U S A,* vol. 110, pp. 18279-84, Nov 5 2013.

[7] J. A. Berg, J. F. Dammann, 3rd, F. V. Tenore, G. A. Tabot, J. L. Boback, L. R. Manfredi, M. L. Peterson, K. D. Katyal, M. S. Johannes, A. Makhlin, R. Wilcox, R. K. Franklin, R. J. Vogelstein, N. G. Hatsopoulos, and S. J. Bensmaia, "Behavioral demonstration of a somatosensory neuroprosthesis," *IEEE Trans Neural Syst Rehabil Eng,* vol. 21, pp. 500-7, May 2013.

[8] J. E. O'Doherty, M. A. Lebedev, P. J. Ifft, K. Z. Zhuang, S. Shokur, H. Bleuler, and M. A. Nicolelis, "Active tactile exploration using a brain-machine-brain interface," *Nature,* vol. 479, pp. 228-31, Nov 10 2011.

[9] J. E. O'Doherty, M. A. Lebedev, T. L. Hanson, N. A. Fitzsimmons, and M. A. Nicolelis, "A brain-machine interface instructed by direct intracortical microstimulation," *Front Integr Neurosci,* vol. 3, p. 20, 2009.

[10] B. M. London, L. R. Jordan, C. R. Jackson, and L. E. Miller, "Electrical stimulation of the proprioceptive cortex (area 3a) used to instruct a behaving monkey," *IEEE Trans Neural Syst Rehabil Eng,* vol. 16, pp. 32-6, Feb 2008.

[11] M. C. Dadarlat, J. E. O'Doherty, and P. N. Sabes, "A learning-based approach to artificial sensory feedback leads to optimal integration," *Nat Neurosci,* vol. 18, pp. 138-44, Jan 2015.

[12] E. E. Thomson, R. Carra, and M. A. Nicolelis, "Perceiving invisible light through a somatosensory cortical prosthesis," *Nat Commun,* vol. 4, p. 1482, 2013.

[13] S. Venkatraman and J. M. Carmena, "Active sensing of target location encoded by cortical microstimulation," *IEEE Trans Neural Syst Rehabil Eng,* vol. 19, pp. 317-24, Jun 2011.

[14] D. H. O'Connor, S. A. Hires, Z. V. Guo, N. Li, J. Yu, Q. Q. Sun, D. Huber, and K. Svoboda, "Neural coding during active somatosensation revealed using illusory touch," *Nat Neurosci,* vol. 16, pp. 958-65, Jul 2013.

[15] M. Semprini, L. Bennicelli, and A. Vato, "A parametric study of intracortical microstimulation in behaving rats for the development of artificial sensory channels," *Conf Proc IEEE Eng Med Biol Soc,* vol. 2012, pp. 799-802, 2012.

[16] S. Negi, R. Bhandari, L. Rieth, R. Van Wagenen, and F. Solzbacher, "Neural electrode degradation from continuous electrical stimulation: comparison of sputtered and activated iridium oxide," *J Neurosci Methods,* vol. 186, pp. 8-17, Jan 30 2010.

[17] R. A. Parker, T. S. Davis, P. A. House, R. A. Normann, and B. Greger, "The functional consequences of chronic, physiologically effective intracortical microstimulation," *Prog Brain Res,* vol. 194, pp. 145-65, 2011.

[18] T. S. Davis, R. A. Parker, P. A. House, E. Bagley, S. Wendelken, R. A. Normann, and B. Greger, "Spatial and temporal characteristics of V1 microstimulation during chronic implantation of a microelectrode array in a behaving macaque," *J Neural Eng,* vol. 9, p. 065003, Dec 2012.

[19] A. S. Koivuniemi and K. J. Otto, "Asymmetric versus symmetric pulses for cortical microstimulation," *IEEE Trans Neural Syst Rehabil Eng,* vol. 19, pp. 468-76, Oct 2011.

[20] D. B. McCreery, W. F. Agnew, and L. A. Bullara, "The effects of prolonged intracortical microstimulation on the excitability of pyramidal tract neurons in the cat," *Ann Biomed Eng,* vol. 30, pp. 107-19, Jan 2002.

[21] D. McCreery, V. Pikov, and P. R. Troyk, "Neuronal loss due to prolonged controlled-current stimulation with chronically implanted microelectrodes in the cat cerebral cortex," *J Neural Eng,* vol. 7, p. 036005, Jun 2010.

[22] T. G. Yuen, W. F. Agnew, L. A. Bullara, S. Jacques, and D. B. McCreery, "Histological evaluation of neural damage from electrical stimulation: considerations for the selection of parameters for clinical application," *Neurosurgery,* vol. 9, pp. 292-9, Sep 1981.

[23] S. Negi, R. Bhandari, L. Rieth, and F. Solzbacher, "In vitro comparison of sputtered iridium oxide and platinum-coated neural implantable microelectrode arrays," *Biomed Mater,* vol. 5, p. 15007, Feb 2010.

[24] R. A. Normann, E. M. Maynard, P. J. Rousche, and D. J. Warren, "A neural interface for a cortical vision prosthesis," *Vision Res,* vol. 39, pp. 2577-87, Jul 1999.

[25] E. M. Maynard, E. Fernandez, and R. A. Normann, "A technique to prevent dural adhesions to chronically implanted microelectrode arrays," *J Neurosci Methods,* vol. 97, pp. 93-101, Apr 15 2000.

[26] E. M. Maynard, C. T. Nordhausen, and R. A. Normann, "The Utah intracortical Electrode Array: a recording structure for potential brain-computer interfaces," *Electroencephalogr Clin Neurophysiol,* vol. 102, pp. 228-39, Mar 1997.

[27] P. J. Rousche and R. A. Normann, "Chronic intracortical microstimulation (ICMS) of cat sensory cortex using the Utah Intracortical Electrode Array," *IEEE Trans Rehabil Eng,* vol. 7, pp. 56-68, Mar 1999.

[28] B. Zaaimi, R. Ruiz-Torres, S. A. Solla, and L. E. Miller, "Multi-electrode stimulation in somatosensory cortex increases probability of detection," *J Neural Eng,* vol. 10, p. 056013, Oct 2013.

[29] S. Kim, T. Callier, G. A. Tabot, F. V. Tenore, and S. J. Bensmaia, "Sensitivity to microstimulation of somatosensory cortex distributed over multiple electrodes," *Front Syst Neurosci,* vol. 9, p. 47, 2015.

[30] D. B. McCreery, W. F. Agnew, T. G. Yuen, and L. Bullara, "Charge density and charge per phase as cofactors in neural injury induced by electrical stimulation," *IEEE Trans Biomed Eng,* vol. 37, pp. 996-1001, Oct 1990.

[31] R. V. Shannon, "A model of safe levels for electrical stimulation," *IEEE Trans Biomed Eng,* vol. 39, pp. 424-6, Apr 1992.

[32] C. Xerri, M. M. Merzenich, B. E. Peterson, and W. Jenkins, "Plasticity of primary somatosensory cortex paralleling sensorimotor skill recovery from stroke in adult monkeys," *J Neurophysiol,* vol. 79, pp. 2119-48, Apr 1998.

[33] S. Love, P. Arie, J. Ironside, and H. Budka, *Greenfield's Neuropathology*. London, 2015.

[34] W. F. Agnew, D. B. McCreery, T. G. Yuen, and L. A. Bullara, "Histologic and physiologic evaluation of electrically stimulated peripheral nerve: considerations for the selection of parameters," *Ann Biomed Eng,* vol. 17, pp. 39-60, 1989.

[35] G. C. McConnell, H. D. Rees, A. I. Levey, C. A. Gutekunst, R. E. Gross, and R. V. Bellamkonda, "Implanted neural electrodes cause chronic, local inflammation that is correlated with local neurodegeneration," *J Neural Eng,* vol. 6, p. 056003, Oct 2009.

[36] W. M. Grill and J. T. Mortimer, "Electrical properties of implant encapsulation tissue," *Ann Biomed Eng,* vol. 22, pp. 23-33, Jan-Feb 1994.

[37] G. H. Freeman and J. H. Halton, "Note on an exact treatment of contingency, goodness of fit and other problems of significance," *Biometrika,* vol. 38, pp. 141-9, Jun 1951.

[38] R. Biran, D. C. Martin, and P. A. Tresco, "Neuronal cell loss accompanies the brain tissue response to chronically implanted silicon microelectrode arrays," *Exp Neurol,* vol. 195, pp. 115-26, Sep 2005.

[39] J. C. Williams, J. A. Hippensteel, J. Dilgen, W. Shain, and D. R. Kipke, "Complex impedance spectroscopy for monitoring tissue responses to inserted neural implants," *J Neural Eng,* vol. 4, pp. 410-23, Dec 2007.

[40] X. Liu, D. B. McCreery, R. R. Carter, L. A. Bullara, T. G. Yuen, and W. F. Agnew, "Stability of the interface between neural tissue and chronically implanted intracortical microelectrodes," *IEEE Trans Rehabil Eng,* vol. 7, pp. 315-26, Sep 1999.

[41] K. H. Chen, J. F. Dammann, J. L. Boback, F. V. Tenore, K. J. Otto, R. A. Gaunt, and S. J. Bensmaia, "The effect of chronic intracortical microstimulation on the electrode-tissue interface," *J Neural Eng,* vol. 11, p. 026004, Apr 2014.

[42] M. S. Graziano, C. S. Taylor, and T. Moore, "Complex movements evoked by microstimulation of precentral cortex," *Neuron,* vol. 34, pp. 841-51, May 30 2002.

[43] A. Koivuniemi, O. B. Regele, J. H. Brenner, and K. J. Otto, "Rat Behavioral Model for High-Throughput Parametric Studies of Intracortical Microstimulation," *Engineering in Medicine and Biology Society, EMBS, 2011 Annual International Conference of the IEEE,* pp. 7541-44, 2011.

[44] A. S. Koivuniemi and K. J. Otto, "The depth, waveform and pulse rate for electrical microstimulation of the auditory cortex," *Conf Proc IEEE Eng Med Biol Soc,* vol. 2012, pp. 2489-92, 2012.

[45] E. J. Tehovnik and W. M. Slocum, "Microstimulation of macaque V1 disrupts target selection: effects of stimulation polarity," *Exp Brain Res,* vol. 148, pp. 233-7, Jan 2003.

[46] M. D. Johnson, K. J. Otto, and D. R. Kipke, "Repeated voltage biasing improves unit recordings by reducing resistive tissue impedances," *IEEE Trans Neural Syst Rehabil Eng,* vol. 13, pp. 160-5, Jun 2005.

[47] K. J. Otto, M. D. Johnson, and D. R. Kipke, "Voltage pulses change neural interface properties and improve unit recordings with chronically implanted microelectrodes," *IEEE Trans Biomed Eng,* vol. 53, pp. 333-40, Feb 2006.

[48] G. Deuschl, J. Herzog, G. Kleiner-Fisman, C. Kubu, A. M. Lozano, K. E. Lyons, M. C. Rodriguez-Oroz, F. Tamma, A. I. Troster, J. L. Vitek, J. Volkmann, and V. Voon, "Deep brain stimulation: postoperative issues," *Mov Disord,* vol. 21 Suppl 14, pp. S219-37, Jun 2006.

[49] K. Torab, T. S. Davis, D. J. Warren, P. A. House, R. A. Normann, and B. Greger, "Multiple factors may influence the performance of a visual prosthesis based on intracortical microstimulation: nonhuman primate behavioural experimentation," *J Neural Eng,* vol. 8, p. 035001, Jun 2011.

[50] D. C. Bradley, P. R. Troyk, J. A. Berg, M. Bak, S. Cogan, R. Erickson, C. Kufta, M. Mascaro, D. McCreery, E. M. Schmidt, V. L. Towle, and H. Xu, "Visuotopic mapping through a multichannel stimulating implant in primate V1," *J Neurophysiol,* vol. 93, pp. 1659-70, Mar 2005.

[51] T. Callier, E. Schluter, G. Tabot, L. Miller, F. Tenore, and S. Bensmaia, "long-term stability of sensitivity to intracortical microstimulation of somatosensory cortex," *Journal of neural engineering,* in review.

[52] T. Brochier, M. J. Boudreau, M. Pare, and A. M. Smith, "The effects of muscimol inactivation of small regions of motor and somatosensory cortex on independent finger movements and force control in the precision grip," *Exp Brain Res,* vol. 128, pp. 31-40, Sep 1999.